

Three-Dimensional Dose Reconstruction using Non-Transmission Portal Dosimetry and Monte Carlo Calculations

Joseph Oliver Holmes

Master of Science

Medical Physics Unit

McGill University

Montréal, Québec Canada

June 2010

A thesis submitted to the Faculty of Graduate Studies and Research of McGill University in partial fulfillment of the requirements of the degree of Master of Science.

© Joseph O. Holmes, 2010

All rights reserved. This dissertation may not be reproduced in whole or in part by photocopy or other means, without the permission of the author.

DEDICATION

I dedicate this thesis to the love of my life, Chelsea M. Anderson. She has been overwhelmingly supportive, encouraging, and instrumental to my success in the M.Sc. program. I look forward to spending the rest of my life pursuing other challenging endeavors together with her.

ACKNOWLEDGEMENTS

My sincere gratitude goes to my supervisor Dr. ***François DeBlois*** for his support and willingness to adapt and overcome difficulties associated with working remotely on a thesis project. He played a pivotal role in maintaining a continual connection to McGill University and provided insightful discussions that aided in the success of my thesis.

My sincere appreciation goes to Dr. ***Andrew Reader*** for accepting and dedicating much time towards my request for his expertise pertaining to image restoration. He provided insightful discussion that aided in overcoming some of the most difficult obstacles in my thesis.

I would like to thank Dr. ***Stephen Steciw*** for providing guidance and helpful discussions for implementation of deconvolution methods. He also clarified my understanding of a publication he co-authored, which evolved into the back bone of my thesis project.

My appreciation goes as well to Dr. ***Ervin Podgoršak*** for his inspirational lectures and overwhelming dedication to medical physics and the world-renown program at McGill University. I also acknowledge him for providing me the opportunity to join this program and helping me to realize my dream.

I would like to also thank ***Andrew Alexander***, ***John Thébaut***, and ***Tanner Connell*** for their instruction on Monte Carlo and using the McGill computer cluster.

I would also like to express my greatest gratitude to my fiancée ***Chelsea Anderson***, and my parents ***Joe Holmes*** and ***Debra Holmes*** for their unconditional support throughout the two year medical physics program.

ABSTRACT

Amorphous silicon (a-Si) electronic portal imaging devices (EPIDs) offer convenient high-resolution and fast digital image acquisition, making the a-Si EPID advantageous for portal dosimetry. In this research project, a Varian aS1000 EPID was dosimetrically evaluated for portal dosimetry characteristics including: short-term reproducibility, linearity, field size dependence, pixel uniformity, dose-rate dependence, detector displacement, inverse square law, image lag, and memory effect. A convolution and Monte Carlo (MC) based non-transmission portal dosimetry method was also developed to reconstruct a 3D dose distribution. Images acquired by the Varian aS1000 EPID were deconvolved with a two part scatter kernel: a MC calculated dose kernel scored at the bottom of the scintillation screen, and an iteratively optimized optical spreading (or glare) kernel, to determine a 2D primary energy fluence (PEF) distribution. The derived PEF was converted into a phase space file (PSF) and utilized as a source input for DOSXYZnrc MC calculation. The EPID reconstructed 3D dose distributions were verified by comparison with measured beam profiles, PDDs, and 2D dose distributions.

ABRÉGÉ

Les dispositifs d'imagerie portale électronique (EPIDs) à base de silicium amorphe (a-Si) permettent l'acquisition rapide d'images digitales à haute résolution ce qui rend ces systèmes très utiles pour l'imagerie portale clinique. Pour les besoins de cette recherche, les caractéristiques dosimétriques d'un EPID aS1000 de Varian ont été évaluées dans le contexte de la dosimétrie portale. Les caractéristiques évaluées sont: la reproductivité à court terme, la linéarité, la dépendance de la taille du champ, l'uniformité de la matrice de pixels, la dépendance du débit de dose, le déplacement du détecteur, la loi de l'inverse du carré, le décalage d'image, et l'effet mémoire. Une méthode de dosimétrie portale en géométrie de « non transmission » utilisant les techniques de convolution et de Monte Carlo (MC) a également été mise au point pour reconstruire une distribution de dose 3D. Les images acquises par l'EPID aS1000 furent déconvoluées à l'aide d'un noyau corrigeant pour la dispersion se composant de deux parties: un noyau de dose calculée par MC au niveau de l'écran à scintillation, et un noyau itératif optimisé tenant compte de la propagation optique (ou l'éblouissement), afin de déterminer la distribution 2D de la fluence énergétique primaire (FEP). La FEP a été convertie en un fichier d'espace de phase « phase-space file » (PSF) et utilisé comme source pour les calculs de dose par MC à l'aide du code DOSXYZnrc. Les distributions de dose reconstruites 3D obtenues à partir de l'EPID ont été vérifiées en les comparant aux différents profils de doses et distributions de dose 2D.

TABLE OF CONTENTS

DEDICATION	ii
ACKNOWLEDGEMENTS	iii
ABSTRACT	iv
ABRÉGÉ	v
LIST OF TABLES	ix
LIST OF FIGURES	x
1 INTRODUCTION TO EXTERNAL BEAM RADIOTHERAPY	1
1.1 Historical Review	1
1.2 The Radiotherapy Process	3
1.3 Radiobiology of Radiotherapy	4
1.4 Clinical Goal of Radiotherapy	4
1.5 The Modern Medical Linear Accelerator	6
1.5.1 Acceleration and Beam Transport of Electrons	6
1.5.2 X-ray Production	9
1.5.3 Shaping, Flattening, Monitoring, and Secondary Collima- tion of Beam	10
1.5.4 The Multi-Leaf Collimator	12
1.6 Advanced External Beam Radiotherapy Techniques	12
1.6.1 Intensity Modulated Radiation Therapy	13
1.6.2 RapidArc	14
1.7 The Importance of Accurate Radiotherapy	14
1.8 Pretreatment Verification in Advanced Radiotherapy	16
1.9 Proposed Work	17
1.10 Scope and Structure of Thesis	18
References	20
2 INTRODUCTION TO MONTE CARLO SIMULATION IN RADIO- THERAPY	22
2.1 The Monte Carlo Method	22
2.2 Radiation Transport Simulation with EGSnrc	28
2.3 Linear Accelerator Head Simulation with BEAMnrc	29

2.4	Radiation Transport Simulation Through Patient with DOSXYZnrc	30
References		33
3	DOSIMETRIC DEVICES AND METHODS	35
3.1	Introduction	35
3.2	Ionization Chamber	35
3.3	Water Phantom	36
3.4	Photodiode Detector	38
3.5	Solid Water	39
3.6	Film Dosimetry	39
3.6.1	Gamma and Absolute Dose Difference	42
References		46
4	ELECTRONIC PORTAL IMAGING FOR RADIOTHERAPY DOSIMETRY	47
4.1	Portal Dosimetry Devices and Dosimetric Characteristics	47
4.1.1	Charged-Coupled Device Camera-Based	48
4.1.2	Scanning Liquid-Filled Ionization Chamber	49
4.1.3	Amorphous Silicon Flat Panel	51
4.1.4	Portal Dosimetry Methods	55
4.2	Dosimetric Evaluation of the PortalVision aS1000 EPID	56
4.3	Materials and Methods	57
4.3.1	Short-Term Reproducibility	57
4.3.2	Dose-Response Behavior	57
4.3.3	Field Size Dependence	57
4.3.4	Pixel Uniformity-Response	58
4.3.5	Dose-Rate Influence	59
4.3.6	EPID Displacement	59
4.3.7	Inverse Square Law Verification	59
4.3.8	Image Lag	59
4.3.9	Memory Effect	60
4.4	Results	60
4.5	Discussion and Conclusion	65
References		70
5	PRIMARY ENERGY FLUENCE EXTRACTION FROM EPID	73
5.1	Introduction	73
5.2	Materials and Methods	74
5.2.1	Initial Portal Image Correction	74
5.2.2	Beam Profile Correction	75
5.2.3	Determination of Scatter Kernel	75

5.2.4	Primary Energy Fluence Extraction	78
5.3	Results	80
5.3.1	Image Corrections	80
5.3.2	Beam Profile Correction	81
5.3.3	Glare and Dose Kernels	82
5.3.4	EPID Depth Dose	85
5.3.5	Measured and Optimized EPID In-Air Fluence Beam Profiles	86
5.3.6	Primary Energy Fluence	87
5.4	Discussion and Conclusion	89
	References	93
6	THREE-DIMENSIONAL DOSE RECONSTRUCTION USING PRIMARY ENERGY FLUENCE AND MONTE CARLO SIMULATION	94
6.1	Introduction	94
6.2	Materials and Methods	95
6.2.1	Generation of Phase Space File	95
6.2.2	DOSXYZnrc Simulation and Dose Normalization	97
6.3	Results	98
6.3.1	EPID Reconstructed Beam Profiles	98
6.3.2	EPID Reconstructed Percent Depth Doses	98
6.3.3	2D Dose Distribution Comparison	98
6.4	Discussion and Conclusion	102
	References	105
7	FINAL CONCLUSIONS	106
7.1	Dissertation Summary	106
7.2	Future Work	107
	ABBREVIATIONS	109
	REFERENCES	113

LIST OF TABLES

<u>Table</u>	<u>page</u>
Chapter 1	1
1–1 Overall uncertainty ^a in dose delivered at a point in a patient.	16
Chapter 3	35
3–1 Technical specifications for the IC-10 as stated by the manufacturer [5].	36
3–2 Technical specifications for the Blue Phantom as stated by the manufacturer [5].	37
3–3 Technical specifications for the PDIODE as stated by the manufacturer [5].	38
3–4 Technical specifications for the MapCHECK as stated by the manufacturer [2].	42
Chapter 4	47
4–1 Reproducibility of ten consecutive portal images acquired by the PortalVision aS1000.	61
4–2 PortalVision aS1000 EPID ROI values corresponding to the indicated positions (right) used to measure pixel uniformity for a 20×20 cm ² field size.	63
4–3 PortalVision aS1000 displacement in the cross-plane and in-line direction for various Varian gantry angles.	64

LIST OF FIGURES

<u>Figure</u>	<u>page</u>
Chapter 1	1
1-1 Probabilistic model of tumor control probability (TCP), normal tissue complication probability (NTCP), and uncomplicated normal tissue probability (UTCP).	5
1-2 Five-year relative survival rates SEER Program, 1999-2005, both sexes, and all races from nine different areas in the U.S. (San Francisco, Connecticut, Detroit, Hawaii, Iowa, New Mexico, Seattle, Utah, Atlanta)	7
1-3 The modern medical linear accelerator (Reproduced from Ervin. B. Podgorsak, Radiation Physics for Medical Physicists, page 111) [11].	8
1-4 A cutaway view of a 6 MV standing wave accelerating waveguide (Reproduced from Ervin. B. Podgorsak, Radiation Physics for Medical Physicists, page 87) [11].	9
1-5 Varian Clinac 23EX 6 MV location and geometry of electron target, primary collimator, vacuum window (berillium), and flattening filter.	11
1-6 A Varian Millennium multi-leaf collimator [Varian Medical Systems, Palo Alto, CA].	12
Chapter 2	22
2-1 Regions of predominance for the three main photon interaction with matter (Reproduced from Ervin. B. Podgorsak, Radiation Physics for Medical Physicists, page 246) [13].	24
2-2 A schematic model of a Varian Clinac 23EX showing the component modules used in BEAMnrc.	30
2-3 Phase-space source incident from any direction (isource=2). Similar to source 1, a polar coordinate system is set up at the isocenter, (xiso, yiso, ziso). The position of the origin in the phase-space plane is then defined by the angles theta and phi, and the distance from the isocenter, dsource. The source can be rotated in its own plane using the variable phicol [10].	31

Chapter 3	35
3-1 The IC-10 ionization chamber.	36
3-2 The 3D water phantom system (Blue Phantom) used for beam profile and PDD measurements [5].	37
3-3 PDIODE photodiode [5].	38
3-4 Solid Water slabs [4].	39
3-5 Multi-leaf collimator shaped step wedge consisting of fourteen dose steps measured at a depth of 5.0 cm in Solid Water (cGy) and a zoomed view of a pinhole cross-hair position used for centering the film.	40
3-6 MapCHECK 2D photodiode array used for film dose calibration [2].	41
3-7 Characteristic curve for Kodak EDR2 radiographic film and Epson Expression 10000 XL flatbed scanner at 5.0 cm depth in Solid Water.	43
3-8 2D geometric representation of γ evaluation criteria using the combined ellipsoidal dose-difference and distance-to-agreement tests.	44
Chapter 4	47
4-1 Schematic illustration of optical elements for one type of geometry used for camera-based EPID systems.	49
4-2 Cross-sectional view of the scanning liquid filled ionization chamber.	50
4-3 Schematic illustration of x-ray detection in an a-Si EPID for indirect detection using a scintillation screen.	51
4-4 (a) PortalVision aS1000 and Exact Arm assembly (b) image detection unit assembly [23].	53
4-5 PortalVision aS1000 image detection unit layers.	53
4-6 (a) Close-up view of a PortalVision aS1000 individual pixel and (b) detector array.	54
4-7 Specific EPID ROI positions used to measure pixel uniformity for a 20×20 cm ² field size.	58
4-8 PortalVision aS1000 dose-response to increasing monitor units.	61
4-9 PortalVision aS1000 field size dependence (total scatter factor) as compared to photodiode (PDIODE) measurement at 8.0 mm depth in water.	62

4–10	PortalVision aS1000 relative EPID response for various dose-rates acquired at 20 and 100 MU.	64
4–11	A verification of the inverse square law as measured by the PortalVision aS1000 relative response to change in source-to-detector distance.	65
4–12	PortalVision aS1000 continuous imaging mode acquisition from 0 to 44 seconds, demonstrating the image lag effect and triple-exponential fit $G(t_{rad})$ equation.	66
4–13	The demonstration of the memory effect by the PortalVision aS1000 after the acquisition sequence of a (1) 5 MU 20×20 cm ² , (2) 500 MU 5×5 cm ² , and (3) 5 MU 20×20 cm ²	67
Chapter 5		73
5–1	Monte Carlo PortalVision aS1000 EPID model for simulation of beam-let to determine the dose kernel, where ψ indicates orientation of incident primary energy fluence.	76
5–2	Diagram of 1D to 2D scatter kernel conversion based on factorization of the cross-plane and in-line kernel directions.	78
5–3	Narrow beam geometry measurement setup used for the determination of the total linear attenuation coefficient.	79
5–4	Calibration images: (a) pixel defect map, (b) flood field, (c) dark field, and (d) noise image.	81
5–5	Beam profile correction matrix originating from a radially mapped 6 MV, 40×40 cm ² field profile measured at a depth of 8.0 mm in water: (a) two-dimensional beam profile correction weighting, and (b) an in-line profile measured along the central axis of (a) (red).	82
5–6	A comparison between a raw (dotted) and beam profile corrected (solid) 6 MV, 10×10 cm ² EPID cross-plane profile.	83
5–7	The cross-plane kernels used for the EPID deconvolution: the MC generated dose kernel scored in the scintillation screen, the iteratively optimized glare kernel, and the combined dose-glare scatter kernel.	84
5–8	Three-dimensional dose-glare scatter kernel.	85
5–9	Monte Carlo depth dose curve scored in each PortalVision aS1000 EPID layer where, ψ indicates orientation of incident primary energy fluence directed at the EPID model.	86

5-10	Cross-plane profiles for a 6 MV, 10×10 cm ² in-air field taken with the raw EPID, the IC-10 ionization chamber, and the iteratively optimized (primary fluence) EPID corrected image.	87
5-11	Ionization chamber (IC-10) attenuation measurement with increasing Solid Water attenuator thickness, where $I^{\theta=0}$ is the attenuated intensity.	88
5-12	Mean photon energy distribution: (a) mean photon energy matrix in MeV, and (b) an in-line profile along central axis of (a) (red). . . .	88
5-13	A summary of the calibration process to extract the primary energy fluence from a PortalVision aS1000 EPID 6 MV, 10×10 cm ² image.	89
Chapter 6	94
6-1	EPID reconstructed open-field cross-plane beam profiles at depths of 5.0, 10.0, and 15.0 cm in water as compared to PDIODE measurement: (a) 5×5 cm ² , (b) 10×10 cm ² , and (c) 20×20 cm ²	99
6-2	EPID reconstructed PDDs as compared to PDIODE measurement in water: (a) 5×5 cm ² , (b) 10×10 cm ² , and (c) 20×20 cm ²	100
6-3	A 6 MV, 10×10 cm ² open-field 2D dose distributions obtained at 5.0 cm depth in water (Solid Water for film): (a) EPID reconstructed, and (b) EDR2 radiographic film.	101
6-4	Absolute dose difference between EDR2 radiographic film and EPID reconstruction normalized to max film dose for a 6 MV, 10×10 cm ² open-field 2D dose distribution obtained at 5.0 cm depth in water (Solid Water for film): (a) absolute dose distribution (cGy), and (b) histogram of (a).	101
6-5	γ evaluation between EDR2 radiographic film and EPID reconstruction for a 6 MV, 10×10 cm ² open-field 2D dose distribution obtained at 5.0 cm depth in water (Solid Water for film): (a) γ distribution, and (b) histogram of (a).	102
6-6	A 6 MV, 10×10 cm ² 60° enhanced dynamic wedge 2D dose distributions obtained at 5.0 cm depth in water (Solid Water for film): (a) EPID reconstructed, and (b) EDR2 radiographic film.	102
6-7	Absolute dose difference between EDR2 radiographic film and EPID reconstruction normalized to max film dose for a 6 MV, 10×10 cm ² 60° enhanced dynamic wedge 2D dose distribution obtained at 5.0 cm depth in water (Solid Water for film): (a) absolute dose distribution (cGy), and (b) histogram of (a).	103

6–8	γ evaluation between EDR2 radiographic film and EPID reconstruction for a 6 MV, 10×10 cm ² 60° enhanced dynamic wedge 2D dose distribution obtained at 5.0 cm depth in water (Solid Water for film): (a) γ distribution, and (b) histogram of (a).	103
-----	---	-----

CHAPTER 1

INTRODUCTION TO EXTERNAL BEAM RADIOTHERAPY

Contents

1.1	Historical Review	1
1.2	The Radiotherapy Process	3
1.3	Radiobiology of Radiotherapy	4
1.4	Clinical Goal of Radiotherapy	4
1.5	The Modern Medical Linear Accelerator	6
1.5.1	Acceleration and Beam Transport of Electrons	6
1.5.2	X-ray Production	9
1.5.3	Shaping, Flattening, Monitoring, and Secondary Col- limation of Beam	10
1.5.4	The Multi-Leaf Collimator	12
1.6	Advanced External Beam Radiotherapy Techniques .	12
1.6.1	Intensity Modulated Radiation Therapy	13
1.6.2	RapidArc	14
1.7	The Importance of Accurate Radiotherapy	14
1.8	Pretreatment Verification in Advanced Radiotherapy	16
1.9	Proposed Work	17
1.10	Scope and Structure of Thesis	18

1.1 Historical Review

Since the discovery of x-rays in 1895 by Wilhelm Conrad Roentgen, the medical field has been revolutionized by its opportunities for treatment and diagnosis. Within the first year of the discovery, x-rays were used for treatment of malignant diseases. This new form of treatment eventually became known as external beam radiotherapy (EBT) and matured into an effective cancer management tool in the field of Radiation Oncology. The first reported case of a

patient cured by radiotherapy was in 1899, although, in the beginning treatment with ionizing radiation often produced normal tissue damage. In the 1950's Harold E. John's group conducted physics research on a cobalt-60 teletherapy machine. These machines utilized a radioactive cobalt-60 source to produce monoenergetic gamma radiation of 1.25 MeV (1.173 MeV and 1.332 MeV). On October 27th, 1951 the first patient in the world to be treated with cobalt-60 teletherapy took place in London, Ontario, Canada. As technology progressed, teletherapy machines were replaced by particle accelerators, which utilized betatrons and were capable of producing megavoltage x-ray treatment. These particle accelerators would later develop into more sophisticated medical linear accelerators (linac). Today in the field of Radiation Oncology, linacs are in routine use due to their ability to produce variable energy x-ray beams and electron beams, while not requiring the management of radioactive sources.

EBT has gone through many technological advances over the years, one important aspect has been its evolution towards increased conformality of dose to the target volume. Treatment planning with high conformality allows for increased dose deposition to the intended target and less to normal tissues. However, the success of conformal dose distributions rely heavily on the knowledge of the tumor extent and the ability to shape the radiation field. Prior to the 1970s, much of the planning was done manually using standard isodose charts mapped out on a patient's body and utilized bulky field blocks. After the 1970s computed tomography (CT), then 1980s came magnetic resonance imaging (MRI), along with increased computational power, led to better delineation of targets and a more sophisticated radiotherapy technique known as three-dimensional conformal radiotherapy (3D-CRT). To achieve conformal shapes 3D-CRT utilized fixed radiation beams and three dimensional anatomical information from CT and MRI to shape the radiation field. The field shaping was accomplished through the use

of beam modifiers such as, wedges, compensating filters, and transmission blocks, which modified the beam fluence resulting in a radiation distribution tailored to the anatomical target volume.

1.2 The Radiotherapy Process

In radiotherapy, many steps work towards the objective of directing very accurately ionizing radiation to a well-defined target volume while minimizing radiation dose to surrounding healthy tissues. The process starts with diagnosis and target localization, determined by a wide variety of imaging modalities and simple clinical examinations. Treatment planning is another crucial step used to delineate target volumes from 3D CT images and radiation beams are chosen to adequately cover the localized target. Three sub-volumes define the target including: gross tumor volume (GTV), clinical target volume (CTV), and planning target volume (PTV). The GTV is the gross or visible/demonstrable extent and location of malignant growth [6]. The CTV is a tissue volume that contains a demonstrable GTV and/or subclinical microscopic malignant disease, which has to be eliminated. This volume thus has to be treated adequately in order to achieve the aim of therapy, cure or palliation [6]. The PTV is defined as a geometrical concept, and dictates the appropriate beam sizes and beam arrangements, taking into consideration the net effect of all the possible geometrical variations, in order to ensure that the prescribed dose is actually absorbed in the CTV [6]. The treatment planning system (TPS) uses the delineated CT images, doses prescribed by the radiation oncologist, and dose limitation of critical structures to develop radiation beam configurations to meet these conditions. Before the treatment is delivered, treatment verification is performed to ensure the radiation beam delivers dose to the desired target, while avoiding critical structures.

1.3 Radiobiology of Radiotherapy

From a radiobiological perspective, the biologic effect caused by absorption of ionizing radiation in biological material is mainly a result of damage to deoxyribonucleic acid (DNA). Commonly for x-rays, the interaction is through indirect action. In this process incident x-rays produce fast recoil electrons, primarily through the Compton effect, that create free hydroxyl radicals (hydroxyl molecules carrying an unpaired orbital electron) as they traverse water resulting in a chemical change and consequently DNA strand breaks. Single and double strand DNA breaks may occur, however evidence has shown that double-strand DNA breaks lead to important biologic end points, including cell death [5].

1.4 Clinical Goal of Radiotherapy

The goal of EBT is to induce mitotic death and/or apoptosis of malignant cancer cells, while avoiding surrounding healthy tissues. One way to characterize this objective is to plot a dose response curve. A dose response curve is a plot of a chosen biological endpoint (cell death) against the dose given to a particular tissue. The typical response of tissues to ionizing radiation is characterized by a sigmoid curve. To quantify the delicate balance between tumor control and normal tissue damage, a probabilistic model based on clinical evidence defines the tumor control probability (TCP) and normal tissue complication probability (NTCP). In Figure 1–1, both the TCP and NTCP increase with dose then reach a threshold where the slope becomes shallow and asymptotically approaches 100%. Oftentimes, the NTCP has a steeper slope than TCP due to the homogenous nature of normal tissues [5]. Optimally, the radiotherapy technique should maximize the TCP, while minimizing the NTCP. The further the NTCP curve is to the right of the TCP curve the higher the likelihood of achieving the radiotherapeutic goal. A good radiotherapy treatment, $TCP \geq 0.5$ and $NTCP \leq 0.05$. The therapeutic ratio, generally defined as the ratio of TCP to NTCP for a fixed level of normal tissue

damage (usually 0.05), places a number on the likelihood of radiotherapy success. Another curve used to measure the effectiveness of radiotherapy treatment is plotted in Figure 1–1 called the uncomplicated tissue control probability (UTCP), and represents the probability of achieving tumor control while having no normal tissue complications and is calculated as $TCP \times (1 - NTCP)$.

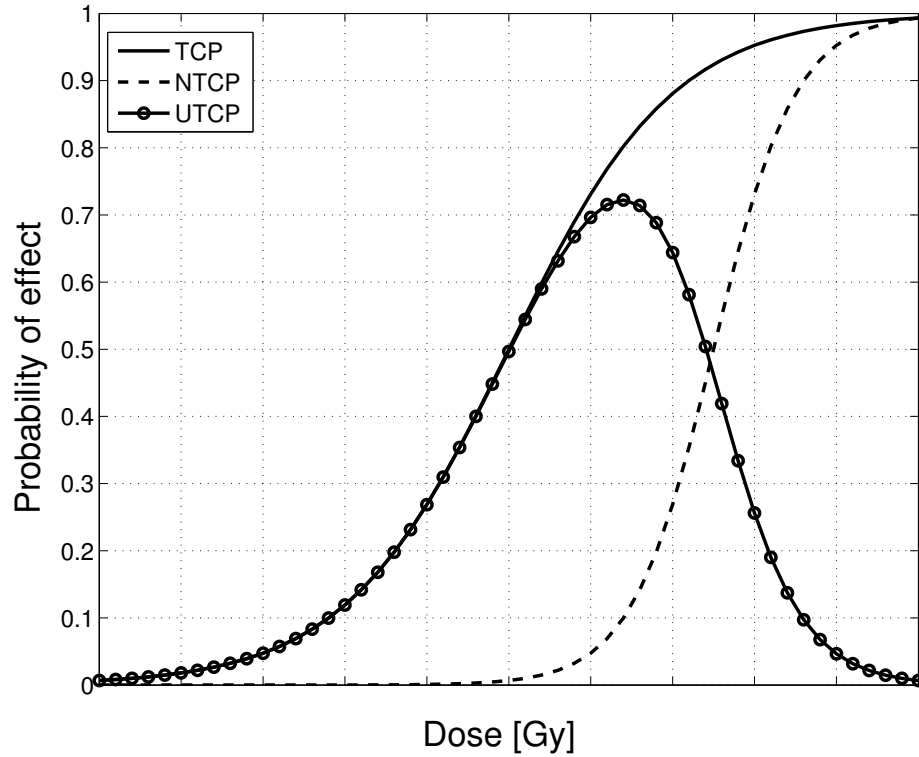


Figure 1–1: Probabilistic model of tumor control probability (TCP), normal tissue complication probability (NTCP), and uncomplicated normal tissue probability (UTCP).

Exhaustive efforts to combat cancer have been ongoing due to its prevalence and lethality. Statistically, cancer has been reported as the most common cause of death worldwide [13] and the second most common cause of death, first being heart disease, in the United States [4]. About one-third will develop cancer and

one-fourth will die from cancer [13]. Worldwide it accounted for more than 7.4 million deaths, making up 13% of all deaths in 2004 [13]. The cancers with the highest mortality rates include: lung, stomach, colorectal, liver, and breast [13]. Some common forms of cancer treatment include: surgery, radiotherapy, and chemotherapy. Often, cancer is treated with more than one technique. Approximately thirteen types of cancers may be cured by chemotherapy, which roughly accounts for 10% of all cancers [5]. Radiotherapy is said to be capable of curing 12.5% of all cancers [5]. The so-called, "half-half-half-rule", states that one-half of all cancer patients are treated with radiotherapy, one-half of those patients are treated curatively, and one-half of those patients are definitively cured. Presented in Figure 1–2 is Surveillance Epidemiology and End Results (SEER) cancer statistics of the United States relative five year survival rates for the top 26 cancer sites from 1999-2005, for both sexes, and all races.

1.5 The Modern Medical Linear Accelerator

In practice, the kinetic energy of electrons accelerated by a linac may range from 4 MeV up to 25 MeV, for both photons and electrons. Since, in this thesis x-rays are used, linacs operating in x-ray mode will be discussed. A schematic of the components of a modern medical linear accelerator is shown in Figure 1–3 [11].

1.5.1 Acceleration and Beam Transport of Electrons

In a linac, the electrons originate from a triode gun and are linearly accelerated by non-conservative microwave fields in accelerating waveguides at frequency ranges from 10^3 MHz (L band) to 10^4 MHz (X band), with many operating at 2856 MHz (S band). The triode gun is the source of electrons, which are thermoionically emitted from the heated cathode filament and are initially accelerated across a relatively small potential of approximately 20 kV towards a perforated anode. In the path of the electrons exists a negative voltage grid that is pulsed to synchronize the injection of electrons into the accelerating waveguide microwave frequency. The

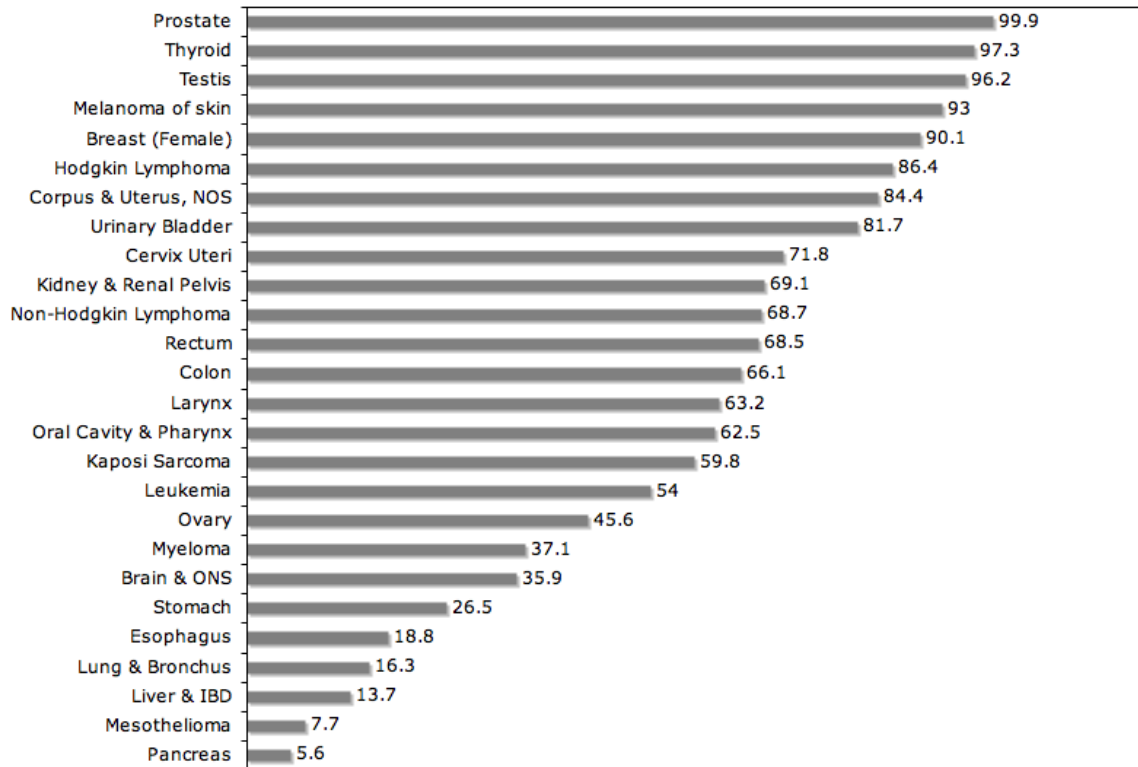


Figure 1-2: Five-year relative survival rates SEER Program, 1999-2005, both sexes, and all races from nine different areas in the U.S. (San Francisco, Connecticut, Detroit, Hawaii, Iowa, New Mexico, Seattle, Utah, Atlanta)

waveguide is an evacuated or gas filled metallic structures used in the transmission of microwaves. There are two different waveguides in a linac that have unique tasks in electron acceleration. The radio-frequency (RF) power transmission waveguide transports the RF power from a microwave power source called a klystron to the accelerating waveguide used to accelerate the electrons. The klystron creates the high power microwaves by decelerating electrons in retarding potentials in evacuated chambers. There are two types of accelerating waveguides: traveling and standing wave structures. The latter, is preferred due to its space saving compact design. At the end of standing accelerating waveguides is a conducting disk used to reflect the microwave power, resulting in a summation of standing waves in the

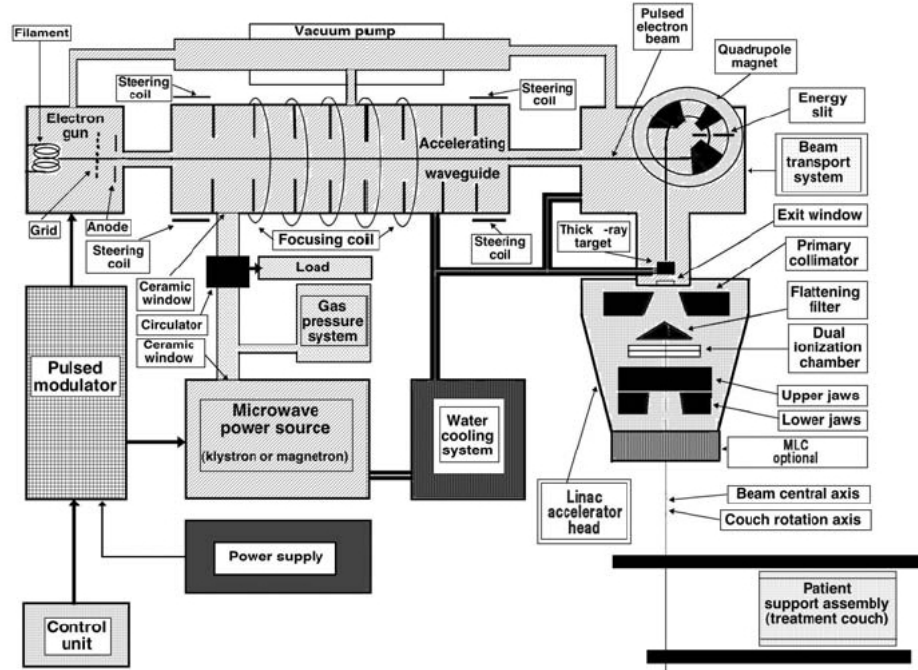


Figure 1-3: The modern medical linear accelerator (Reproduced from Ervin. B. Podgorsak, Radiation Physics for Medical Physicists, page 111) [11].

waveguide. With this configuration there exists no electric field in every second cavity, thus no energy is transferred to electrons for acceleration. This makes it possible to move coupling cavities to the side of the accelerating waveguide, shortening the structure by 50%. A cross-section of a 6 MV accelerating waveguide is shown in Figure 1-4.

For linacs operating above 6 MeV, it is necessary to transport the beam of electrons through vacuum onto a thick x-ray target, since the accelerating waveguides are too long to be mounted on a isocentric linac head. Steering coils, focusing coils, and bending magnets are used to guide the electron beam onto the thick x-ray target. In the case of the Varian Clinac 23EX¹ used in this research,

¹ Varian Medical Systems, Palo Alto, CA, USA. Varian Clinac 23EX is a registered trademark of Varian Medical Systems.

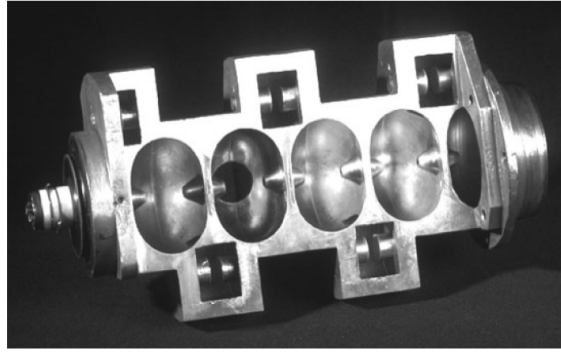


Figure 1–4: A cutaway view of a 6 MV standing wave accelerating waveguide (Reproduced from Ervin. B. Podgorsak, *Radiation Physics for Medical Physicists*, page 87) [11].

electrons are guided from the accelerating waveguide through an evacuated drift tube and then bent 270° around 3-piece magnet and onto an x-ray target. The reason for the circular trajectory is to filter out lower energy electrons and to allow for a more compact design. As shown in Figure 1–3, the energy slit selects electrons at a particular rotational radius defining the allowable energy range of incident electrons on the x-ray target.

1.5.2 X-ray Production

X-rays are produced when high kinetic energy electrons interact with a high atomic number (high-Z) material such as tungsten, resulting in kinetic energy transfer from electrons to predominately bremsstrahlung photons. Production of bremsstrahlung photons is a result of a charged particle (electron) inelastic Coulombic interaction with the absorber nucleus where part of the electron's kinetic energy is emitted as electromagnetic radiation. Due to electrons interacting at various depths within the target, a spectrum of photon energies emerges as the clinical photon beam ranging from zero up to the maximum electron kinetic energy. The efficiency of x-ray production in EBT is of the order of 10% to 20%, where the rest of the energy is transferred as heat, thus a high melting point target and efficient cooling system are required.

Although x-ray production utilizing high-Z absorbers are optimal for electron kinetic energy below 15 MeV, it is not the case for electron kinetic energies above 15 MeV, instead a low-Z target is desired since x-ray production is in the forward direction and independent of absorber atomic number. In radiotherapy, one uses only the forward projected photons, while any peripheral photons outside the useful radiotherapy beam are unfavorable since they increase the need for more shielding necessary to prevent leakage radiation during a patient's treatment. In practice however, low-Z targets are low in density requiring inconvenient target thicknesses to prevent electrons from escaping and contaminating the clinical photon beam.

1.5.3 Shaping, Flattening, Monitoring, and Secondary Collimation of Beam

The bremsstrahlung photons exiting the target pass through an evacuated conical bore and are collimated by the tungsten primary collimator (Fig. 1-5). The emerging photons from the beryllium window are highly forward peaked, that is, the radiation intensities and energies are much higher at smaller characteristic angles from the beam central axis (CAX). In radiotherapy, clinical photon beams must be approximately uniform for various field sizes and depths. To create uniform x-ray beams a flattening filter is placed in the beams path to reduce forward peaked intensity by using a thicker filter along the beam's central axis (Fig. 1-5) [2].

The x-ray beam exiting the flattening filter traverses sealed gas filled ionization monitoring chambers. The beam symmetry, instantaneous dose rate, and integral dose are all monitored by these chambers. To maintain constancy of these parameters, measurements from the monitor chambers provide feedback information to the upstream waveguide steering and focusing coils as wells as the bending magnet to correct alignment of electron beam.

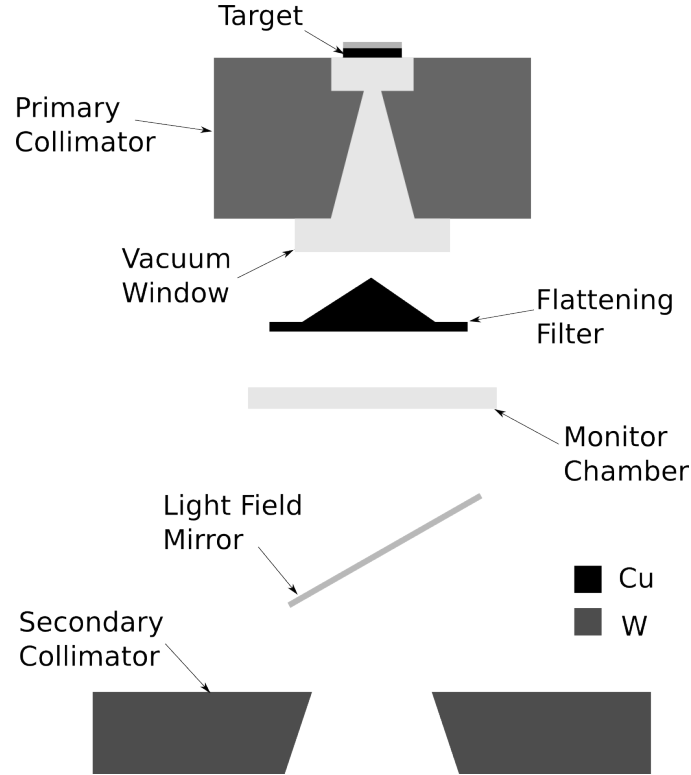


Figure 1–5: Varian Clinac 23EX 6 MV location and geometry of electron target, primary collimator, vacuum window (berillium), and flattening filter.

The secondary collimators are located downstream from the monitor chambers and consist of four blocks made from tungsten. Two blocks form upper jaws and two form lower jaws of the secondary collimator. Both the upper and lower jaws of the Varian Clinac 23EX have ± 20 cm of displacement from the beam's CAX and are designed so that the block edge is aligned along a radial line passing through the target. The primary transmission of x-rays through the collimator is less than 1%. The jaws can provide rectangular or square fields up to 40×40 cm² at a source to surface distance (SSD) of 100 cm. Asymmetric fields are possible due to the independence of upper and lower jaws. Since, the conical shaped primary collimator is limited to 35×35 cm², clipping occurs at the corner regions with field sizes greater than this limitation.

The lighting localizing system defines a visible field size. A light source, and mirror located between jaws and monitor chambers projects light as if it were from the x-ray focal spot, making it congruent with the actual radiation field size.

1.5.4 The Multi-Leaf Collimator

A multi-leaf collimator (MLC) consists of a large number of tungsten collimating leaves, each controlled independently by individual motors. In this study, a Varian Millennium MLC was employed. The radiation transmission through the leaves is less than 2%, while the inter-leaf leakage is less than 3%. The MLC plays a pivotal role in the automation of field shaping and modulation of beam intensity.



Figure 1–6: A Varian Millennium multi-leaf collimator [Varian Medical Systems, Palo Alto, CA].

1.6 Advanced External Beam Radiotherapy Techniques

Over the past several years EBT has become more and more conformal. The major change to linac hardware has been a better designed MLC with more leaves, less primary transmission, and more accurate leaf motion and position. These improvements advanced the MLC from a field aperture, to a reliable intensity modulator.

1.6.1 Intensity Modulated Radiation Therapy

In the late 1990s a more advanced form of 3D-CRT became commercially available called intensity modulated radiation therapy (IMRT). It has been reported that IMRT represents one of the most important advancements in radiotherapy since the medical linear accelerator. IMRT seeks to shape the radiation field even more so than 3D-CRT by modulating the intensity to conform better to 3D tumor volumes. The major advancement that made this new technique possible was the MLC. This special collimator, now comes standard on most linacs and is mounted on the head of the accelerator. The number of leaves continues to increase, currently up to 120 attenuator leaves controlled individually by separate motors are commercially available. There are two main ways to deliver IMRT, either segmental IMRT (SMLC-IMRT) or dynamic IMRT (DMLC-IMRT). In SMLC-IMRT, the MLC is a constant shape during irradiation and is changed between irradiations. A so called step and shoot process takes place where the gantry maintains a fixed position while irradiating with different MLC shapes, creating summation of subfields or segmentations at a given gantry angle. DMLC-IMRT is when the MLC does change shape during irradiation. Although there still is not irradiation between gantry angles, a sliding window process dynamically varies leaf position, velocity, delivered MU, and dose rate to achieve intensity modulation at a fixed gantry angle.

Conventional 3D-CRT uses beam modifiers which can become cumbersome and unable to produce ideal distributions in some cases. IMRT is a more efficient way to deliver modulated radiation through the use of a MLC, which is capable of delivering concave dose distributions. This is a useful advantage for clinical situations where critical structures must be avoided. 3D-CRT uses forward planning, where beam geometry, shape, modifier, and beam weights are first defined, then a 3D distribution is calculated. This process is a more qualitative

approach and must go through several guesses before optimization is reached. IMRT instead focuses on how the outcome is to be accomplished, rather than on the outcome desired. In inverse treatment planning the user specifies goals and the computer optimizes. Although, adjustments often need to be made after the optimization process, thus IMRT uses both forward and inverse planning. Today, both 3D-CRT and IMRT are in use, however IMRT is preferred for treatments requiring specific dose sparing, such as head and neck diseases, although there is a growing trend for IMRT use on traditional diseases treated with 3D-CRT, since IMRT offers the possibility for reduced side effects from radiation.

1.6.2 RapidArc

Varian's RapidArc² technique is a volumetric modulated arc therapy (VMAT) that simultaneously changes gantry rotation speed, shape of field aperture using MLC, and dose rate. The complex leaf sequencing developed by Otto [10] and the intensity modulated arc therapy (IMAT) method proposed by Yu [14] evolved into the sophisticated RapidArc technique. An advantage of this dynamic process is the significant reduction of treatment time and monitor units. During a RapidArc treatment the gantry rotates around the patient in either a single arc or multiple arcs. RapidArc is different than IMAT since it delivers dose to entire volume instead of slice by slice.

1.7 The Importance of Accurate Radiotherapy

Radiotherapy is a complex process involving sophisticated equipment. The accuracy of the treatment and measuring equipment is vital for clinical objectives involving tumor control and the elimination of normal tissue complications. In

² *Varian Medical Systems, Palo Alto, CA, USA. RapidArc is a registered trademark of Varian Medical Systems.*

radiotherapy, the accuracy is maintained through quality assurance and is defined as “all those procedures that ensure consistency of the medical prescription and the safe fulfillment of that prescription as regards to the target volume, together with minimal dose to normal tissue, minimal exposure of personnel, and adequate patient monitoring aimed at determining the end result of treatment” [12]. The required level of dosimetric accuracy depends on the detectability in individual patients, slopes of dose response curves, practical achievability, and required statistical credibility for clinical trials to be deemed reliable [1]. In terms of individual detectability, it has been observed clinically that a 7% change in dose for different patient treatments was discovered by radiation oncologists [3]. Another important aspect of required accuracy is the steep dose response curves as mentioned in Section 1.4, which demand a high level of accuracy, since a 5% change in dose could result in 10 to 20% change in response. This high demand for perfection has limitations based on treatment and measuring equipment. The linac specifications such as output consistency, beam uniformity, gantry rotation isocenter, jaw symmetry, etc. are recommended to be within certain tolerances as determined by the International Electrotechnical Commission (IEC), American Association of Physicists in Medicine (AAPM, TG-40), and other groups. The calibration of the linac output requires absolute dose measurements conducted by ionization chambers. These measurements, along with the linac specifications have uncertainties, and are usually combined in quadrature to estimate the overall uncertainty. Combining in quadrature assumes that each error is independent and is determined by the square root of the sum of the squares of the errors. The random uncertainties are accessed by repeated measurements and is expressed as the standard deviation (SD) of their random distribution. Since, the random distribution is commonly unknown, a Gaussian distribution is used where the 95% confidence level (CL) is approximately 2 SD, which determines the reliability of the

Table 1–1: Overall uncertainty^a in dose delivered at a point in a patient.

Step	Uncertainty [%]
Ionization chamber calibration	1.6
Calibration procedure	2.0
Dose calculation parameters and methods	3.0
Effective depth	2.0
SSD	2.0
Beam shaping	2.0
Cumulative:	5.2

^a 95% confidence level

estimate in most radiotherapy accuracy recommendations. Table 1–1 is an example of the uncertainties in dose delivered at a point in a patient. Depending on the steps considered and uncertainties assigned, the practically achievable dosimetric accuracy has uncertainty ranging from 4-8% (95% CL).

One other major source of uncertainty, is the systematic error of geometry, such as field position, collimator setting, gantry angle, patient position, etc., which also lead to dosimetric inaccuracies. Such errors, could cause underdosing of target volume (lower TCP) or overdosing of normal tissues (increasing NTCP), resulting in an unfavorable therapeutic ratio. Recommendations for the geometric uncertainty are suggested to be between 5-10 mm (95% CL). Base on these considerations and the need for reliable clinical trials, the International Commission on Radiation Units and Measurements (ICRU) has recommended the dose delivery accuracy to be within $\pm 5\%$ [9].

1.8 Pretreatment Verification in Advanced Radiotherapy

Since radiotherapy techniques have become more conformal, there has been an even more stringent demand on the accuracy of treatment delivery as compared to conventional 3D-CRT. This elevated level of accuracy is a result of increased sophistication of hardware and software, and a consequence of utilizing a more conformal dose distribution. With increased conformality came the need for

reduced geometric uncertainties due to the steep dose gradients between target volumes and critical structures. Even small variations in positioning of field setup could lead to target misses and possible avoidable normal tissue damage. As a result quality control procedures must be implemented as pretreatment verification of each patient treatment for advanced radiotherapy techniques.

There are several pretreatment verification procedures for advanced radiotherapy techniques. Typically the verification consists of a point dose, and a two-dimensional (2D) composite beam dose distribution measurement. The point measurement is an absolute dose³ check commonly measured in solid water with an ionization chamber. The 2D dose distribution can be measured with a wide variety of detectors including film, diode array, ionization matrix, or electron portal imaging device (EPID). Usually, the 2D dose distribution is measured in phantom with film. Both the point dose and 2D dose distribution are compared to the treatment plan. The point dose checks a point of absolute dose in a specified plane, while the 2D dose distribution verifies shape and intensity of the radiation beam. The 2D dose distribution may quantitatively be compared with the treatment plan dose distribution using gamma evaluation or a calculation of dose differences amongst isodose lines. The point dose measurement should be within $\pm 5\%$, while the gamma evaluation acceptance criteria is usually 3% at 3 mm, although no standard criterion exists.

1.9 Proposed Work

The current research project consists of developing a convolution and Monte Carlo based non-transmission portal dosimetry method used to reconstruct a

³ *In this thesis, the term “absolute dose” as it is commonly understood in a clinical environment, namely for dose determination in units of Gy according to a dosimetry protocol.*

3D dose distribution. To do so, a dosimetric evaluation of the amorphous silicon Varian aS1000 EPID will provide evidence for portal dosimetry efficacy. In order to use DOSXYZnrc MC code, a primary energy fluence (PEF) will be extracted from the EPID and randomly sampled to create a phase space file (PSF), which will act as an input source for DOSXYZnrc MC simulation. To extract the PEF, a scatter kernel will be derived from MC simulation and an iterative deconvolution algorithm implemented in MATLAB 7.8.0⁴. Verification measurements including beam profiles, PDDs, and 2D dose distributions will be utilized to support the methodology to reconstruct a 3D dose distribution from the EPID extracted PEF.

1.10 Scope and Structure of Thesis

Chapter 2 is an introduction to radiation transport using Monte Carlo (MC) simulation using Electron Gamma Shower (EGSnrc) code [7, 8]. We discuss the photon and electron interaction processes in matter and their application in determining the probability density function used in MC simulation. **Chapter 3** is an introduction to past and present electronic portal imaging devices (EPIDs) employed in portal dosimetry. We describe the hardware and image acquisition of a Varian aS1000 amorphous silicon EPID. We present the dosimetric evaluation of the Varian aS1000. **Chapter 4** is concerned with EPID calibration to extract the primary energy fluence (PEF). First, initial portal image corrections are applied and followed by beam profile correction. Then, a scatter kernel is determined to restore the EPID images from x-ray scatter and optical photon divergence. Finally, the mean photon energy distribution is empirically determined to arrive at the PEF acquired from the Varian aS1000 EPID. **Chapter 5** pertains to the 3D dose

⁴ *Math Works, Natick, MA, USA. MATLAB is a reregistered trademark of Math Works.*

reconstruction using the PEF and DOSXYZnrc MC simulation. Beam profile, PDD, and 2D dose distribution verifications were performed. We finally end this manuscript in ***Chapter 6*** with concluding remarks and discussions on future work.

References

- [1] A. Brahme, J. Chavaudra, T. Landberg, E. McCullough, F. Nusslin, A. Rawlinson, G. Svensson, and H. Svensson. Accuracy requirements and quality assurance of external beam therapy with photons and electrons. *Acta. Oncol.*, 27:Suppl. 1, 1998.
- [2] Karl K. Bush. *Monte Carlo Dose Calculations in Advanced Radiotherapy*. 2009.
- [3] A. Dutreix. When and how can we improve precision in radiotherapy? *Radiother. Oncol.*, 2:275–292, 1984.
- [4] Centers for Disease Control and Prevention (CDC), 2006. Fact sheet.
- [5] Eric J. Hall & Amato J. Giaccia. *Radiobiology for the Radiologist*. Lippincott Williams & Wilkins, sixth edition, 2006.
- [6] ICRU. Prescribing, recording, and reporting photon beam therapy. *International Commission on Radiation Units and Measurements*, 50, 1993.
- [7] I. Kawrakov and D. Rogers, 2003. EGSnrc / BEAMnrc / DOSXYZnrc. EGS electron gamma source. Pirs, NRCC - Canada Ottawa - National Research Council.
- [8] I Kawrakov and D. Rogers, 2003. EGSnrc / BEAMnrc / DOSXYZnrc. The EGSnrc code system : Monte Carlo simulation of electron and photon transport. Pirs-701, NRCC - Canada Ottawa - National Research Council.
- [9] International Commission on Radiation Units and Measurements (ICRU). ICRU Report 24. Determination of absorbed dose in a patient irradiated by beams of x or gamma rays in radiotherapy procedures. (*Washington, D.C.: ICRU*), 1976.
- [10] K. Otto. Volumetric modulated arc therapy: Imrt in a single gantry arc. *Med. Phys.*, 35:310–7, 2008.
- [11] Ervin B. Podgorsak. *Radiation Physics for Medical Physicists*. Springer, first edition, 2006.
- [12] World Health Organization (WHO). Quality assurance in radiotherapy. (*Geneva: WHO*), 1988.

- [13] World Health Organization (WHO), 2009. Fact sheet.
- [14] C. X. Yu. Intensity-modulated arc therapy with dynamic multileaf collimation: an alternative to tomotherapy. *Phys. Med. Biol.*, 40:1435–1449, 1995.

CHAPTER 2

INTRODUCTION TO MONTE CARLO SIMULATION IN RADIOTHERAPY

Contents

2.1	The Monte Carlo Method	22
2.2	Radiation Transport Simulation with EGSnrc	28
2.3	Linear Accelerator Head Simulation with BEAMnrc	29
2.4	Radiation Transport Simulation Through Patient with DOSXYZnrc	30

2.1 The Monte Carlo Method

The Monte Carlo (MC) method was initially realized by Enrico Fermi and later independently developed and named by Stan Ulam and John von Neumann from the Los Alamos laboratory [11]. The development of the MC method was sparked by the invention of the first electronic computer called Electronic Numerical Integrator And Computer (ENIAC) in 1946 and the need for random statistical models for calculation of thermonuclear applications [11]. Before computers, statistical sampling techniques were far from reach due to long tedious calculations, so with the advent of ENIAC statistical calculations were possible. In 1947, the ENIAC completed neutron diffusion simulations by utilizing a MC algorithm [11]. Soon thereafter, other laboratories were requesting time on the ENIAC to run MC problems. As computational power grew so did the usefulness of MC, now a wide array of applications exist from finance to nuclear physics.

The MC method has many different variations, however in general it uses random variables created by a random number generator (RNG) and probability density functions (PDFs) to predict outcomes of systems possessing large coupled

degrees of freedom. In radiotherapy, MC uses fundamentals of physics to determine probability distributions of individual interactions of photons, electrons, and other particles with matter. MC simulation is categorized as a model based algorithm, and can be utilized to characterize the clinical radiation beam and dose deposition for a given patient. Other analytical methods exist, however they suffer from extreme approximations of physical phenomena, geometrical constraints, and have difficulty simulating the randomness of interaction. The MC method is a better choice than analytical methods because it allows for arbitrary geometries and is capable of simulating fundamental physics. Another important reason for using MC is its strong ability to simulate the intrinsic randomness of ionizing radiation interaction with matter.

The MC photon transport simulation relies on fundamental physics of photon interactions with matter. Primarily these interactions include: Compton effect (incoherent scattering), photoelectric effect, pair production, and coherent (Rayleigh) scattering. The Compton effect is a photon interaction with an essentially “free” orbital electron¹, resulting in a scattered photon and recoil electron. The photon loses part of its kinetic energy to the recoil electron. The photoelectric effect is when a photon interacts with a tightly bound orbital electron. In this interaction the photon is completely absorbed and the orbital electron is ejected from the atom. Pair production occurs when a high energy photon interacts with the nuclear coulombic field of an atom, producing an electron-positron pair. During coherent scattering a photon elastically interacts with a bound orbital electron

¹ “Free” orbital electron isn’t entirely true, since outer shell electrons are bound to the atom by a few electron volts and therefore not free. However, the term “free” can be used if the corresponding electron binding energy is a small fraction of the incoming photon energy.

transferring no energy, but is scattered at a certain angle. In Figure 2–1, regions of predominance of the three main photon interactions are illustrated (Compton effect, photoelectric, and pair production). In radiotherapy the Compton effect and pair production are dominant effects due to the low atomic number of tissue and the relatively high clinical beam energy.

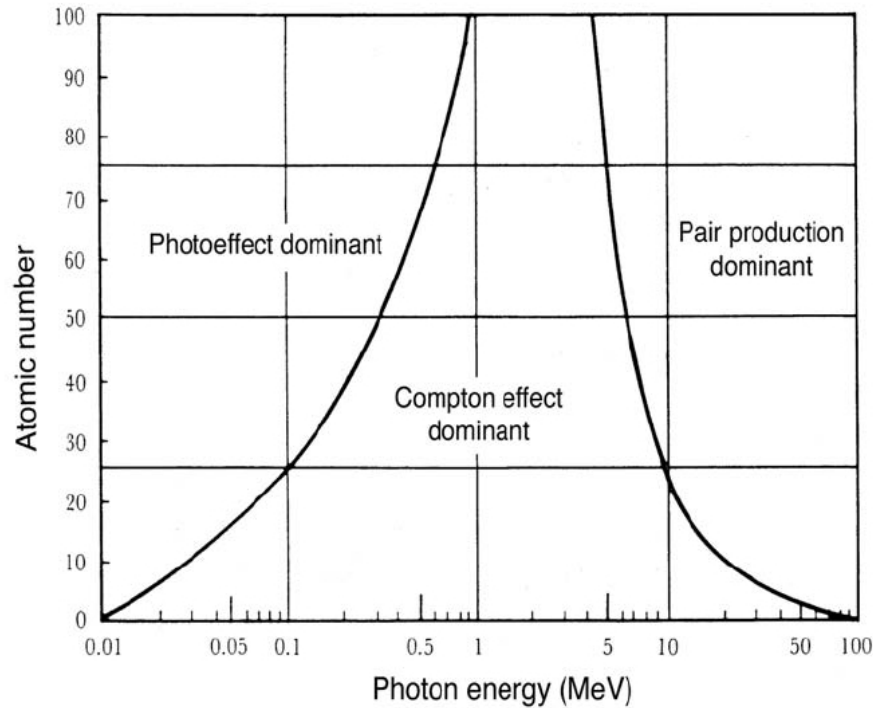


Figure 2–1: Regions of predominance for the three main photon interaction with matter (Reproduced from Ervin. B. Podgorsak, Radiation Physics for Medical Physicists, page 246) [13].

It is important to realize that when a photon interacts (Compton effect, photoelectric effect, pair production and coherent scattering) with matter it eventually transfers its energy to charged particles, which then cascades through the medium creating ionizations, excitations, bremsstrahlung photons, and positron annihilations. As each particle travels deeper, there is an increase in the amount of particles in the forward direction and an average energy decrease after each interaction through the medium.

To simulate this complex shower of particle interactions, MC simulation transports photons and charged particles in two different ways. Photons utilize the various photon interaction cross sections along with the concept of mean free path. While charged particle transport includes elastic coulombic scattering off nucleus, inelastic scattering off orbital electrons, positron annihilations, and bremsstrahlung cross sections along with short grouped paths. Due to the nature of charged particle interaction with matter the slowing down process includes a very large number of interactions. This is a result of the previously mentioned charge particle interactions having cross sections that approach infinity when the transferred energy approaches zero. It is not practical to simulate all these interactions, instead the difficulty is circumvented by the condensed history technique (CH) first introduced by Berger in 1962 [3]. Instead of modeling each interaction, CH groups (condenses) the interactions together to form short steps.

To transport photons, MC simulation randomly determines their step length sampled from the PDFs defined by photon interactions with mater. The step length is the distance a particle will travel between interactions given the exponential attenuation photon distribution and is defined by:

$$s = -\lambda \cdot \ln(1 - \xi), \quad (2.1)$$

where λ is the mean free path at the beginning of the step, and ξ is the random variable, $0 \leq \xi < 1$ [1]. The mean free path is defined by

$$\lambda = \frac{A}{N_a \cdot \rho \cdot {}_a\sigma_t}, \quad (2.2)$$

where A is atomic mass, N_a is Avogadro's number, ρ is density, and ${}_a\sigma_t$ is the sum of the total atomic cross section for each interaction type [12]. The total atomic cross section is proportional to the probability per atom of interaction given by

the initial parameters of the photon and the properties of the absorber atom. The sum of the total atomic cross sections includes each interaction type (photoelectric effect ${}_a\tau$, Compton effect ${}_a\sigma_c$, pair production ${}_a\kappa_{pp}$, coherent scattering ${}_a\sigma_R$) for an absorber atom [13].

$${}_a\sigma_t = {}_a\tau + {}_a\sigma_c + {}_a\kappa_{pp} + {}_a\sigma_R, \quad (2.3)$$

A pivotal point in MC simulation is determining which interaction will prevail. Once the photon has traveled through step s , a certain photon interaction type will occur and the appropriate type is determined by sampling with a random variable \hat{i} the PDF. The $p(i)$ are the branching ratios, defined as,

$$p(i) = \frac{\sum_{j=1}^i {}_a\sigma_j}{{}_a\sigma_t}, \quad (2.4)$$

where ${}_a\sigma_j$ represents the total atomic cross section of the j th type of interaction [12]. The branching ratios are used to decide the interaction type in MC simulation according to the ratio of single atomic cross sections to the total atomic cross sections. Another random variable ξ selects the interaction type $i(\xi)$ that satisfies

$$\sum_{i=1}^{j-1} p(i) = P_{j-1} \leq \xi < \sum_{i=1}^j p(i) = P_j, \quad (2.5)$$

where $i(\xi)$ is either photoelectric effect, Compton effect, pair production, or coherent scattering [1]. After the interaction type has been selected, the final state is determined. The properties of the product particles are stored in the computer as a stack where the particle with the least energy is placed on top. The MC code responsible for the transporting top particle type is then executed and the whole process starts over again. To increase efficiency, certain energy restrictions are used

to prioritize relevant energies in a specified simulation. If a photon energy is below a cut-off value it is not transported.

Since, MC is a statistical sampling method there exist uncertainties that depend on the number of particles transported known as particle histories. The size of uncertainty is proportional to the inverse square root of the number of particle histories [14]. This makes MC simulation time consuming computational process. Due to the small number of interactions of photons with matter, it was realized that variance reduction techniques could be employed to improve the uncertainty and decrease simulation time. In variance reduction, physical effects are modified to increase the occurrence of particular interaction types. Forced interactions, importance sampling, Russian roulette, particle splitting, etc. are just a few examples of different variance reduction techniques used in radiotherapy [5, 12].

A variety of techniques exist for sampling the probability distributions characterized by the photon interactions after a distance s . They all strive for faster more efficient MC simulation. Sampling in MC simulation in radiotherapy commonly use inverse integration and acceptance-rejection of Klein-Nishina distributions.

Charged particle transport in MC simulation is similar to photon transport in that it uses random variables and probability density functions, however as mentioned early the interactions are condensed into short paths. The complexity of the technique becomes apparent when determining the step size since it is proportional to computation time and the accuracy of simulation. Often MC simulations of charged particle transport only group minor collisions together, while individually sampling major events where there is large energy loss. Variation reduction techniques found in photon transport can be used for charged particles, however there still are many interactions as compared to photons. Cut-off energies

and thresholding are important concepts when it comes to increasing the accuracy and efficiency of MC simulation.

Several MC codes exist in radiation transport simulation, a partial list includes: Electron Gamma Shower version 4 (EGS4) [9, 10], Electron Transport (ETRAN) [2], Monte Carlo N-Particle-Extended (MCNP/MCNPX) [4], Penetration and Energy Loss of Position and Electron (PENELOPE) [17], Fluktuierende Kaskade (FLUKA) [8], and Geometry and Tracking (GEANT4) [6]. EGS4 developed at the Stanford Linear Accelerator Center (SLAC) and later refined by the National Research Council (NRC) of Canada to become EGSnrc, was used for MC simulation in this study and will be discussed in greater detail in the following sections.

2.2 Radiation Transport Simulation with EGSnrc

EGS was first introduced in 1978 by Ford and Nelson [7]. It soon developed into EGS4, then in the mid 1990's the Omega group from the NRC adapted the EGS4 code to better suit radiotherapy and also included physics enhancements. The modified version of EGS became known as EGSnrc.

The user communicates with the EGS code by a set of different subroutines. The geometry is managed by HOWFAR & HOWNEAR, and the output scoring is determined by AUSGAB. The HATCH subroutine initializes EGS and reads material data previously prepared by PEGS. In the SHOWER particle histories or cases are generated. The user inputs arguments into shower to specify the parameters of the incident particle initiating the cascade of particles.

The EGSnrc code includes photon interaction models for photoelectric effect, Compton scattering, pair production, and coherent scattering. One adaptation of EGS was the introduction of thresholding to limit particle histories by cut-off energies known as PCUT for photons and ECUT for electrons. Any particle having energy below the cut-off will be discarded. Other thresholding parameters

are for radiative and collisional restrictive stopping power, AP and AE, respectively. The AP cut-off energy represents the required energy for the creation of a bremsstrahlung photon, while AE cut-off energy is the necessary energy for delta-ray production. If AP and AE are decreased, the MC simulation will have greater accuracy at the expense of modeling more particles, thus owing to more computation time. A detailed account of other physics updates and cross sections for each interaction used in EGSnrc can be found in the NRC Technical Report PIRS-701[10]. Electrons are transported using the PRESTA II algorithm.

2.3 Linear Accelerator Head Simulation with BEAMnrc

The BEAMnrc is a user code for EGSnrc to simulate radiotherapy beams produced by a linac. The accelerator parts and geometry are modeled by component modules (CM). The component modules used for the Varian Clinac 23EX are shown in Figure 2-2.

To build a linac head model in BEAMnrc the composition, geometry, and dimension of the components are defined as specified by the manufacturer. Each component module is stacked on top of one another usually including a target, primary collimator, flattening filter, monitor chambers, mirror, and secondary jaws. Each component's material properties are stored in a PEGS4 file, which includes cross section data for a wide range of energies for each component material and surrounding material (i.e. air). Once the head is modeled correctly and has an associated PEGS4 data file, MC simulation parameters are defined. Some parameters include, number of histories, incident particle on target, ECUT, PCUT, variance reduction options, and kinetic energy of incident particle. After the BEAMnrc simulation has been run an output binary phase-space file (PSF) is created. Generally, the PSF is several gigabytes (GB) in size and includes each particle's position, direction cosines, energy, LATCH history, weight, and optionally, the Z-coordinate of the last interaction. The advantage of the PSF is

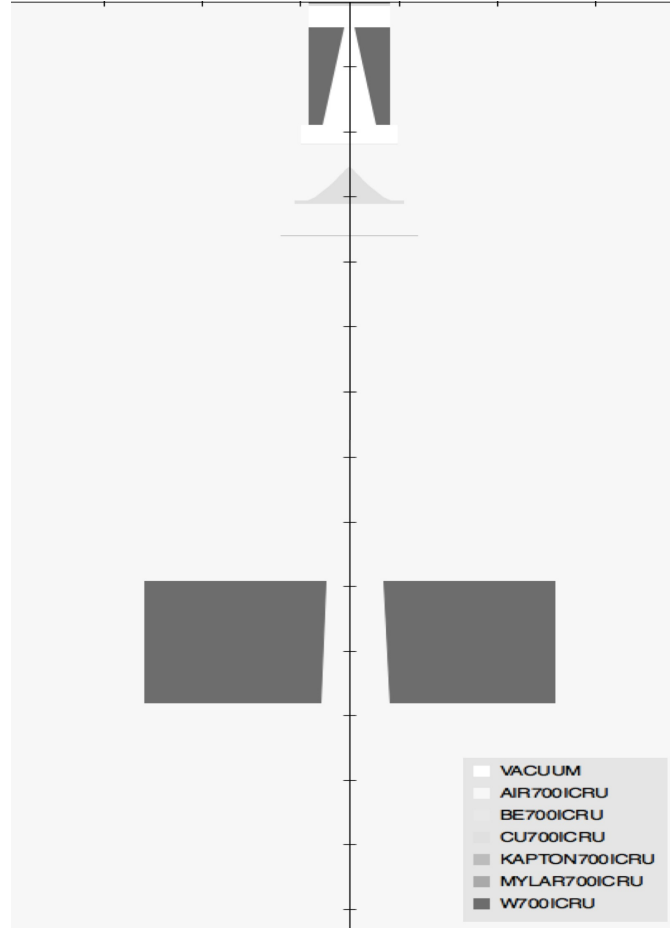


Figure 2-2: A schematic model of a Varian Clinac 23EX showing the component modules used in BEAMnrc.

that it can be scored at any plane and assuming nothing above changes there is no need to re-simulate the whole linac head. The PSF can be used to examine characteristics of particles at a specified plane, and can be used as an source input for other user codes such as DOSXYZnrc, which transports the particles through a patient as discussed in the next section.

2.4 Radiation Transport Simulation Through Patient with DOSXYZnrc

The DOSXYZnrc is a user code for calculating dose distributions in rectilinear voxel defined phantoms. It has a variety of different source input (isource) options. Originally, DOSXYZnrc defined the sources in spherical coordinates, however linac geometry is specified by gantry angle, collimator angle, and couch rotation.

Therefore, a coordinate transformation is required [16]. The isources used in this study were isource 0 (rectangular beam parallel from front) and isource 2 (phase-space source). The geometry of isource2 is shown in Figure 2–3, where a phase-space plane incident on the phantom from any direction is defined by a polar coordinate system.

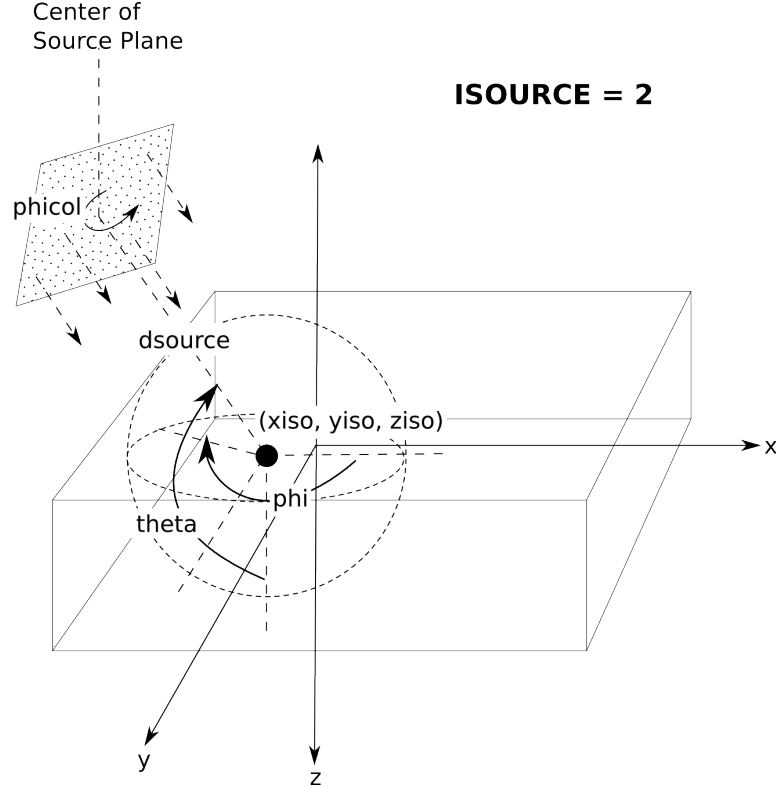


Figure 2–3: Phase-space source incident from any direction (isource=2). Similar to source 1, a polar coordinate system is set up at the isocenter, $(x_{iso}, y_{iso}, z_{iso})$. The position of the origin in the phase-space plane is then defined by the angles θ and ϕ , and the distance from the isocenter, d_{source} . The source can be rotated in its own plane using the variable ϕ_{icol} [10].

Each layered material is characterized by a density specified in the PEGS4 file and thicknesses are defined by arbitrary voxel dimensions. An important function of DOSXYZnrc, is its capability of using a phase-space file generated by BEAMnrc as an isource. In isource 2, a phase-space source incident from any direction may be transported through the surrounding medium and into the phantom. If the

medium surrounding the phantom is air DOSXYZnrc will transport the particles according to physical principles and terminate any particle history that doesn't make it to the phantom surface. Also, the beam size parameter may be adjusted to a smaller field size than the original PSF.

The absorbed dose is scored in a three-dimensional array with dimensions matching the predefined voxel boundaries. The output file '.3ddose' is formatted in American Standard Code for Information Interchange (ASCII), and contains information regarding the voxel boundaries, uncertainties, and dose/incident particle. A companion program called STATDOSE can read the calculation results and generate plots. Another, output file '.egsphant' stores density matrix information used to define the phantom. This .egsphant file along with the .3ddose file may be imported by a DICOM-RT-based toolbox implemented in MATLAB 7.8.0 [15]. This allows users to analyze the voxel defined phantom and dose distributions in the MATLAB environment.

References

- [1] P. Andreo. Monte carlo techniques in medical radiation physics. *Phys. Med. Biol.*, 36:861–920, 1991.
- [2] Berger and Seltzer, 1968. ETRAN - electron transport. Technical report, National Institute of Standards and Technology.
- [3] J. Berger. Monte carlo calculation of the penetration and diffusion of fast charged particles. *Methods in Computational Physics*, 1:135–215, 1963.
- [4] J. F. Briesmeister, 2000. MCNP - a general Monte Carlo N-particle transport code version 4C. Technical Report LA-12625-M, Los Alamos Natl. Lab.
- [5] L. L. Carter and E. D. Cashwell. *Particle-Transport Simulation with the Monte Carlo Method, TID-26607*. National Technical Information Service, U. S. Department of Commerce, 1975.
- [6] CERN, 1982. GEANT - GEometry ANd TRacking. Technical report, CERN - European Organization for Nuclear Research.
- [7] R. L. Ford and W. R. Nelson, 1978. The EGS Code System: Computer Programs for the Monte Carlo Simulation of Electromagnetic Cascade Showers (Version 3) Rep. SLAC-210.
- [8] INFN and CERN, 1982. FLUKA - (FLUktuierende KAskade). Technical report, Italian National Institute for Nuclear Physics (INFN) and by the European Organization for Nuclear Research (CERN).
- [9] I. Kawrakov and D. Rogers, 2003. EGSnrc / BEAMnrc / DOSXYZnrc. EGS electron gamma source. Pirs, NRCC - Canada Ottawa - National Research Council.
- [10] I Kawrakov and D. Rogers, 2003. EGSnrc / BEAMnrc / DOSXYZnrc. The EGSnrc code system : Monte Carlo simulation of electron and photon transport. Pirs-701, NRCC - Canada Ottawa - National Research Council.
- [11] Metropolis N. The beginning of the monte carlo method. *Los Alamos Science*, Special Issue:125–130, 1987.
- [12] Walter R. Nelson, Hideo Hirayama, and David W. O. Rogers, 1985. The EGS4 Code System, Stanford Linear Accelerator Center.

- [13] Ervin B. Podgorsak. *Radiation Physics for Medical Physicists*. Springer, first edition, 2006.
- [14] Y. A. Shreider. *The Monte Carlo Method*. Pergamon Press, 1966.
- [15] E. Spezi, D. Lewis, and C. Smith. A dicom-rt-based toolbox for the evaluation and verification of radiotherapy plans. *Phys. Med. Biol.*, 47:4223–4232, 2002.
- [16] J. Thebaut and S. Zavgorodni. Coordinate transformations for beam/egsnrc monte carlo dose calculations of non-coplanar fields received from a dicom-compliant treatment planning system. *Phys. Med. Biol.*, 51:N441–9, 2006.
- [17] UB, 1982. PENELOPPE - PENetration and energy LOss of Positron and Electron. Technical report, Universidad de Barcelona.

CHAPTER 3 DOSIMETRIC DEVICES AND METHODS

Contents

3.1	Introduction	35
3.2	Ionization Chamber	35
3.3	Water Phantom	36
3.4	Photodiode Detector	38
3.5	Solid Water	39
3.6	Film Dosimetry	39
3.6.1	Gamma and Absolute Dose Difference	42

3.1 Introduction

In this chapter, an overview of dosimetric devices and methods used to measure percent depth doses, beam profiles, and 2D dose distributions is presented. Also, a brief derivation of the γ evaluation and absolute dose difference methods is outlined. A more detailed account of the Varian aS1000 EPID as a dosimetric device will be described in more detail in Chapter 4.

3.2 Ionization Chamber

A waterproof IC-10¹ compact ionization chamber was used for in-air fluence profiles and in-water profiles. The compact ionization chamber was chosen for its ease of use, reproducibility, and availability. Specification for the IC-10 ionization chamber are given in Table 3-1.

¹ *Scanditronix Wellhöfer North, Memphis, TN, USA. IC-10 is a registered trademark of Scanditronix Wellhöfer North.*

3.3. WATER PHANTOM



Figure 3–1: The IC-10 ionization chamber.

Table 3–1: Technical specifications for the IC-10 as stated by the manufacturer [5].

Cavity volume:	0.13 cm ³
Cavity length:	5.8 mm
Cavity radius	3.0 mm
Wall material:	C552
Wall thickness	0.070 g/cm ²
Central electrode material:	C552

Also, the IC-10 ionization chamber acted as a reference chamber that was fixed inside the x-ray field, in order to compensate for fluctuations of the linac output. The ionization reading was determined from the ratio of the two signals. Both chambers were connected to an electrometer to measure the ionization charge. A 300 V potential was applied across the ionization chamber electrodes for stable charge accumulation.

3.3 Water Phantom

An IBA Blue Phantom² water tank was used to perform beam profile and PDD measurements. The IBA tank was equipped with direct current (DC) motors and timing belts to ensure smooth, accurate and precise motion of the detector through the water without perturbing the liquid surface. It can be controlled remotely from the linac control room. The engraved crosshairs help to correctly

² IBA Dosimetry America, Bartlett, TN, USA. Blue Phantom is a registered trademark of IBA Dosimetry America.

3.3. WATER PHANTOM

align the tank with respect to the linac and the room lasers. Specifications of the IBA Blue water phantom are given in Table 3-2.



Figure 3-2: The 3D water phantom system (Blue Phantom) used for beam profile and PDD measurements [5].

Table 3-2: Technical specifications for the Blue Phantom as stated by the manufacturer [5].

Scanning volume:	480 mm (L) \times 480 mm (W) \times 410 mm (H)
Scanning speed (continuous):	up to 15 mm/s
Position reproducibility:	min. 0.1 mm
Position accuracy:	\pm 0.5 mm
Approximation volume:	200 L
Wall thickness/material:	15 mm / acrylic (plexiglass)
Water tank exterior dimension:	675 mm (L) \times 645 mm (W) \times 560 mm (H)
Weight:	46 Kg

3.4 Photodiode Detector

A PDIODE³ was used to conduct beam profile and PDD measurements. The waterproof PDIODE is a high doped p-type silicon photodiode detector and possess independent energy and dose-rate dependence [5]. Specification of the Scanditronix PDIODE are given in Table 3–3.



Figure 3–3: PDIODE photodiode [5].

Table 3–3: Technical specifications for the PDIODE as stated by the manufacturer [5].

Effective measurement point:	< 0.9 mm
Chip size (side/thickness):	2.5/0.5 mm
Geometric form of active area:	circled
Diameter of active area	2 mm
Thickness of active volume:	0.06 mm

³ *Scanditronix Wellhöfer North, Memphis, TN, USA. PDIODE is a registered trademark of Scanditronix Wellhöfer North*

3.5 Solid Water

Solid Water⁴ slabs were used as an attenuator for the total linear attenuation coefficient and 2D dose distribution measurements. The slabs mimic the ionizing radiation absorption characteristics of water to within 1% [4]. Solid Water offers a convenient solution over actual water because it is easier to handle and position. The slab thicknesses used ranged from 0.2 to 5.0 cm.



Figure 3–4: Solid Water slabs [4].

3.6 Film Dosimetry

Kodak extended dose range (EDR2⁵) radiographic film was used for 2D dose distribution measurements at 5 cm depth in Solid Water. Since, radiographic film has been shown to have energy dependence [8, 10, 12], dose-rate dependence [3, 11], and sensitivity to processing conditions [1], careful calibration was required to produce accurate 2D fluence measurements.

⁴ *Gammex RMI, Middleton, WI, USA. Solid Water is a registered trademark of Gammex RMI.*

⁵ *Eastman Kodak Company, Rochester, NY, USA. EDR2 is a registered trademark of Eastman Kodak Company.*

3.6. FILM DOSIMETRY

A perpendicular geometry calibration protocol similar to AAPM Task Group 69 (TG-69) [9] was adopted to acquire an EDR2 radiographic film characteristic curve (Fig. 3–7). For better efficiency, fourteen calibration points with varying dose were shaped by the MLC to create a step-wedge capable of fitting onto a single EDR2 film (Fig. 3–5) at 5.0 cm depth in Solid Water.

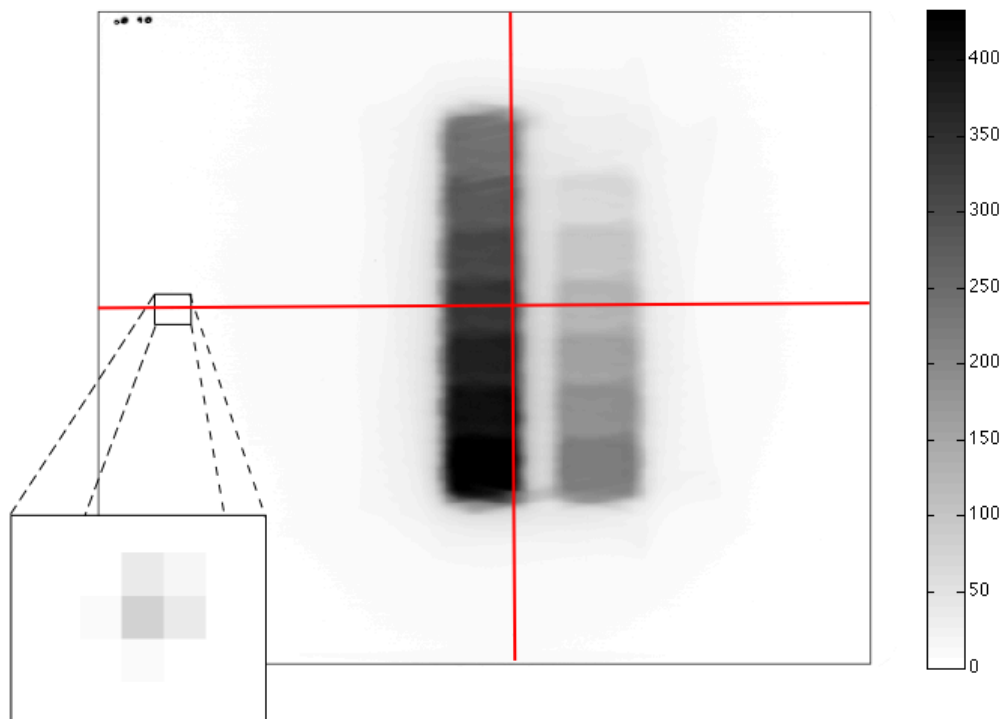


Figure 3–5: Multi-leaf collimator shaped step wedge consisting of fourteen dose steps measured at a depth of 5.0 cm in Solid Water (cGy) and a zoomed view of a pinhole cross-hair position used for centering the film.

3.6. FILM DOSIMETRY

A MapCHECK⁶ 2D photodiode array detector⁷ was also irradiated with the MLC pattern at 5.0 cm depth in Solid Water to establish a reference dose for each of the fourteen calibration points located on the EDR2 calibration film. The manufacture specifications are given in Table 3-4.



Figure 3-6: MapCHECK 2D photodiode array used for film dose calibration [2].

An Epson Expression 10000 XL⁸ flatbed photo scanner was used for digitization of EDR2 calibration film to determine the pixel value vs. dose characteristic curve. The flatbed scanner was set to acquire a 16-bit grayscale image at a resolution of 150 dots per square inch (DPI). All EDR2 films originated from the same batch and were processed on the same day to prevent any inconsistencies due to manufacturing and processing conditions.

⁶ *Sun Nuclear Corporation, Melbourne, FL, USA. MapCHECK is a registered trademark of Sun Nuclear Corporation.*

⁷ *MapCHECK was cross-calibrated with an IC-10 ionization chamber.*

⁸ *Epson America Inc., Long Beach, CA, USA. Expression 10000 XL is a registered trademark of Epson America Inc.*

3.6. FILM DOSIMETRY

Table 3–4: Technical specifications for the MapCHECK as stated by the manufacturer [2].

Detector type:	Diode detectors
Detector quantity:	445
Detector spacing:	7.07 cm (inside 10×10 cm ²); 14.04 cm (outside)
Active detector area	0.64 mm ²
Active detector volume:	0.000019 cm ³
Detector sensitivity:	32.0 nC/Gy
Detector stability:	0.5%/kGy at 6 MV
Dose-rate limit:	56.0 Gy/min
Inherent buildup:	2.0 ± 0.1 g/cm ²
Inherent backscatter:	2.70 ± 0.1 g/cm ²
Dimensions/Weight:	31.2 x 43.3 x 5.2 cm / 4.8 kg

In Figure 3–7, the EDR2 film characteristic curve indicated a nonlinear pixel response to dose. The pixels values ranged from 0 to 47,880 over a dose range of 0 to 434 cGy. The background pixel value (fog and base) was determined to be 51,367.

3.6.1 Gamma and Absolute Dose Difference

A γ evaluation algorithm, implemented in MATLAB 7.8.0, was used to compare the EPID reconstructed and EDR2 film dose distributions for a 10×10 cm² and 60° EDW, at a depth of 5.0 cm in Solid Water. The γ evaluation algorithm introduced by Low et al. [7], combines a dose-difference criterion ΔD_M and a distance-to-agreement (DTA) criterion Δd_M for the comparison of two dose distributions [7, 6]. Shown in Figure 3–8 is a 2D diagrammatic representation of the simultaneous consideration of the dose-difference and DTA.

At the origin is a single measured point \vec{r}_m with a measured dose of $D_m(\vec{r}_m)$. The x and y axis represent the spatial location of the calculated point \vec{r}_c , while δ axis is the difference between the measured dose $D_m(\vec{r}_m)$ and calculated dose $D_c(\vec{r}_c)$. The DTA criterion Δd_M becomes the radius of a disk in the $\vec{r}_c - \vec{r}_m$ plane. If the calculated dose $D_c(\vec{r}_c)$ point intersects or falls short of the disk boundary then the DTA criterion passes. The dose-difference criterion passes when the

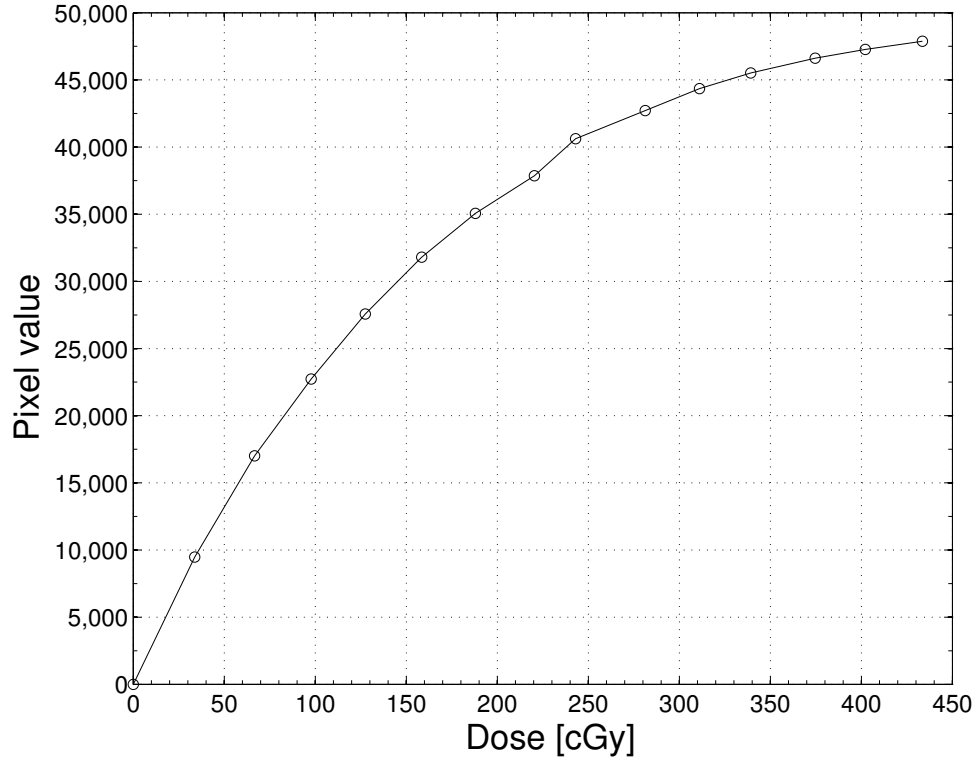


Figure 3–7: Characteristic curve for Kodak EDR2 radiographic film and Epson Expression 10000 XL flatbed scanner at 5.0 cm depth in Solid Water.

$D_c(\vec{r}_c)$ intersects or falls short of the ΔD_M surface boundary. Combining the dose-difference and DTA, $\Gamma(\vec{r}_m, \vec{r}_c)$ determines overall criterion acceptance as described in Equation 3.1.

$$\Gamma(\vec{r}_m, \vec{r}_c) = \sqrt{\frac{r^2(\vec{r}_m, \vec{r}_c)}{\Delta d_M^2} + \frac{\delta^2(\vec{r}_m, \vec{r}_c)}{\Delta D_M^2}} = 1, \quad (3.1)$$

where $r(\vec{r}_m, \vec{r}_c)$ is defined by Equation 3.2, and $\delta(\vec{r}_m, \vec{r}_c)$ is defined by Equation 3.3.

$$r(\vec{r}_m, \vec{r}_c) = |\vec{r}_c - \vec{r}_m| \quad (3.2)$$

$$\delta(\vec{r}_m, \vec{r}_c) = D_c(\vec{r}_c) - D_m(\vec{r}_m), \quad (3.3)$$

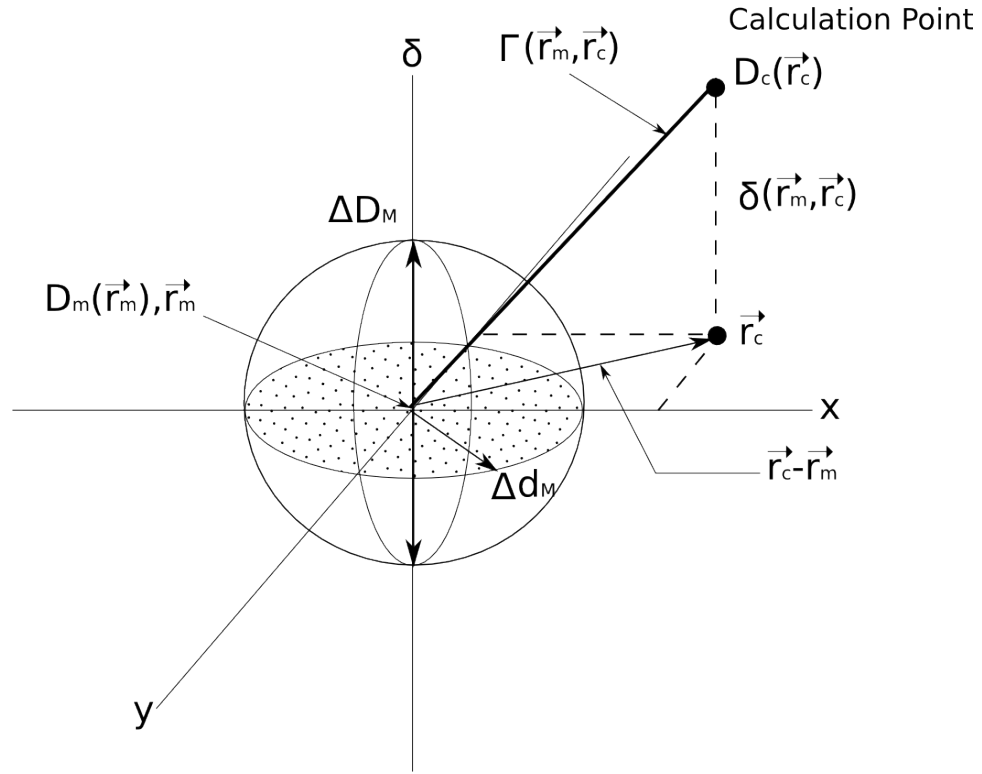


Figure 3–8: 2D geometric representation of γ evaluation criteria using the combined ellipsoidal dose-difference and distance-to-agreement tests.

The quality index γ at each location in the disk plane may be determined and Equation 3.4 derives the minimum value within the dose-difference and DTA criterion.

$$\gamma(\vec{r}_m) = \min \{ \Gamma(\vec{r}_m, \vec{r}_c) \} \forall \{ \vec{r}_c \}, \quad (3.4)$$

$$\gamma(\vec{r}_m) \leq 1, \text{ calculation passes,} \quad (3.5)$$

$$\gamma(\vec{r}_m) > 1, \text{ calculation fails,} \quad (3.6)$$

The 2D dose distributions were also analyzed using absolute dose difference. The absolute dose difference (DIFF) is the absolute value of the difference between

3.6. FILM DOSIMETRY

the EPID reconstructed dose D_{EPID} and the EDR2 film dose D_{film} distributions, normalized to the max EDR2 film dose and multiplied by one hundred resulting in a percent (Equation 3.7).

$$DIFF = \frac{|D_{EPID} - D_{film}|}{max(D_{film})} \cdot 100 \quad (3.7)$$

References

- [1] T. Bogucki, W. Murphy, C. Baker, S. Piazza, and A. Haus. Processor quality control in laser imaging systems. *Med. Phys.*, 24:581–84, 1997.
- [2] Sun Nuclear Corp. MapCHECK- <http://www.sunnuclear.com/>.
- [3] A. Djouguela, R. Kollhoff, A. Ruhmann, K. Willborn, D. Harder, and B. Poppe. Physical mechanism of the schwarzschild effect in film dosimetry-theoretical model and comparison with experiments. *Phys. Med. Biol.*, 51:4345–4356, 2006.
- [4] Gammex. Gammex- <http://www.gammex.com/>.
- [5] IBA. IBA - <http://www.iba-dosimetry.com/>.
- [6] D. Low and J. Dempsey. Evaluation of the gamma dose distribution comparison method. *Med. Phys.*, 30:2455–2464, 2003.
- [7] D. Low, W. Harms, S. Mutic, and J. Purdy. A technique for the quantitative evaluation of dose distributions. *Med. Phys.*, 25:656–661, 1998.
- [8] P. Muench, A. Meigooni, R. Nath, and W. McLaughlin. Photon energy dependence of the sensitivity of radiochromic film and comparison with silver halide and lif tlds used for brachytherapy dosimetry. *Med. Phys.*, 18:767–775, 1991.
- [9] S. Pai, I. Das, J. Dempsey, K. Lam, T. Losasso, A. Olch, J. Palta, L. Reinstein, D. Ritt, and E. Wilcox. Tg-69: Radiographic film for megavoltage beam dosimetry. *Med. Phys.*, 34:2228–2258, 2007.
- [10] Å. Palm, A. Kirov, and T. LoSasso. Predicting energy response of radiographic film in a 6 mv x-ray beam using monte carlo calculated fluence spectra and absorbed dose. *Med. Phys.*, 31:3168–3178, 2004.
- [11] S. Srivastava and I. Das. Dose rate dependence of film dosimetry in radiation treatment: Study of reciprocity law. *Med. Phys.*, 33:2089 (abstract), 2006.
- [12] J. Yeo and J. Kim. A Procedural Guide to Film Dosimetry. Medical Physics, Madison, WI, 2004.

CHAPTER 4

ELECTRONIC PORTAL IMAGING FOR RADIOTHERAPY DOSIMETRY

Contents

4.1	Portal Dosimetry Devices and Dosimetric Charac-	
	teristics	47
4.1.1	Charged-Coupled Device Camera-Based	48
4.1.2	Scanning Liquid-Filled Ionization Chamber	49
4.1.3	Amorphous Silicon Flat Panel	51
4.1.4	Portal Dosimetry Methods	55
4.2	Dosimetric Evaluation of the PortalVision aS1000	
	EPID	56
4.3	Materials and Methods	57
4.3.1	Short-Term Reproducibility	57
4.3.2	Dose-Response Behavior	57
4.3.3	Field Size Dependence	57
4.3.4	Pixel Uniformity-Response	58
4.3.5	Dose-Rate Influence	59
4.3.6	EPID Displacement	59
4.3.7	Inverse Square Law Verification	59
4.3.8	Image Lag	59
4.3.9	Memory Effect	60
4.4	Results	60
4.5	Discussion and Conclusion	65

4.1 Portal Dosimetry Devices and Dosimetric Characteristics

The original role of electronic portal imaging devices (EPIDs) was to acquire portal images while utilizing the MV therapy x-ray beams to ensure accurate patient positioning and beam geometry. Shortly after EPID setup-verification was introduced, it was realized that portal images included dosimetry information.

As EPID technology advanced, EPID dosimetry became more favorable due to fast image acquisition, high resolution, digital format, and the possibility of three-dimensional dose verifications.

Many different EPIDs have been examined since the early 1980s. Three main devices include: charged-coupled device (CCD) camera-based, scanning liquid-filled ionization chamber (SLIC), and amorphous silicon (a-Si) flat panel. A brief overview of camera-based and scanning liquid-filled ionization chamber will follow. Since, in this study an a-Si Varian PortalVision aS1000¹ flat panel EPID was employed for portal dosimetry, it is examined in more careful detail throughout the following sections.

4.1.1 Charged-Coupled Device Camera-Based

Since the 1950s, the CCD camera-based approach has been under development by many different institutions and investigators. The approach consists of an x-ray converter that is coupled to a camera by a lens and mirror. The converter consists of a metal plate used to convert incident high energy x-rays into secondary electrons. A gadolinium oxysulfide ($\text{Gd}_2\text{O}_2\text{S:Tb}$) phosphor screen then converts these secondary electrons into optical photons. The optical photons diffuse through the screen exiting on the mirror side. The lens and CCD capture a fraction of the light and transform it into a video signal to be digitally processed. The schematic of a camera-based EPID is illustrated in Figure 4–1 [21].

The advantage of camera-based EPIDs is that a large portion of the field can be imaged quickly due to converter size and fast read-out by camera. Also, due to the CCD it has a high spatial resolution. In order to use this approach for

¹ *Varian Medical Systems, Palo Alto, CA, USA. PortalVision aS1000 is a registered trademark of Varian Medical Systems.*

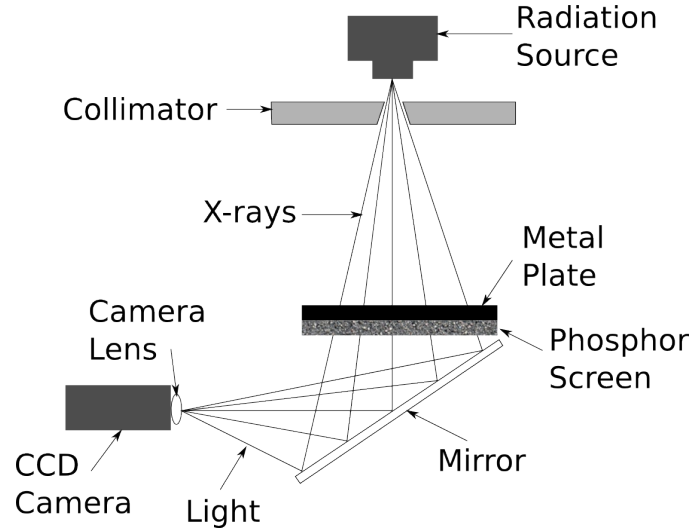


Figure 4–1: Schematic illustration of optical elements for one type of geometry used for camera-based EPID systems.

dosimetry, corrections must be made for the large field size dependence, which is a result from scattered optical photons inside the optical system. This dependence is removed via deconvolution kernels [10, 20]. Furthermore, a sensitivity matrix must be utilized to remove residual cross-talk and correct for non-uniformities in the phosphor screen. After the calibration procedure, the camera-based EPID short-term variation is smaller than 1% (1 SD) and long-term stability of 1-2% (1 SD) for intervals up to one year [20, 1, 9, 5, 6].

4.1.2 Scanning Liquid-Filled Ionization Chamber

The scanning liquid-filled ionization chamber (SLIC) was developed in the late 1980s at the Netherlands Cancer Institute, Amsterdam by Meertens and van Herk [15, 16, 25] and eventually was commercially available in 1990 as PortalVision². As shown in Figure 4–2, the design consists of an ionization medium constructed of two planes of electrodes separated by a 0.8 mm gap filled

² Varian Medical Systems, Palo Alto, CA, USA. PortalVision is a registered trademark of Varian Medical Systems.

with a fluid (2,2,4-trimethylpentane). The two planes have perpendicular electrodes forming a 256×256 ionization chamber matrix, which results in a sensitive area of 32×32 cm². A 1 mm thick plastoferrite (0.8 mm of water equivalent thickness) plate positioned on top of the chamber matrix and acts as a buildup material to convert incident x-rays to secondary electrons. A high-voltage supply applies a bias of 500 V to each electrode on one side of the plate. Each electrode on the other plate are connected to their own individual electrometer. The sampling time for one row was determined to be 20 ms with a scan time of 5.6 s [2]. Since, the scan time is long, dose cannot be measured directly, instead dose-rate is measured and converted to absolute dose. The conversion is accomplished by recording the linac monitor chamber signal continuously as well as the MU delivered for each portal image. The image must be corrected for lateral scatter, and individual ionization electrometer pair sensitivity variations. The stability of the response has been determined to be 1% up to 2 years, as long as temperature and radiation damage corrections are applied [24].

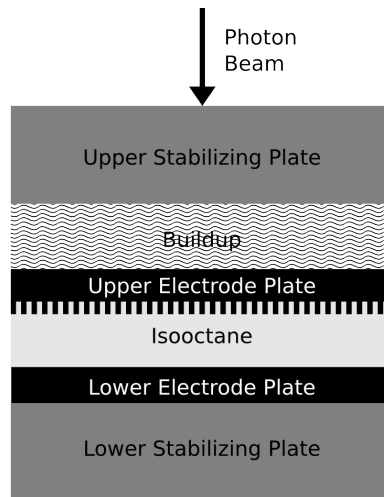


Figure 4–2: Cross-sectional view of the scanning liquid filled ionization chamber.

4.1.3 Amorphous Silicon Flat Panel

The indirect detection a-Si EPID became commercially available in 2000, following its original developed at the University of Michigan, Xerox PARC, and elsewhere beginning in 1987 [2]. The a-Si EPID used in this research project, known as the PortalVision aS1000, consists of several sub-systems including: photodiode pixel array, x-ray converter scintillator, electronic acquisition system, and host display computer.

As illustrated in Figure 4–3, the indirect detection scheme converts x-rays into optical photons, which are captured and stored as integrated charge within each photodiode pixel. The charge is read out along data lines row by row via a pixel switch controlled by gate lines. The analog signal passes through a analog to digital converter and eventually to the host computer display adapter.

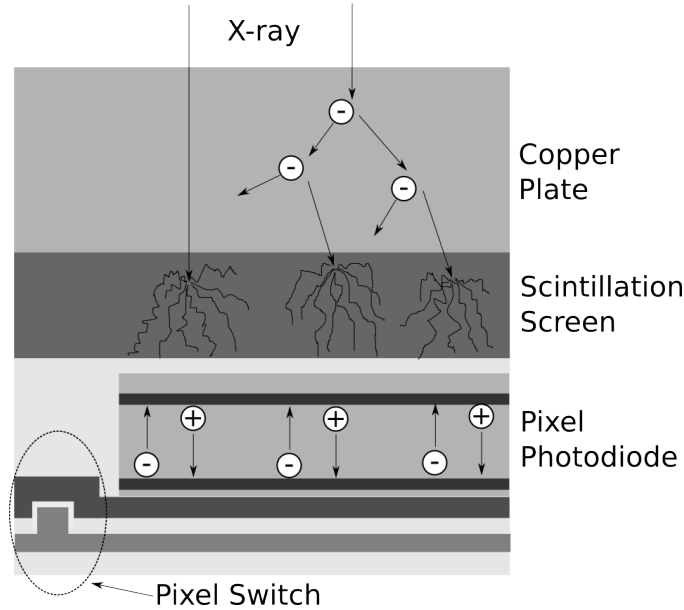


Figure 4–3: Schematic illustration of x-ray detection in an a-Si EPID for indirect detection using a scintillation screen.

Indirect a-Si EPIDs offer a variety of advantages over previous EPIDs. The thin-film circuitry used to control and process the integrated charge stored on the photodiodes creates a compact, and large active detection array. The technology

also offers fast digital acquisition, at a high resolution, with the capability of using on the order of 50% of the optical photons emitted from the scintillator [2]. The a-Si EPID signal response is highly linear making it dosimetrically favorable. Furthermore, the photodiodes and thin film circuitry are highly resistant to radiation damage and have shown to be capable of receiving in excess of 10^4 Gy per year [3, 4].

The PortalVision aS1000 EPID hardware and image acquisition software offers convenient and reliable operation. The PortalVision aS1000 EPID and Exact Arm³ retractable arm are attached to the counter weight portion of a Varian Clinac 23EX (Fig. 4–4). The imager is a 52 cm square and weighs approximately 7 kg. It can be positioned at source to EPID distances ranging from 100 to 180 cm. The Exact Arm poses the ability to move in longitudinal, lateral, and vertical directions, with a tolerance of ± 2 mm. There is no active positioning of detector if displacement occurs during rotation of the gantry. The sensitive active imaging area of the detector is 40×30 cm².

The EPID image acquisition system (IAS3) is made up of the image detection unit (IDU), digitization unit (DU), universal control board (UCB), and frame processing board (FPB). The IDU is comprised of a layered detection volume and electronics including read-out, interface, and gate drive circuitry. The detector is made up of several layers that are incased in thermoplastic (Fig. 4–5).

³ *Varian Medical Systems, Palo Alto, CA, USA. Exact Arm is a registered trademark of Varian Medical Systems.*

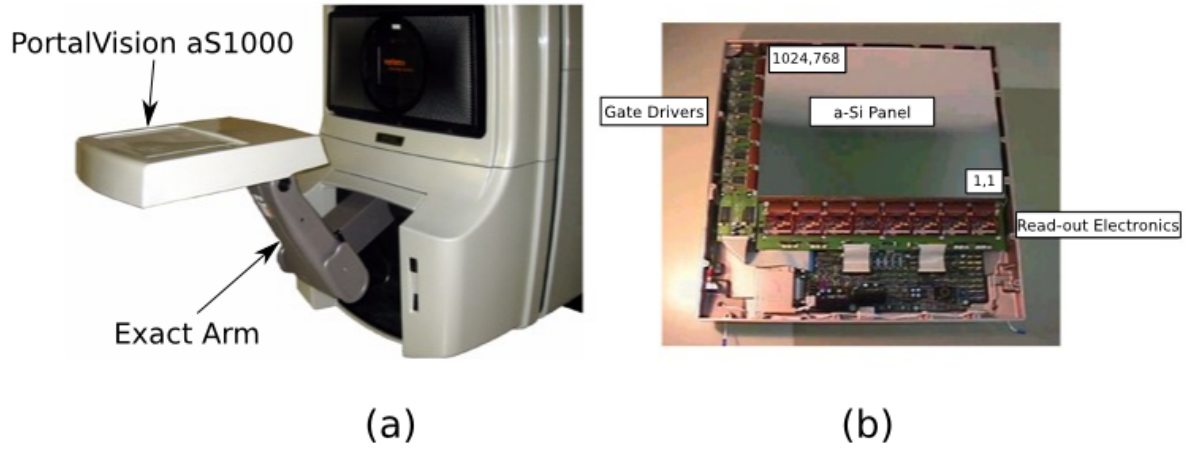


Figure 4-4: (a) PortalVision aS1000 and Exact Arm assembly (b) image detection unit assembly [23].

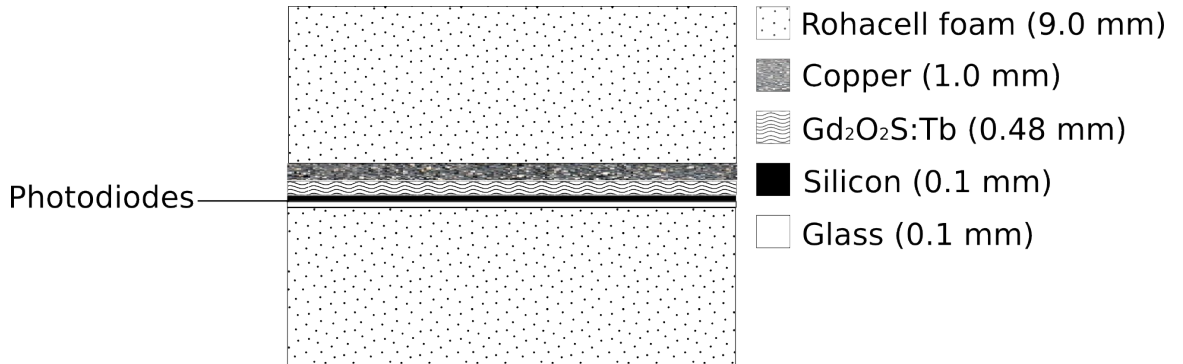


Figure 4-5: PortalVision aS1000 image detection unit layers.

The top and bottom layers are ROHACELL⁴ foam, while the center consist of a 1 mm copper buildup plate, 0.48 mm Kodak Lanex Fast B⁵ scintillating screen (Gd₂O₂S:Tb), 0.1 mm silicon photodiodes, and 0.1 mm glass substrate. All

⁴ *Evonik Röhm GmbH, Darmstadt, Germany. ROHACELL is a registered trademark of Evonik Röhm GmbH.*

⁵ *Eastman Kodak Company, Rochester, NY, USA. Lanex Fast B is a registered trademark of Eastman Kodak Company.*

4.1. PORTAL DOSIMETRY DEVICES AND DOSIMETRIC CHARACTERISTICS

buildup layers total to a water equivalent thickness of 8 mm, as specified by the manufacture. The 1 mm copper buildup layer absorbs incident x-rays and emits recoil electrons. It also removes low energy photons, which have been reported as causing an over-response of detector signal [14, 13] and scatter radiation that may degrade image quality. Downstream from the copper layer, a 134 mg/cm² Kodak Lanex Fast B scintillating screen absorbs recoil electrons and x-rays, transforming them into visible photons making the PortalVision aS1000 an indirect detection system. The scintillating screen enhances the sensitivity of the detector more than tenfold [7]. The next layer has a 1024×768 pixel matrix deposited on a glass substrate constituting the sensitive layer of the IDU. Each pixel is made up of a-Si n-i-p photodiode to integrate the incoming visible photons into stored charge acting as a capacitor (Fig. 4–6(a)), and a thin film transistor (TFT) that behaves as a 3-terminal switch for read-out.

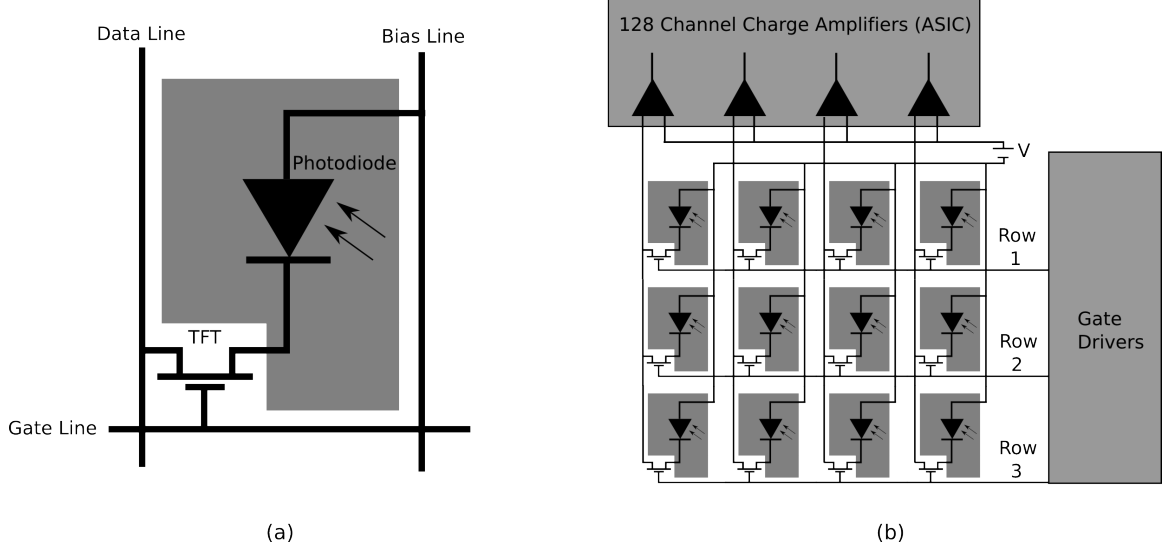


Figure 4–6: (a) Close-up view of a PortalVision aS1000 individual pixel and (b) detector array.

The read-out is initialized by the gate drive circuitry, which applies a bias voltage to a gate line, activating a row of TFTs by switching them to transparent causing the charges stored in photodiodes to be led through each data line and

charge amplifier into the read-out electronics, then digitized through the DU (Fig. 4–6(b)). The DU is capable of 14 bit analog to digital conversion. As soon as one row is complete, the next row of TFTs are switched to transparent and charge is read-out. This process repeats until full read-out of the photodiode array is complete. The digital signals are sent via high-speed link to the UCB workstation. At the UCB, the pixel data stream is encoded and buffered, then eventually transferred to the FPB. The FPB is responsible for image correction and processing (dark-field, flood-field, defective pixel, etc.). The final image is transferred from this card to the workstation’s display adaptor and into hosts memory.

Image acquisition in this study was conducted in integrated mode, and continuous mode. Integrated mode was used for all experiments except for the determination of image lag, in which continuous mode was used. Integrated mode is asynchronous with linac beam pulse frequency and readout is governed by an internal clock controlled only by the frame cycle time (FCT). The FCT is proportional to the raw value of each pixel in a frame and it has been found to be related to the saturation limitation of 1.53 MU per frame [8]. In this study, images are integrated over the entire delivery, at a frame rate v_{fr} of 9.574 frames per second (fps) ($FCT = \frac{1}{v_{fr}} = 104 \text{ ms}$). The detector was set to read out all rows for each acquisition, with no reset frames to ensure all radiation was captured. To avoid buffer overflow, the IAS3 stores a frame-averaged image. The integrated image was reconstructed by multiplying the frame-averaged image by the number of frames acquired. For continuous mode, the real-time acquisition is synchronized with the linac beam pulse delivery, and frames were saved in buffer after every second.

4.1.4 Portal Dosimetry Methods

Several portal dosimetry methods exist and are grouped according to whether or not the radiotherapy beams have passed through an attenuating medium, or not

passed through an attenuating medium. These methods also may be performed during treatment time (i.e. with patient) or outside treatment time (i.e. without the patient).

- **In vivo dosimetry:** measurement conducted during treatment time, whereby the in vivo dose at a point of interest is extrapolated to within the patient.
- **Transmission (or transit) dosimetry:** determination of dose or incident energy fluence at the position of a detector, patient or phantom, based on the radiation transmitted through the patient or phantom.
- **Non-transmission (or non-transit) dosimetry:** determination of dose or incident energy fluence at the position of a detector, patient or phantom, based on measurement without an attenuating medium between source and detector.

In this study, non-transmission portal dosimetry was used to reconstruct a 3D dose inside a phantom.

4.2 Dosimetric Evaluation of the PortalVision aS1000 EPID

The dosimetric characteristics of the PortalVision aS1000 EPID were investigated for reproducibility and dosimetric performance using a 6 MV x-ray beam. Properties examined include short-term reproducibility, signal linearity with MU, signal dependence on field size, pixel uniformity, dose-rate influence, EPID displacement with gantry angle, inverse-square law (ISL), image lag, and the memory effect. For all EPID measurements the relative EPID response was defined as the mean pixel value in a region of interest (ROI) of 25×25 pixels ($\approx 1 \text{ cm}^2$) known as EPID ROI. All portal images were acquired in integrated mode except for the image lag measurement, which was acquired in continuous mode.

4.3 Materials and Methods

4.3.1 Short-Term Reproducibility

Short-term reproducibility was determined by acquiring ten consecutive images at a 10×10 cm² field size. Each portal image was irradiated at 50 MU, dose-rate of 300 MU/min, and at a fixed source to detector distance (SDD) of 100 cm. The mean and standard deviation were determined from the relative EPID response.

4.3.2 Dose-Response Behavior

To assess the EPID response to an increase in MU, each portal image was irradiated with a range from 2 to 999 MU. All portal images had a fixed field size of 10×10 cm², 100 cm SDD and were exposed to a constant dose rate of 300 MU/min. The relative EPID response was determined for each portal image and plotted against MU to examine the linearity.

4.3.3 Field Size Dependence

Open field portal images were obtained for square field sizes ranging from 2 cm to 30 cm and were incremented by 2 cm. Each portal image was exposed to 50 MU at a dose-rate of 300 MU/min, 100 cm SDD. Photodiode measurements were also performed on beam CAX for the same square field size range in water at a depth of 1.5 cm. The photodiode measurements were converted using PDD to 8.0 mm in water to account for the same water equivalent buildup present in the EPID. Both the relative EPID response and photodiode measurement were normalized to a square 10 cm field. The following fourth order polynomial was used as a fit equation for both total scatter factor curves.

$$S_{cp} = a_0 \cdot x^4 + a_1 \cdot x^3 + a_2 \cdot x^2 + a_3 \cdot x + a_4, \quad (4.1)$$

where the S_{cp} is the total scatter factor, and x is the square field size.

4.3.4 Pixel Uniformity-Response

The EPID uniformity was investigated by comparing pixel values at specific positions relative to the CAX pixel. The pixel uniformity was measured using a 20×20 cm² field size at 50 MU, 300 MU/min and 100 cm SDD. A sample of seventeen points were acquired at the specified locations as shown in Figure 4–7. During irradiation, the scatter in the EPID increases the pixels values in the periphery of the field, as compared to a penumbra region measured by a common dosimeter (i.e. ionization chamber, photodiode, etc.). Therefore, pixel positions in the penumbra region were also considered since they represent an important dosimetric characteristic of the EPID, even though this region is sensitive to collimator and detector positioning.

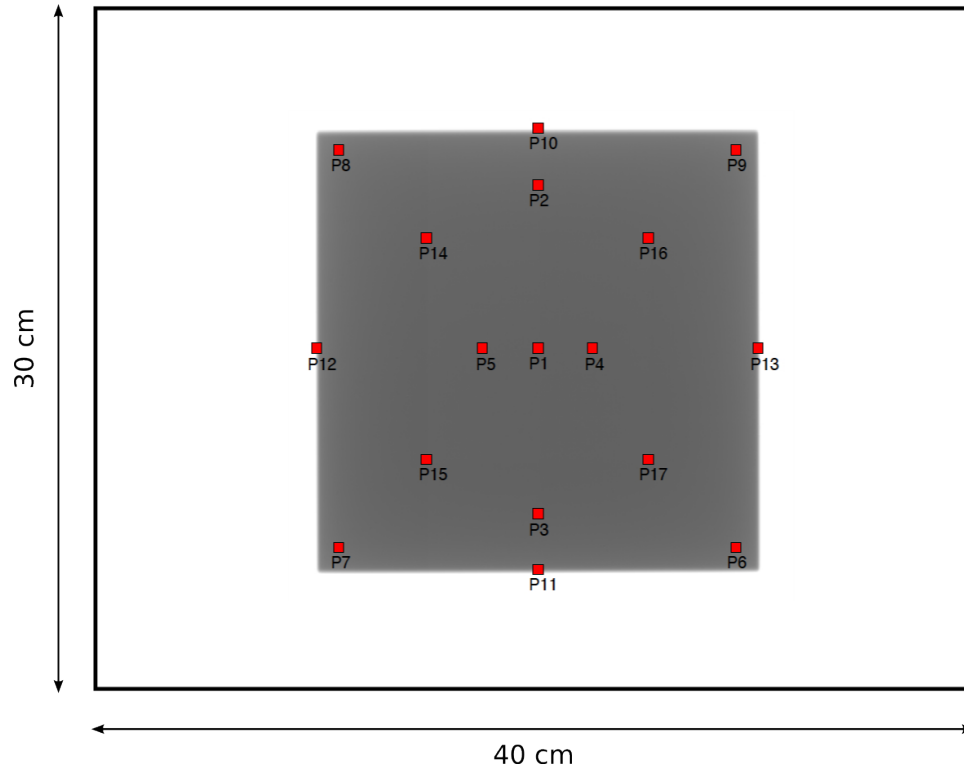


Figure 4–7: Specific EPID ROI positions used to measure pixel uniformity for a 20×20 cm² field size.

4.3.5 Dose-Rate Influence

Relative EPID response measurements were acquired at a fixed 10×10 cm², at SDD of 100 cm for dose-rates of 100, 200, 300, 400, and 600 MU/min, at 20 and 100 MU on the same day to minimize any day-to-day variation. The EPID response was normalized to the response for 600 MU/min.

4.3.6 EPID Displacement

EPID displacement was evaluated as a function of gantry angle. The displacement was measured in the cross-plane and in-line directions for gantry angles ranging from 0 to 360 degrees in 45 degree increments at a SDD of 130 cm. A cube phantom with a 2.0 mm metal ball (bb) was placed on foam extending beyond the treatment table and positioned at isocenter. EPID images were acquired at various gantry angles around the cube phantom.

This experiment was necessary because EPID acquisition of a patient's actual treatment plan would include the planned gantry angles and it was important to measure the displacement to better understand the tolerance of geometric accuracy for the proposed 3D dose reconstruction method stemming from EPID measurement. To ascertain the displacement in both the in-line and cross-plane directions, the full-width half-max (FWHM) was calculated for each gantry angle profile along the bb in both directions.

4.3.7 Inverse Square Law Verification

The inverse square law (ISL) was verified with the EPID by adjusting the SDD from 100 cm to 180 cm and plotting the relative EPID response values normalized to the response at 100 cm SDD.

4.3.8 Image Lag

Image lag has been shown to be a signal delay created by trapped charges from a previous frame that are read-out in subsequent frames causing an offset

4.4. RESULTS

in EPID signal [22]. Image lag was assessed by acquiring EPID images in continuous mode for 44 seconds at a frame-rate of 1 fps and dose-rate of 300 MU/min (Fig. 4–12).

To account for image lag, a triple-exponential equation was used to fit the relative EPID response:

$$G(t_{rad}) = 1 - \sum_{i=1}^3 A_i \cdot \exp(-r_i \cdot t_{rad}), \quad (4.2)$$

where A_i is amplitude, r_i is the decay constant, and t_{rad} is the irradiation time.

4.3.9 Memory Effect

The memory effect represents a change in gain or sensitivity in EPID response. This enhanced sensitivity results from charge stored in deep trapped states that alter the electric field strength within the photodiode bulk and interface layers [18, 17]. To measure the memory effect, three consecutive EPID images were acquired with the following settings: (1) 5 MU 20×20 cm², (2) 500 MU 5×5 cm², and (3) 5 MU 20×20 cm².

4.4 Results

Table 4–1 shows that the EPID short-term reproducibility has a percent standard deviation for ten consecutive images of 0.2 %. The EPID ROI mean pixel values are shown in calibration units or CU, since an unrelated calibration to MU was conducted for clinical portal dosimetry use.

As show in Figure 4–8, the EPID relative response to increased MU followed a linear trend. The ratio of 5 MU to 10 MU was 0.38, while the ratio of 400 MU to 800 MU was 0.50. The overall linearity was best 50 MU and above.

As shown in Figure 4–9, both relative EPID response and photodiode response increased with field size. However, discrepancies up to 6% were observed

4.4. RESULTS

Table 4–1: Reproducibility of ten consecutive portal images acquired by the PortalVision aS1000.

Image number	EPID ROI mean [CU]
1	49.27
2	49.46
3	49.39
4	49.29
5	49.35
6	49.18
7	49.47
8	49.42
9	49.32
10	49.41
Mean:	49.36
Standard deviation [%]:	0.2

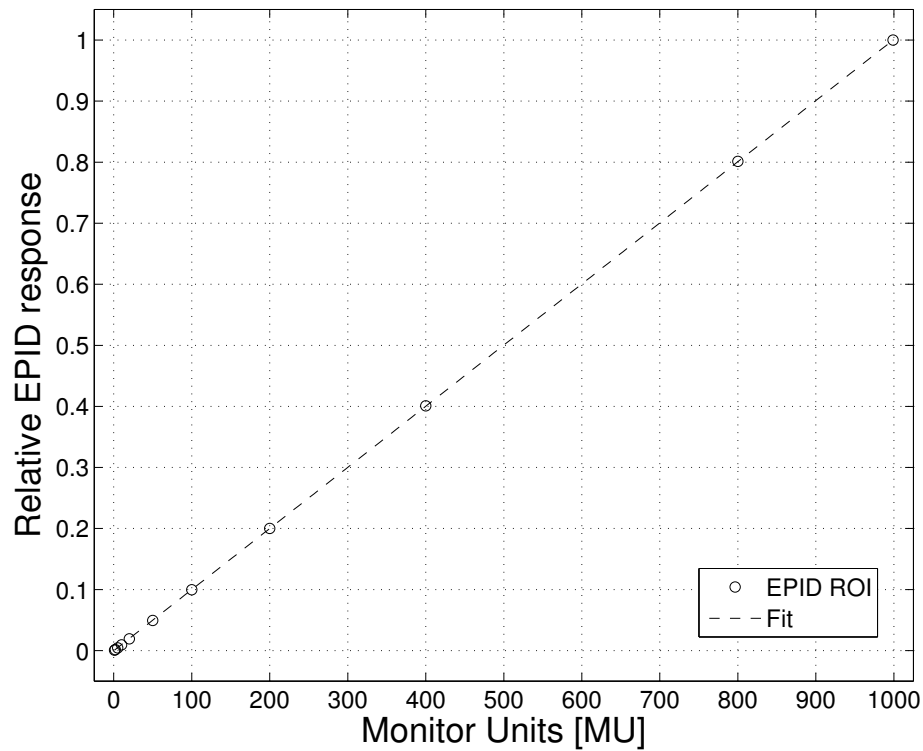


Figure 4–8: PortalVision aS1000 dose-response to increasing monitor units.

4.4. RESULTS

when comparing the relative EPID response and photodiode. Both the relative EPID response ($a_0 = -3.865 \times 10^{-7} \text{ cm}^{-2}$, $a_1 = 4.133 \times 10^{-5} \text{ cm}^{-2}$, $a_2 = -0.001676 \text{ cm}^{-2}$, $a_3 = 0.03611 \text{ cm}^{-2}$, $a_4 = 0.7725 \text{ cm}^{-2}$) and photodiode ($a_0 = -8.029 \times 10^{-7} \text{ cm}^{-2}$, $a_1 = 6.585 \times 10^{-5} \text{ cm}^{-2}$, $a_2 = -0.002026 \text{ cm}^{-2}$, $a_3 = 0.03137 \text{ cm}^{-2}$, $a_4 = 0.834 \text{ cm}^{-2}$) were fit with a fourth order polynomial (Equation 4.1). The fit indicated that the relative EPID response was lower at square field sizes below 10 cm and higher at square field sizes above 10 cm.

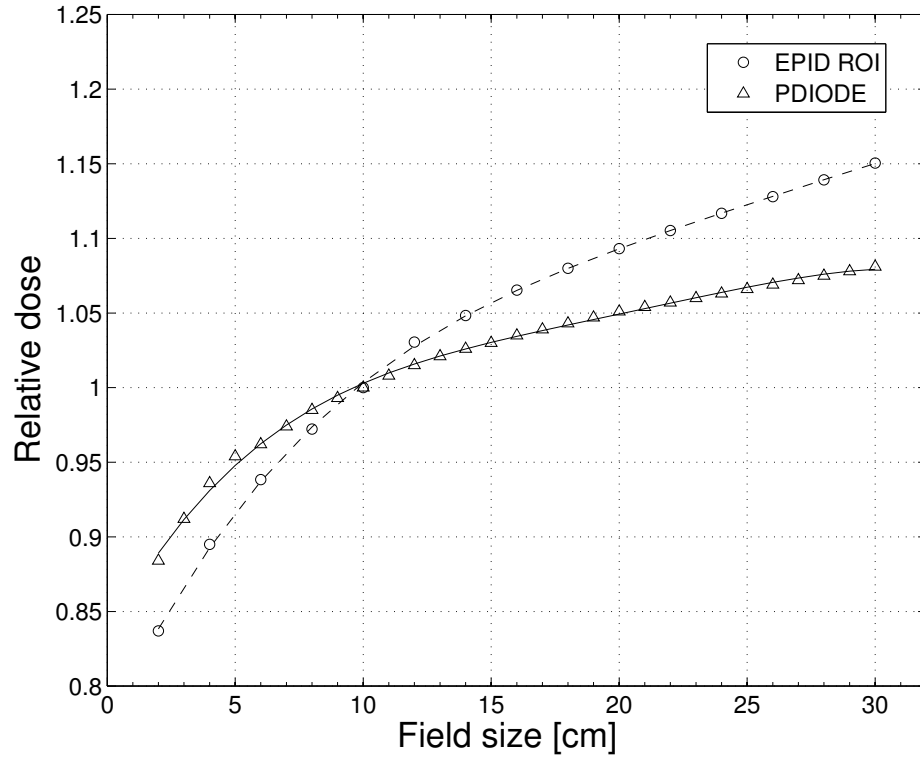


Figure 4-9: PortalVision aS1000 field size dependence (total scatter factor) as compared to photodiode (PDIODE) measurement at 8.0 mm depth in water.

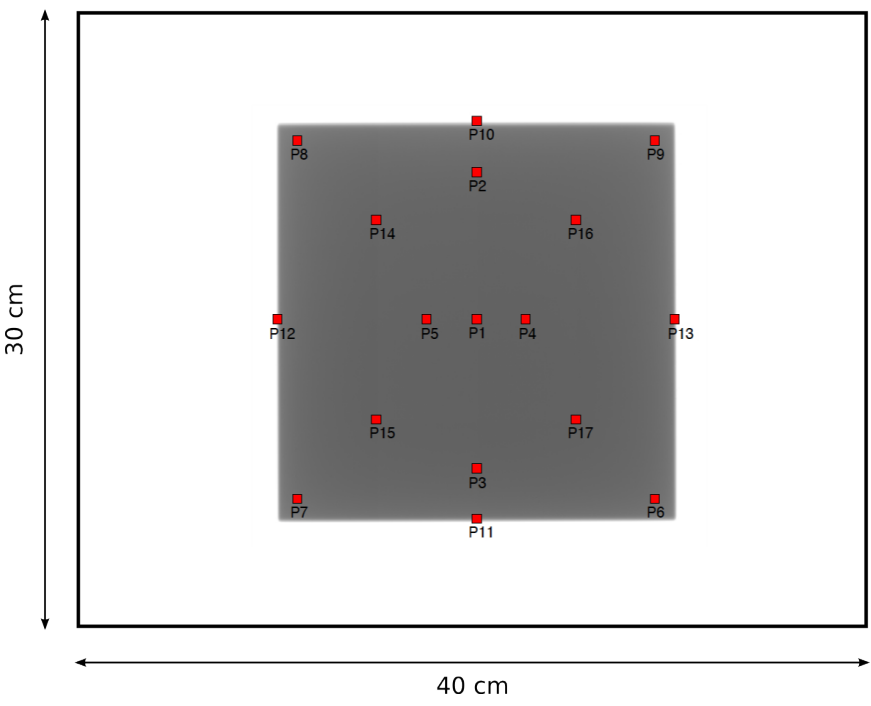
As shown in Table 4-2 the pixel uniformity was in excellent agreement within the boundary of the field. Pixels located at P6-9 showed the most deviation of up to 8% as compared to the CAX pixel. The penumbra pixels located at P12 and

4.4. RESULTS

P13 were in close agreement, however pixels located at P10 and P11 demonstrated greater disagreement. The remaining pixel locations were within 3%.

Table 4–2: PortalVision aS1000 EPID ROI values corresponding to the indicated positions (right) used to measure pixel uniformity for a 20×20 cm² field size.

Position	P_i/P_1
P1	1.0
P2	0.97
P3	0.99
P4	1.0
P5	1.0
P6	0.95
P7	0.94
P8	0.92
P9	0.92
P10	0.46
P11	0.64
P12	0.56
P13	0.54
P14	0.99
P15	1.0
P16	0.99
P17	1.0



The diagram shows a rectangular field of size 40 cm by 30 cm. Inside this field, 17 measurement points are marked with red squares and labeled P1 through P17. The points are distributed across the field, with P10 and P11 showing lower response values compared to others. The field is outlined by a black border, and the dimensions are indicated by arrows on the left and bottom.

In Figure 4–10, there was a decrease in response with increasing dose-rate of 2.8% and 2.4% for 100 MU and 20 MU, respectively. There was also a slight discrepancy up to 0.4% between the 100 MU and 20 MU EPID response.

The displacement for each direction was determined to be sub-millimeter varying up to 0.8 mm, which was better than the manufacture specified tolerance of ± 1.0 mm. As shown in Table 4–3, displacement in the cross-plane direction was least for gantry angles at 0° , 45° , 90° , and 135° , while the in-line displacement was least for 0° , 45° , 270° , and 315° .

In Figure 4–11, the relative EPID response agreed within 2% of the theoretical ISL line. There was no indication of significant disagreement with the ISL for a SDD range from 100 cm to 180 cm.

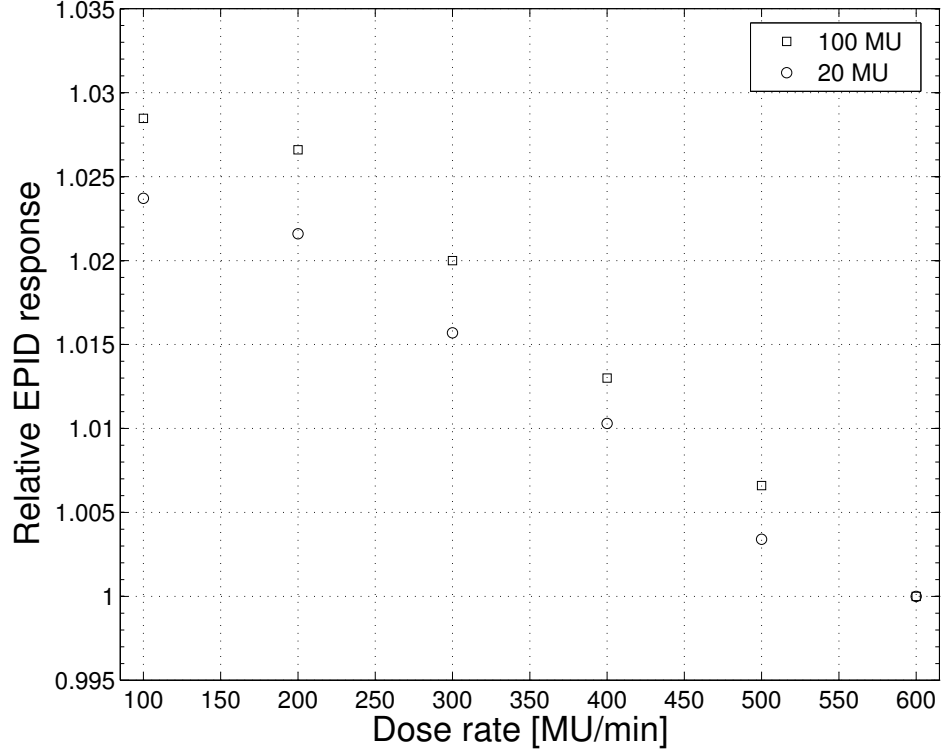


Figure 4–10: PortalVision aS1000 relative EPID response for various dose-rates acquired at 20 and 100 MU.

Table 4–3: PortalVision aS1000 displacement in the cross-plane and in-line direction for various Varian gantry angles.

Gantry angle [degrees]	0	45	90	135	180	225	270	315
Cross-plane displacement [mm]	0	0	0	0	-0.8	-0.8	-0.8	-0.4
In-line displacement [mm]	0	0	-0.4	-0.8	-0.8	-0.4	0	0

The relative EPID response amplitude parameters of the $G(t_{rad})$ fit for Figure 4–12 were determined to be: $A_1 = 0.0888$, $r_1 = 0.5668 \text{ s}^{-1}$, $A_2 = 0.0532$, $r_2 = 0.7235 \text{ s}^{-1}$, $A_3 = 0.0069$, $r_3 = 0.1237 \text{ s}^{-1}$ and the fit matched the measured data to within 0.2%. Beyond 5 seconds the relative EPID response began to stabilize. However, below 5 seconds the relative EPID response indicated an exponential increase in signal.

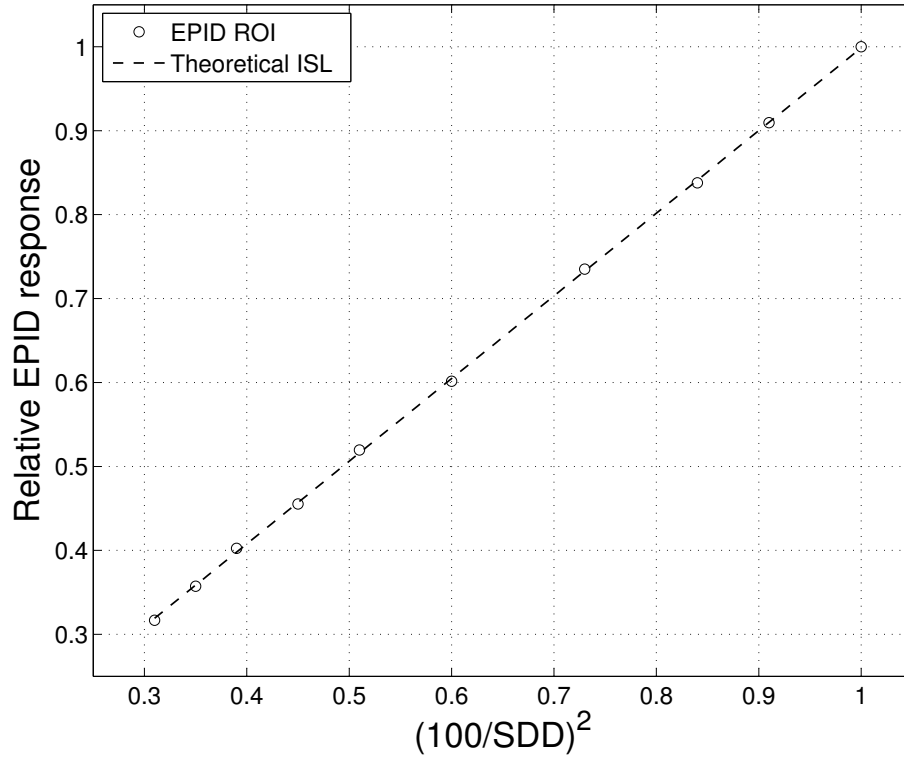


Figure 4-11: A verification of the inverse square law as measured by the PortalVision aS1000 relative response to change in source-to-detector distance.

As shown in Figure 4-13, there was residual signal present from off-axis position -2.5 cm to 2.5 cm. The “with memory effect” curve (solid line) demonstrated a heightened signal where the $5 \times 5 \text{ cm}^2$ field was irradiated. As shown in Figure 4-13, the inset graph indicated a percent difference of approximately 1% between the profile with and without the memory effect.

4.5 Discussion and Conclusion

The short-term reproducibility of a static field over ten consecutive images were in excellent agreement. The percent standard deviation was only 0.2% providing evidence for consistent short-term reproducibility. Although long-term reproducibility wasn’t tested, it has been shown to be 0.5% (1 SD) over a 23 month period for a-Si EPIDs [12].

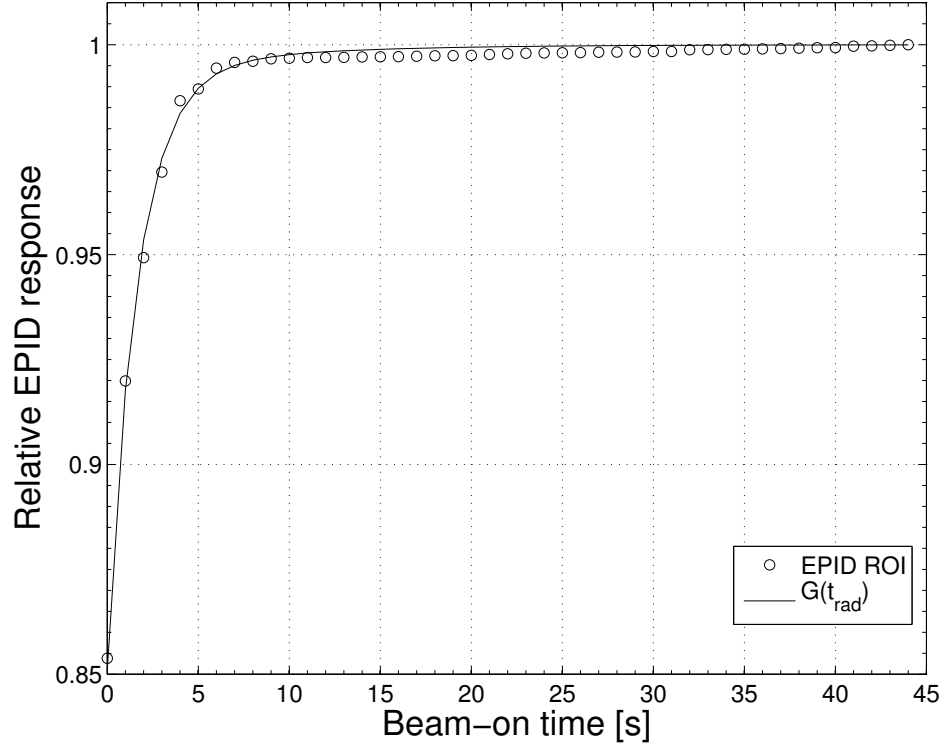


Figure 4-12: PortalVision aS1000 continuous imaging mode acquisition from 0 to 44 seconds, demonstrating the image lag effect and triple-exponential fit $G(t_{rad})$ equation.

Overall, measurements are slightly more linear at higher MU (above 50 MU). The image lag effect and instability during accelerator start-up may account for the reduction in linearity at lower MU values. These results were found to be supported by a previous study [11].

As demonstrated by the field size dependent data, the EPID is not equivalent to the dose to water. This disagreement was most likely due to the enhanced sensitivity of the scintillation screen caused by low energy photons and electrons [26]. Although copper has a sharp rise in mass attenuation after 200 keV, indicating that copper should preferentially filter low energy photons, there may be enough low energy electrons to create an over response of optical photon production from the scintillation screen. Moreover, it is possible the divergence of optical photons

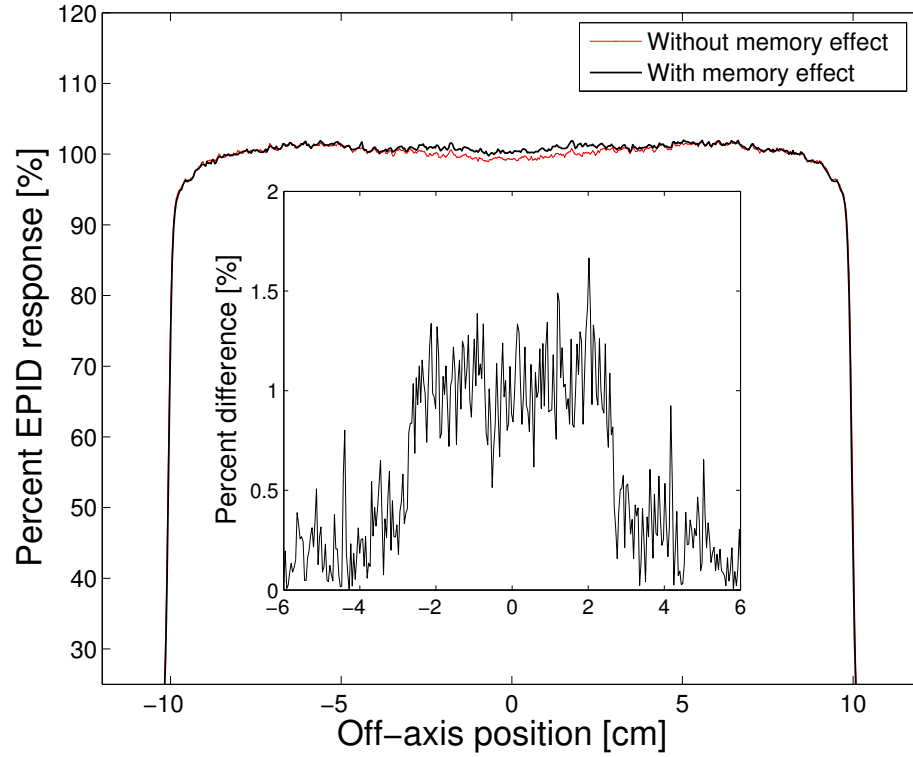


Figure 4–13: The demonstration of the memory effect by the PortalVision aS1000 after the acquisition sequence of a (1) 5 MU $20 \times 20 \text{ cm}^2$, (2) 500 MU $5 \times 5 \text{ cm}^2$, and (3) 5 MU $20 \times 20 \text{ cm}^2$.

between the scintillation screen and photodiode array may contribute to the field size dependence discrepancy.

The EPID displayed excellent uniformity across the field size. The 8% deviation present in locations P6-9 is most likely due to slight in-line detector offset. This offset was identified by comparing pixel locations at P10 and P11, which indicate a shift in the in-line direction.

Ideally, there should be no dose-rate dependence of any dosimeter, however in general the PortalVision aS1000 EPID demonstrated up to 2.8% decrease in sensitivity as the dose-rate increased. Although the decrease in sensitivity was

4.5. DISCUSSION AND CONCLUSION

small, the result may be due to the FCT relationship with dose-rate and could be reduced with the proper FCT setting for each dose rate.

According to Table 4–3, it can be concluded that detector displacement will not be a significant source of geometrical error. At all measured angles the displacement was sub-millimeter, below the manufacture specified tolerance of ± 1 mm. It also should be noted that this displacement experiment was conducted at a SDD of 130 cm due to setup limitations, and it would be expected to observe less displacement at SDD less than 130 cm since the exact arm would have less leverage, and thus less gravitational torque.

Based on the ISL measurement there was no experimental evidence supporting any significant deviation from the ISL, however if there was a phantom obstructing the beam, there may be some discrepancy due to phantom scatter variation as field size increased with SDD.

Previous studies indicate that image lag depends on the number of frames acquired [22, 19]. In the image lag experiment, number of frames acquired is equivalent to beam-on time, since the frame acquisition rate remained fixed. From a clinical perspective, common prescriptions range from 20-300 MU, which in Figure 4–12 would be begin at 4 seconds beam-on time. So at 20 MU or 4 seconds a stable state of relative EPID response indicates little image lag effect. However, for IMRT step-and-shoot treatment plans, a prescription segment may be as low as 5 MU or 1 second beam-on time. According to Figure 4–12, if no image lag correction was applied to a 5 MU IMRT segment, a discrepancy up to 8% may be present.

Although the memory effect may be of concern for EPID dosimetry, the effect was only produceable under extreme conditions and may not be considered a clinically relevant phenomenon.

4.5. *DISCUSSION AND CONCLUSION*

In summary, the PortalVision aS1000 EPID dosimetric performance was excellent. The presented experiments indicated the EPID may act as a EBT dosimeter, albeit with proper field size dependence correction, and under certain circumstances, image lag and memory effect correction.

References

- [1] D. Bonnett A. Glendinning. Dosimetric properties of the theraview fluoroscopic electronic portal imaging device. *Br. J. Radiol.*, 73:517–30, 2000.
- [2] L. Antonuk. Electronic portal imaging devices: a review and historical perspective of contemporary technologies and research. *Phys. Med. Bio.*, 47:R31–R65, 2002.
- [3] L. Antonuk, J. Boudry, J. Yorkston, C. F. Wild, M. J. Longo, and R. A. Street. Radiation damage studies of amorphous silicon photodiode sensors for applications in radiotherapy x-ray imaging. *Nucl. Instrum. Methods*, 299:143–6, 1990b.
- [4] J. Boudry and L. Antonuk. Radiation damage of amorphous silicon photodiode sensors. *IEEE Trans. Nucl. Sci.*, 47:703–7, 1994.
- [5] M. Dirkx and B. Heijmen. Testing of the stability of intensity modulated beams generated with dynamic multileaf collimation, applied to the mm50 racetrack microtron. *Med. Phys.*, 27:2701–7, 2000.
- [6] M. Dirkx, M. Kroonwijk, J. de Boer, and B. Heijmen. Daily dosimetric quality control of the mm50 racetrack microtron using an electronic portal imaging device. *Radiother. Oncol.*, 37:55–60, 1995.
- [7] Y. El-Mohri, L. Antonuk, J. Yorkston, K. Jee, M. Maolinbay, K. Lam, and J. Siewerdsen. Dose-response and ghosting effects of an amorphous silicon electronic portal imaging device. *Med. Phys.*, 26:1530–1541, 1999.
- [8] Z. Elbalaa, J. Foulquier, A. Orthuon, H. Elbalaa, and E. Touboul. Role of the frame cycle time in portal dose imaging using an as500-ii epid. *Physica Medica*, 25:148–153, 2009.
- [9] E. Franken, J. de Boer, J. Barnhoorn, and B. Heijmen. Characteristics relevant to portal dosimetry of a cooled ccd camera-based epid. *Med. Phys.*, 31:2549–51, 2004.
- [10] B. Heijmen, K. Pasma, and M. Kroonwijk. Portal dose measurement in radiotherapy using an electronic portal imaging device (epid). *Phys. Med. Biol.*, 40:1943–55, 1995.

- [11] A. Kavuma, M. Glegg, G. Currie, and A. Elliott. Assessment of dosimetrical performance in 11 varian a-si500 electronic portal imaging devices. *Phys. Med. Biol.*, 53:6893–6909, 2008.
- [12] R. Louwe, L. McDermott, J. Sonke, R. Tielenburg, M. Wendling, M. van Herk, and B. Mijnheer. The long-term stability of amorphous silicon flat panel imaging devices for dosimetry purposes. *Med. Phys.*, 31:2989–2995, 2004.
- [13] L. McDermott, R. Louwe, J. Sonke, M. van Herk, and B. Mijnheer. Dose-response and ghosting effects of an amorphous silicon electronic portal imaging device. *Med. Phys.*, 31:285–295, 2004.
- [14] L. McDermott, S. Nijsten, J. Sonke, M. Partridge, M. van Herk, and B. Mijnheer. Comparison of ghosting effects for three commercial a-si epids. *Med. Phys.*, 33:2448–2451, 2006.
- [15] H. Meertens, M. van Herk, J. Bijhold, and H. Bartelink. First clinical experience with a newly developed electronic portal imaging device. *Int. J. Rad. Oncol. Biol. Phys.*, 18:1173–81, 1990.
- [16] H. Meertens, M. van Herk, and J. Weeda. A liquid ionisation detector for digital radiography of therapeutic megavoltage photon beams. *Phys. Med. Bio.*, 30:313–21, 1985.
- [17] M. Overdick, T. Solf, and H. Wischmann. Temporal artefacts in flat dynamic x-ray detectors. *Proc. SPIE*, 4320:47–54, 2001.
- [18] G. Pang, L. Lee, and J. Rowlands. Investigation of a direct conversion flatpanel imager for portal imaging. *Med. Phys.*, 28:2121–2128, 2001.
- [19] M. Partridge, B. Hesse, and L. Müller. A performance comparison of direct- and indirect-detection flat-panel imagers. *Nucl. Instrum. Methods Phys. Res.*, A484:351–363, 2002.
- [20] K. Pasma, M. Kroonwijk, J. de Boer, A. Visser, and B. Heijmen. Accurate portal dose measurement with a fluoroscopic electronic portal imaging device (epid) for open and wedged beams and dynamic multileaf collimation. *Phys. Med. Biol.*, 43:2047–60, 1998.
- [21] A. Sawant, H. Zeman, S. Samant, G. Lovhoiden, B. Weinberg, and F. DiBianca. Theoretical analysis and experimental evaluation of a csi(tl) based electronic portal imaging system. *Med. Phys.*, 29:1042–53, 2002.
- [22] J. Siewerdsen and D. Jaffray. A ghost story: spatio-temporal response characteristics of an indirect-detection flat-panel imager. *Med. Phys.*, 26:1624–1641, 1999.

- [23] Varian Medical Systems, 2000. PortalVision aS500 Rel. 6, Reference Manual, Version 6.0.05.
- [24] W. van Elmpt, L. McDermott, S. Nijsten, M. Wendling, P. Lambina, and B. Mijnheera. A literature review of electronic portal imaging for radiotherapy dosimetry. *Radiother. Onc.*, 88:289–309, 2008.
- [25] M. van Herk and H. Meertens. A matrix ionisation chamber imaging device for on-line patient setup verification during radiotherapy. *Radiother. Oncol.*, 11:369–78, 1988.
- [26] C. Yeboah and S. Pistorius. Monte carlo studies of the exit photon spectra and dose to a metal/phosphor portal imaging screen. *Med. Phys.*, 27:330–339, 2000.

CHAPTER 5

PRIMARY ENERGY FLUENCE EXTRACTION FROM EPID

Contents

5.1	Introduction	73
5.2	Materials and Methods	74
5.2.1	Initial Portal Image Correction	74
5.2.2	Beam Profile Correction	75
5.2.3	Determination of Scatter Kernel	75
5.2.4	Primary Energy Fluence Extraction	78
5.3	Results	80
5.3.1	Image Corrections	80
5.3.2	Beam Profile Correction	81
5.3.3	Glare and Dose Kernels	82
5.3.4	EPID Depth Dose	85
5.3.5	Measured and Optimized EPID In-Air Fluence Beam Profiles	86
5.3.6	Primary Energy Fluence	87
5.4	Discussion and Conclusion	89

5.1 Introduction

To extract the primary energy fluence (PEF) from the PortalVision aS1000 EPID, several calibration steps were necessary to remove detector imperfections, spatial degradation due to scatter, and a previous correction applied by the Portal Vision aS1000 image acquisition software (IAS3). The EPID itself, was used to measure primary fluence or the incident photon flux originating from the linac source and measured at a SDD of 100 cm. While the energy associated with each photon in the primary fluence distribution was determined from the mean photon energy distribution.

5.2 Materials and Methods

5.2.1 Initial Portal Image Correction

Since, the EPID components are susceptible to imperfections, it was necessary to begin with a series of calibration acquisitions including a pixel defect map (*PD*), dark field (*DF*), noise image (*NI*), drift image (*DI*), and flood field (*FF*).

Due to manufacture limitations, it's common to have thousands of defective pixels [1]. To combat pixel failure, the PortalVision aS1000 has automatic pixel defect correction. Based on the location of each defective pixel stored in the *PD*, the EPID replaces all the defective pixels by the average of neighboring pixels.

A *DF* consists of an averaged set of frames acquired in quick succession without radiation. To minimize noise, usually 300 frames were averaged to form the *DF*. In general, the *DF* has bright and dark vertical stripes. The *DF* content represents array imperfections and electrometer offsets.

The *NI* provides information regarding the IDU readout noise percentages. While the *DI* is the difference between subsequent *NI* images.

A *FF* is acquired by irradiating the entire sensitive detector area with an open-field of $40 \times 30 \text{ cm}^2$ for 300 frames. The frames were averaged to minimize noise. The *FF* represents field homogeneity, electrometer gains, and individual cell sensitivities.

The *DF* offset correction is subtracted from each raw portal image and is approximately a 5% correction, while *FF* gain correction is divided by each raw portal image and may result in a correction of up to 40% [1]. The standard correction express in Equation 5.1, was applied to all acquired EPID images.

$$PI_{corr} = \frac{PI_{raw} - DF}{FF} \cdot k_{FFmean}, \quad (5.1)$$

where k_{FFmean} is the mean value of the *FF* image [1].

5.2.2 Beam Profile Correction

As mentioned in the previous section, the FF was divided by each raw portal image, unfortunately this procedure also removes the dosimetric important characteristic known as beam “horns”. These horns originate from the flattening filter used to create a flat beam profile at a chosen depth. To preserve the beam horns, a $40 \times 40 \text{ cm}^2$ beam profile was measured at a depth of 8.0 mm in water with the IC-10 ionization chamber¹. This beam profile was radially mapped to create a beam profile correction matrix, to be multiplied by each raw portal image.

5.2.3 Determination of Scatter Kernel

To remove spatial degradation due to x-ray scatter in the copper layer and scintillation screen, as well as optical photon spreading (or “glare”) between the scintillation screen and photodiode array, a scatter kernel was determined for image restoration. The scatter kernel consists of two components: the dose deposition kernel and the glare kernel. To better understand the contribution of each component, a MC calculation was conducted to determine the dose kernel. A MC phantom (egsphant, Section 2.4) model (Fig. 5–1) of the EPID was constructed using the dimensions of each layer and appropriate cross-sectional data for each material. It has previously been shown that materials beneath the detector contribute to the backscatter signal (metal bracket, steel bar, cables, and electrical motor) [5], and was determined to represent a water equivalent backscatter thickness of 1.0 cm [7]. Therefore, the inclusion of 1.0 cm of water was placed beneath the EPID layers.

¹ Depth of 8.0 mm was chosen in order to equate the intrinsic water buildup depth created by the copper plate and other materials lying above the scintillation screen, as specified by the manufacturer.

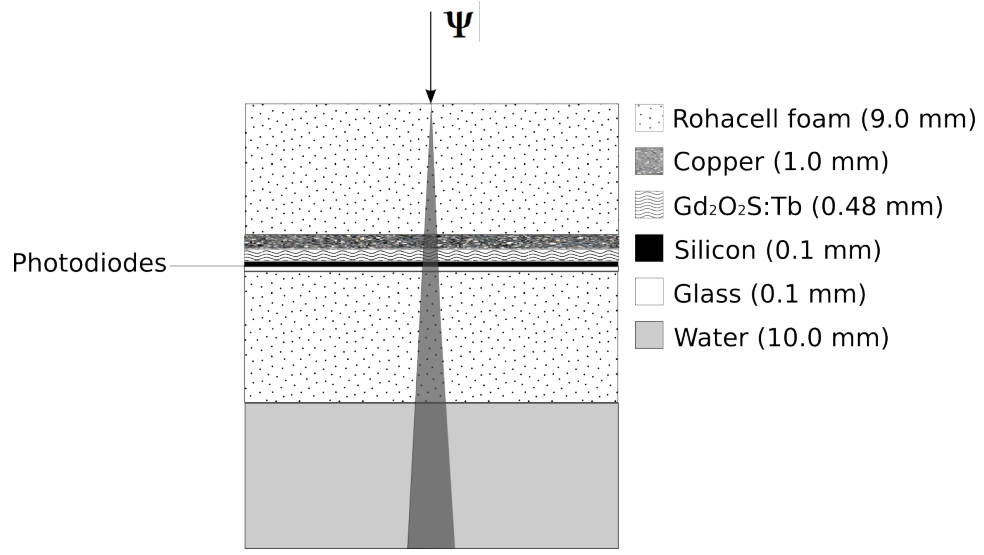


Figure 5–1: Monte Carlo PortalVision aS1000 EPID model for simulation of beam-let to determine the dose kernel, where ψ indicates orientation of incident primary energy fluence.

The pencil-beam dose kernel was scored at the bottom of the scintillation screen. The glare kernel contribution was determined by deconvolving the scatter kernel with the dose kernel. For an initial guess of the scatter kernel, a $10 \times 10 \text{ cm}^2$ beam profile was measured in-air with an IC-10 ionization chamber. The air profile penumbra tail provided an initial guess to the scatter kernel and was mirrored to create a 1D Gaussian kernel. The kernel was fit with the following three-term Gaussian equation:

$$K(x) = \sum_{i=1}^3 A_i \cdot \exp - \left(\frac{\mu_i - x}{\sigma_i} \right)^2, \quad (5.2)$$

where A is the amplitude, μ is the mean, and σ^2 is the variance. An iterative deconvolution optimization procedure implemented in MATLAB 7.8.0 was used to search for the nine parameters of the fit Equation 5.2 that minimized the following objective function:

$$\min \left\{ \sum_x \left(PI_{corr}(x) \otimes^{-1} K(x) - Air(x) \right)^2 \right\}, \quad (5.3)$$

where PI_{corr} is a cross-plane or in-line profile of the beam profile corrected portal image, \otimes^{-1} represents a deconvolution, K is the 1D scatter kernel, and Air is the theoretical cross-plane profile air fluence based on the ionization chamber measurement. The built-in MATLAB function called FMINSEARCH, an algorithm used to find a minimum of an unconstrained multivariable function using the derivative-free method, was implemented to determine the nine parameters of scatter kernel Equation 5.2 that minimized the objective function Equation 5.3. The deconvolution was performed by a built-in MATLAB function known as DECONVLUCY, using an iterative nonlinear restoration technique known as the “Richardson-Lucy algorithm”. The algorithm comes from a maximum-likelihood formulation, in which the image is modeled with Poisson statistics [4]. The following iteration converges, when the likelihood model equation has reached a maximum:

$$\hat{f}_{k+1}(x) = \hat{f}_k(x) \cdot \left[h(-x) \otimes \frac{g(x)}{h(x) \otimes \hat{f}_k(x)} \right], \quad (5.4)$$

where \hat{f} is an estimate of the restored image, \otimes represents a convolution, h is the degradation function or the scatter kernel, and g is the degraded image. Due to the nonlinear nature of the L-R algorithm, it is difficult to know when to terminate the iteration. The approach used in this study was to stop the iteration once an acceptable result was achieved, usually occurring after two iterations.

Optimization was conducted in 1D along both the cross-plane and in-line directions to account for any scatter kernel directional dependence. To convert the 1D cross-plane and 1D in-line scatter kernels into a 2D scatter kernel, a cross-plane kernel matrix was formed by filling the rows, while an in-line kernel matrix was

formed by filling the columns, resulting in a 2D scatter kernel $K(x,y)$. This process is illustrated in Figure 5–2.

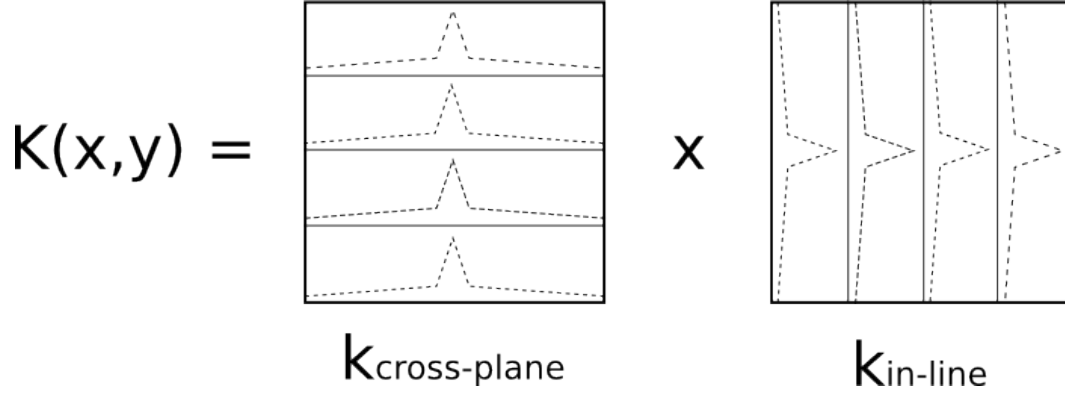


Figure 5–2: Diagram of 1D to 2D scatter kernel conversion based on factorization of the cross-plane and in-line kernel directions.

5.2.4 Primary Energy Fluence Extraction

Primary energy fluence (PEF) was obtained by multiplying the primary fluence by an empirically determined mean energy photon distribution, characteristic of the Varian Clinac 23EX. The mean photon energy distribution was sampled from the CAX mean photon energy and off-axis mean photon energy correction. The CAX mean photon energy was determined from the total linear attenuation coefficient and its exponential relationship with intensity, resulting from an absorber (Eq. 5.5). As shown in Figure 5–3, the intensity reduction was measured under narrow beam geometry² conditions to minimize scattering from the Solid Water attenuator, and the IC-10 ionization chamber was set a reasonable distance away from the Solid Water to minimize the number of scattered photons reaching the detector. Furthermore, a buildup cap was placed on the IC-10 to create a charged particle equilibrium state for accurate charge accumulation in air.

² *Narrow beam geometry technique implies a narrowly collimated source of monoenergetic photons.*

$$I^{\theta=0} = I_0^{\theta=0} \cdot \exp(-\mu(\theta = 0) \cdot z), \quad (5.5)$$

where $I^{\theta=0}$ is the attenuated intensity, $I_0^{\theta=0}$ is the incident intensity with no absorber, $\mu(\theta = 0)$ is the CAX total linear attenuation coefficient, and z is the Solid Water thickness.

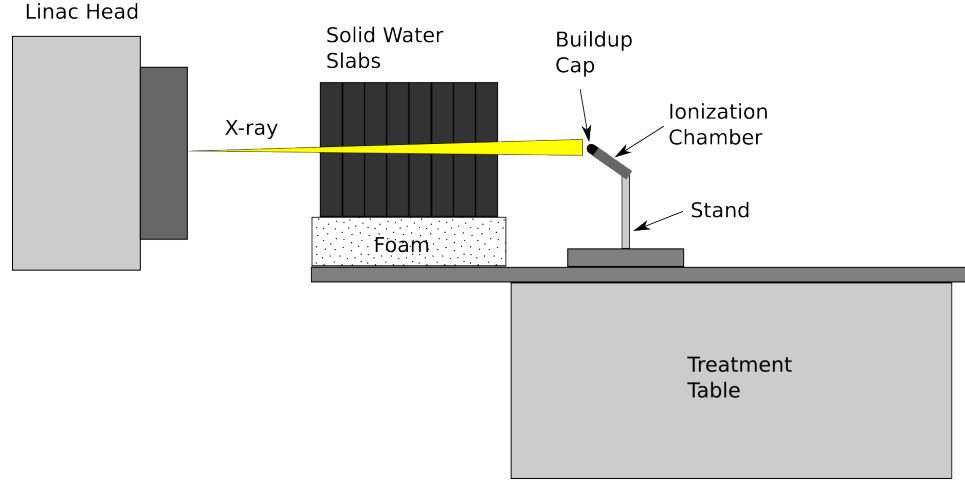


Figure 5-3: Narrow beam geometry measurement setup used for the determination of the total linear attenuation coefficient.

The CAX mean photon energy could thus be determined from the total linear attenuation coefficient and the prior knowledge of the attenuator material as water³. Therefore, by searching the National Institute of Standards and Technology (NIST) photon cross section database (XCOM) [6] a connection between the total attenuation coefficient in water and the CAX mean photon energy was made. The off-axis total linear attenuation coefficient correction was described by the CAX total linear attenuation coefficient $\mu(\theta = 0)$ and the off-axis total linear attenuation

³ *Solid Water is capable of mimicking the radiation absorption characteristics of water to within 1% [3].*

5.3. RESULTS

coefficient $\mu(\theta)$ [8], as expressed in Equation 5.6, where θ is the angle in degrees from the CAX photon ray.

$$\frac{\mu(\theta)}{\mu(\theta = 0)} = 1 + 0.00181\theta + 0.00202\theta^2 - 0.0000942\theta^3, \quad (5.6)$$

The off-axis mean photon energy was sampled from the correction factor $s(\theta)$ in Equation 5.7 and multiplied by the CAX mean photon energy $E(\theta = 0)$ in Equation 5.8 [8, 2].

$$s(\theta) = \left(\frac{\mu(\theta = 0)}{\mu(\theta)} \right)^{2.22}, \quad (5.7)$$

$$E(\theta) = s(\theta) \cdot E(\theta = 0), \quad (5.8)$$

The mean photon energy distribution matrix was calculated with Equation 5.8, assuming a point source in spherical coordinates and radially mapped on to a matrix with equivalent detector area of $40 \times 30 \text{ cm}^2$.

The following equation summarizes the extraction of the PEF Ψ :

$$\Psi(x, y) = \left\{ (PI_{corr}(x, y) \cdot BP(x, y)) \otimes^{-1} (k_g(x, y) \otimes k_d(x, y)) \right\} \cdot E(x, y), \quad (5.9)$$

where PI_{corr} is the raw portal image, BP is the beam profile correction, k_d is the dose kernel, k_g is the glare kernel, and E is the mean photon energy distribution.

5.3 Results

5.3.1 Image Corrections

As shown in Figure 5–4 (a), the PD exhibited lines and regions of defective regions shown in white. The FF (Fig. 5–4 (b)) demonstrated the strongest sensitivity in the central region of the active detector surface, while the corners seemed to represent the least sensitive response. The DF (Fig. 5–4 (c)), resembled

5.3. RESULTS

vertical light and dark stripes, while the *NI* (Fig. 5–4 (d)) displayed small random light and dark “pixelation”.

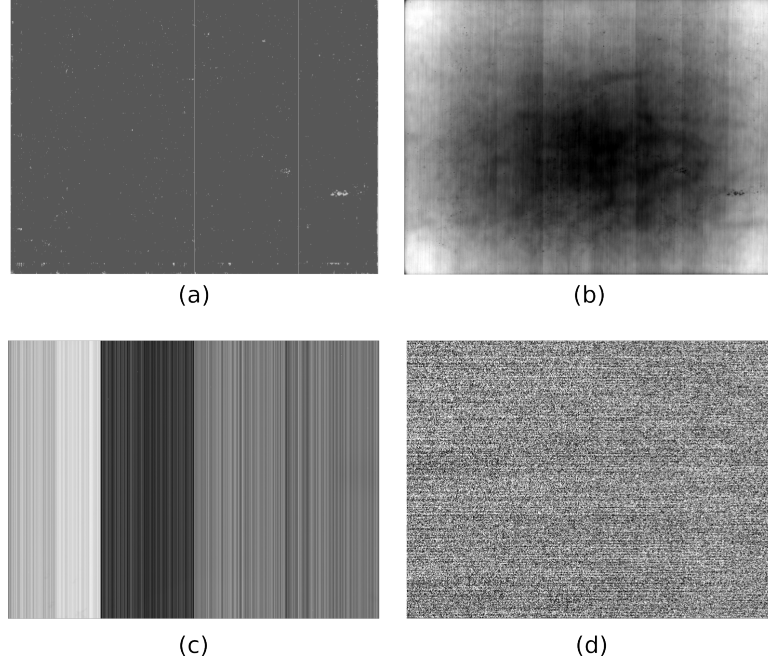


Figure 5–4: Calibration images: (a) pixel defect map, (b) flood field, (c) dark field, and (d) noise image.

5.3.2 Beam Profile Correction

The IC-10 beam profile measurement of a 6 MV, 40×40 cm² field profile at a depth of 8.0 mm (Fig. 5–5) in water was normalized to the CAX, and resulted in a weighting increase of up to 6% at 15.0 cm from the CAX. Furthermore, as shown in Figure 5–5 (b) the weighting increased with distance from CAX, in a non-linear fashion.

As show in Figure 5–6, the raw EPID 6 MV, 10×10 cm² field demonstrated a considerable deviation in the plateau region of the profile as compared to the beam profile corrected EPID image. The raw EPID profile exhibited up to a 3% discrepancy at the CAX. Also shown in Figure 5–6, the corrected EPID image profile (Fig. 5–6) manifested the beam profile horn characteristic.

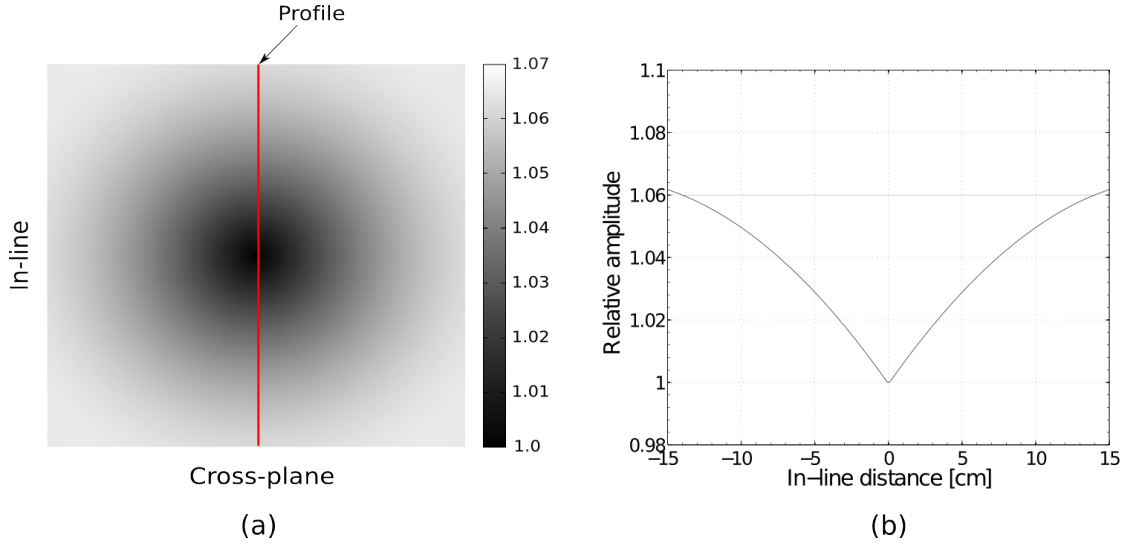


Figure 5-5: Beam profile correction matrix originating from a radially mapped 6 MV, $40 \times 40 \text{ cm}^2$ field profile measured at a depth of 8.0 mm in water: (a) two-dimensional beam profile correction weighting, and (b) an in-line profile measured along the central axis of (a) (red).

5.3.3 Glare and Dose Kernels

The dose kernel shown in Figure 5-7 was calculated by DOSXYZnrc from a $0.01 \times 0.01 \text{ cm}^2$, 1.8 MeV monoenergetic photon beamlet and scored at the bottom of the scintillation screen within the EPID. The global electron cut-off energy (ECUT) and photon cut-off energy (PCUT) was 0.521 MeV, and 0.01 MeV, respectively. The dose kernel was smoothed with a moving-average filter with a span of 10 to remove statistical fluctuations and discontinuities. Span is defined as $2N + 1$, where N is the number of neighboring pixels to be averaged surrounding the smoothed data value. Overall, the dose kernel followed a steep exponential decay, with a wider spatial extent beginning at approximately $\pm 0.5 \text{ cm}$ from the center of the beamlet. At $\pm 5 \text{ cm}$ the dose kernel amplitude was 9×10^{-7} .

The Richardson-Lucy iteratively optimized glare kernel was within convergence tolerance after 5,576 iterations and 8,119 function evaluations. The minimum function value derived from Equation 5.3, was determined to be 0.34. During the

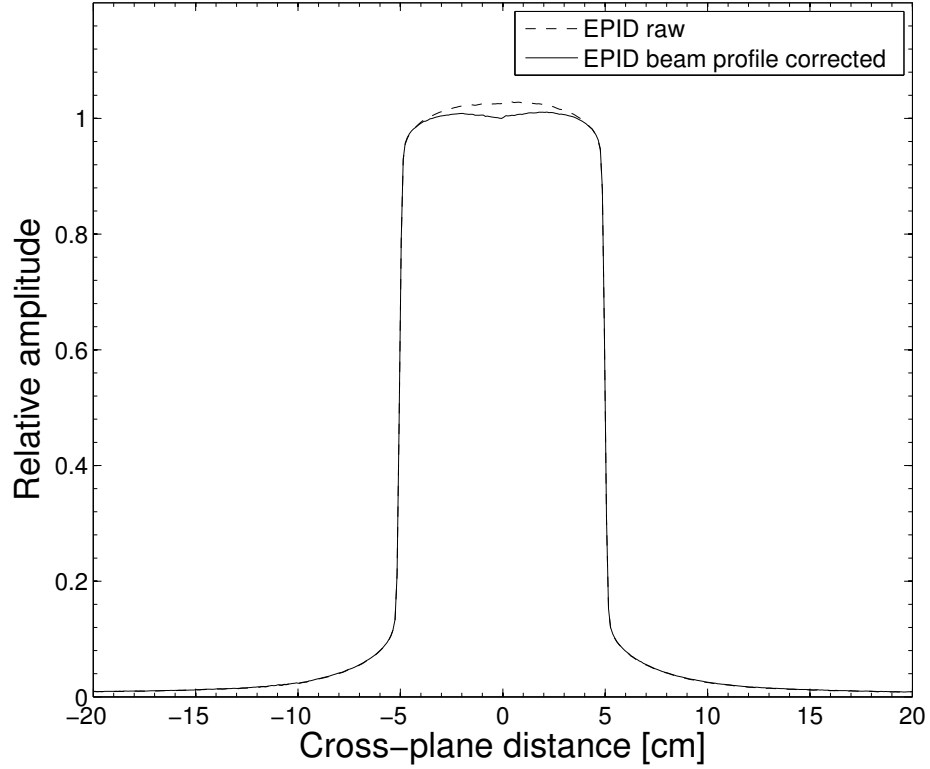


Figure 5–6: A comparison between a raw (dotted) and beam profile corrected (solid) 6 MV, 10×10 cm² EPID cross-plane profile.

search for convergence, each function evaluation represented one iteration of the DECONVLUCY MATLAB function. It was determined that any DECONVLUCY iteration value above one, resulted in a minimum value of Equation 5.3 that was considerably higher, therefore one iteration was chosen for each function evaluation of the FMINSEARCH MATLAB function used to optimize the nine parameters of Equation 5.2 to minimize Equation 5.3.

As illustrated in Figure 5–7, the glare kernel exhibited a much different spatial extent than the dose kernel. The glare kernel had a shallower decay radially from the center of the beamlet. For instance, at ± 1.0 cm the glare kernel was a thousand times greater in relative amplitude as compared to the dose kernel. Another intriguing characteristic of the glare kernel was the abrupt decay rate

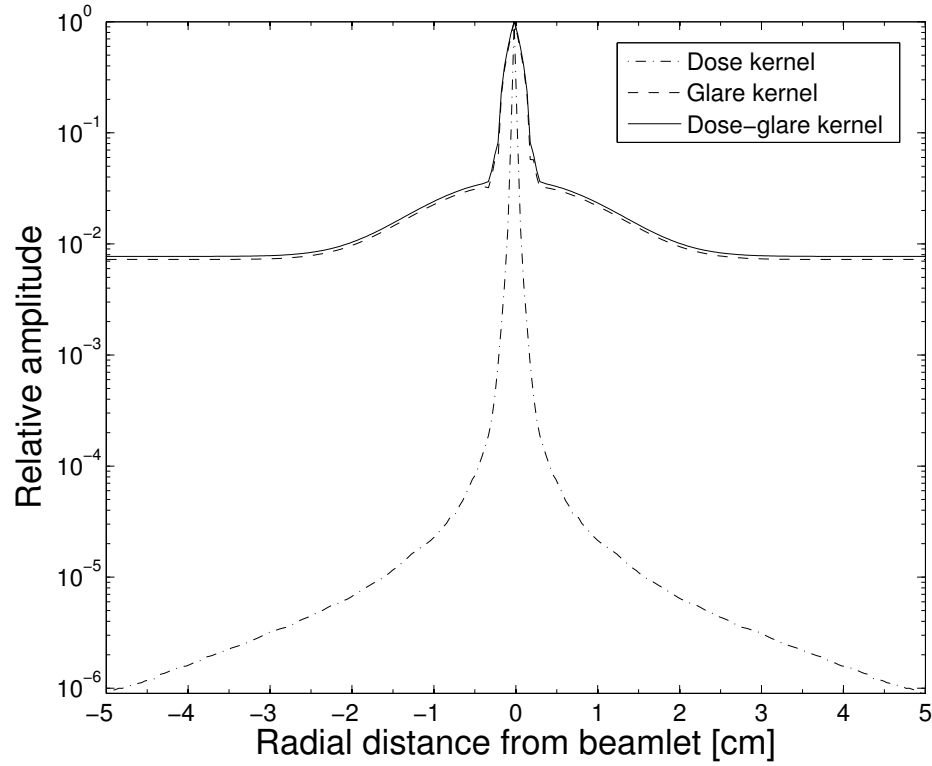


Figure 5-7: The cross-plane kernels used for the EPID deconvolution: the MC generated dose kernel scored in the scintillation screen, the iteratively optimized glare kernel, and the combined dose-glare scatter kernel.

change at ± 0.3 cm from the center of the beamlet. Less than ± 0.3 cm there existed a steep fall-off, however after ± 0.3 cm a slowly decaying Gaussian tail developed. The relative amplitude was flat above ± 2.5 cm from the center of the beamlet. Overall, the glare kernel represented the dominant correction of the dose-glare scatter kernel.

As a result from the described 1D kernel to 2D dose-glare kernel conversion (Fig. 5-2), there exists four 90 degree projections from the center of the dose-glare kernel, illustrated in Figure 5-8. Although their amplitude was approximately 0.7% of the maximum amplitude, this cross-pattern shaped projections were found to significantly contribute to the correction in the penumbra region of the raw EPID image. The importance of these projections was discovered by attempting to

5.3. RESULTS

deconvolve an EPID image without the presence of the projections, this resulted in poor agreement of EPID primary fluence as compared to the IC-10 beam profile.

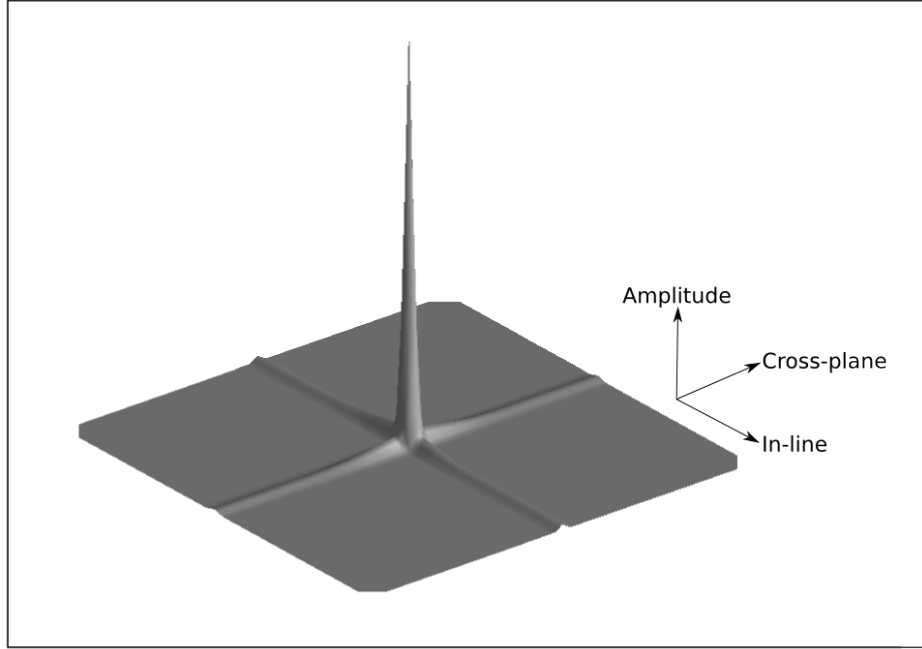


Figure 5-8: Three-dimensional dose-glare scatter kernel.

5.3.4 EPID Depth Dose

To analyze the relative dose at depth along the CAX of the DOSXYZnrc EPID phantom, a depth dose was acquired from the three-dimensional relative dose volume of the dose kernel MC calculation. As shown in Figure 5-9, the depth dose steeply increased at starting of the copper layer, and peaked at the copper-scintillation screen interface. Then, the dose gradually decreased within the scintillation screen, silicon, glass, and foam. At the silicon layer (or photodiode array) the dose was 50% of the max dose. There was another buildup beginning at the foam-water interface that increased to 27% of the max dose before the beam exited the EPID model.

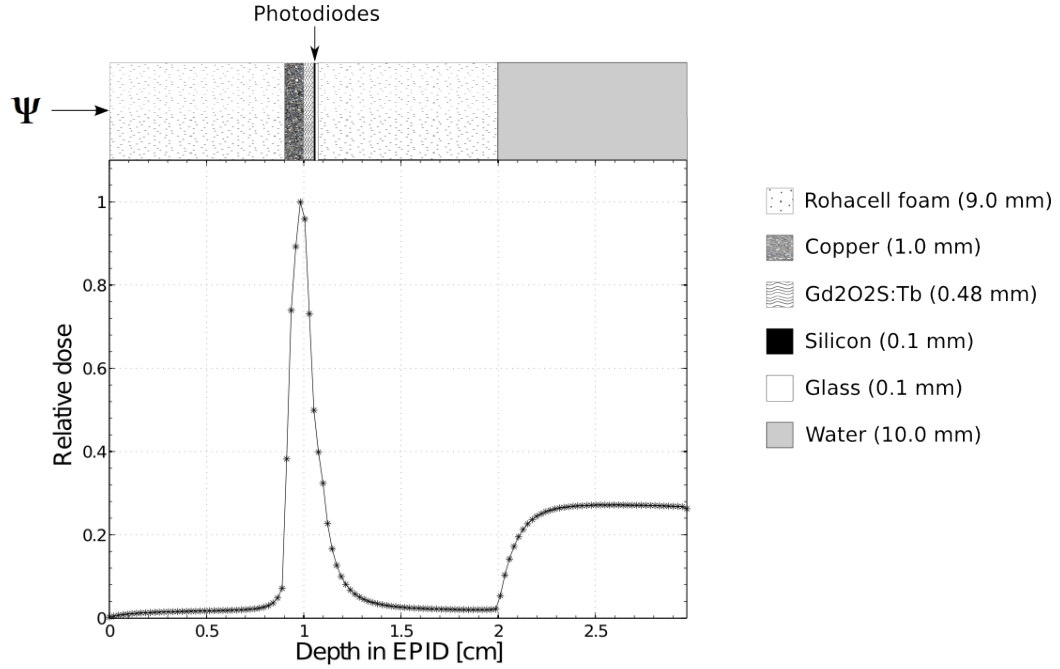


Figure 5-9: Monte Carlo depth dose curve scored in each PortalVision aS1000 EPID layer where, ψ indicates orientation of incident primary energy fluence directed at the EPID model.

5.3.5 Measured and Optimized EPID In-Air Fluence Beam Profiles

The in-air IC-10 beam profile measurement shown in Figure 5-10, had evidence of beam horns and had a flatter beam profile plateau than the EPID raw profile. Moreover, the penumbra and umbra regions of the IC-10 beam profile were also sharper as compared to the EPID raw profile. In particular, the beginning of the umbra region for the IC-10 profile was 27% that of the raw EPID profile. Interestingly, the IC-10 profile featured an abrupt relative amplitude rate of decrease at the beginning of the umbra. Volume averaging was apparent in the penumbra region of the IC-10 profile, while the EPID raw did not have this effect. The optimized in-air fluence profile (EPID-corrected) and the IC-10 profile were in best agreement along the umbra region and ± 2.5 cm from CAX. The EPID-corrected profile horns were 2% higher than the IC-10 profile. The penumbra

was also steeper for the EPID-corrected than both the EPID-raw and the IC-10 profiles.

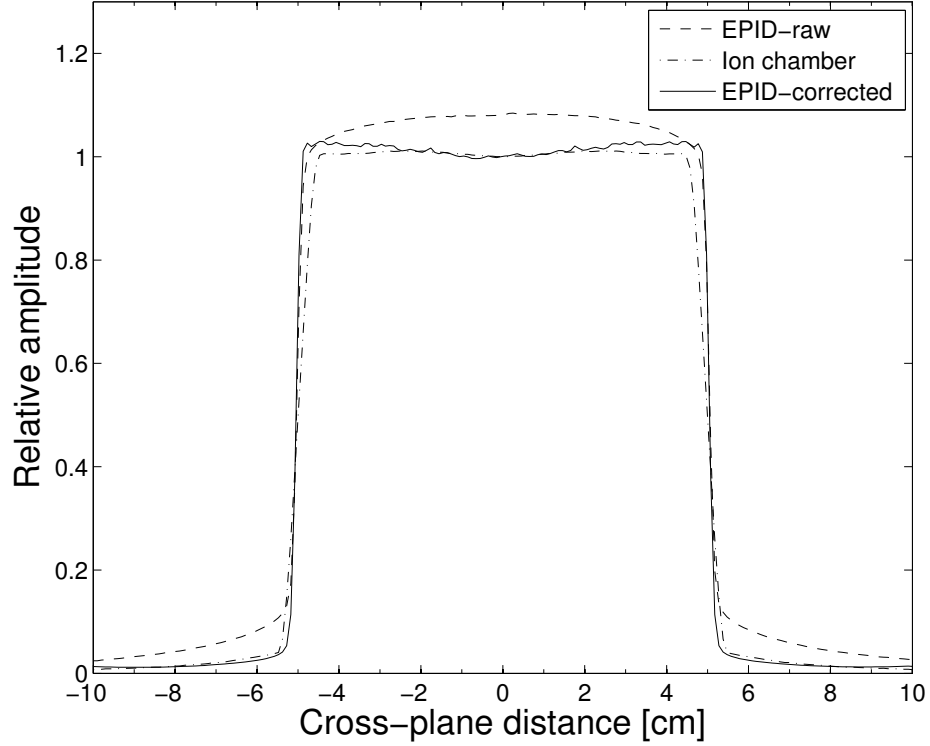


Figure 5-10: Cross-plane profiles for a 6 MV, 10×10 cm² in-air field taken with the raw EPID, the IC-10 ionization chamber, and the iteratively optimized (primary fluence) EPID corrected image.

5.3.6 Primary Energy Fluence

The narrow beam geometry measurement (Fig. 5-3) resulted in a total linear attenuation coefficient of 0.0452 cm^{-1} , derived from the fit Equation 5.5 as shown in Figure 5-11. According to the measured total attenuation coefficient, the corresponding CAX mean photon energy from the NIST XCOM database in water was determined to be 2.3 MeV. Derived from Equation 5.8, the mean photon energy distribution shown in Figure 5-12, ranged from 2.3 MeV at CAX to 2.0 MeV at -20 cm (cross-plane).

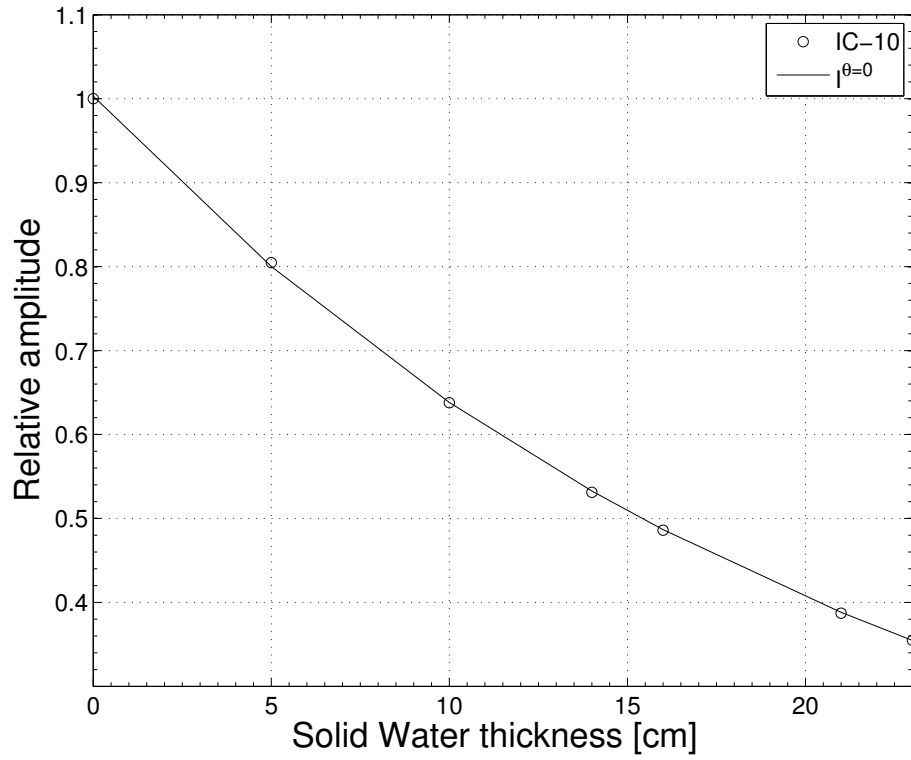


Figure 5-11: Ionization chamber (IC-10) attenuation measurement with increasing Solid Water attenuator thickness, where $I^{\theta=0}$ is the attenuated intensity.

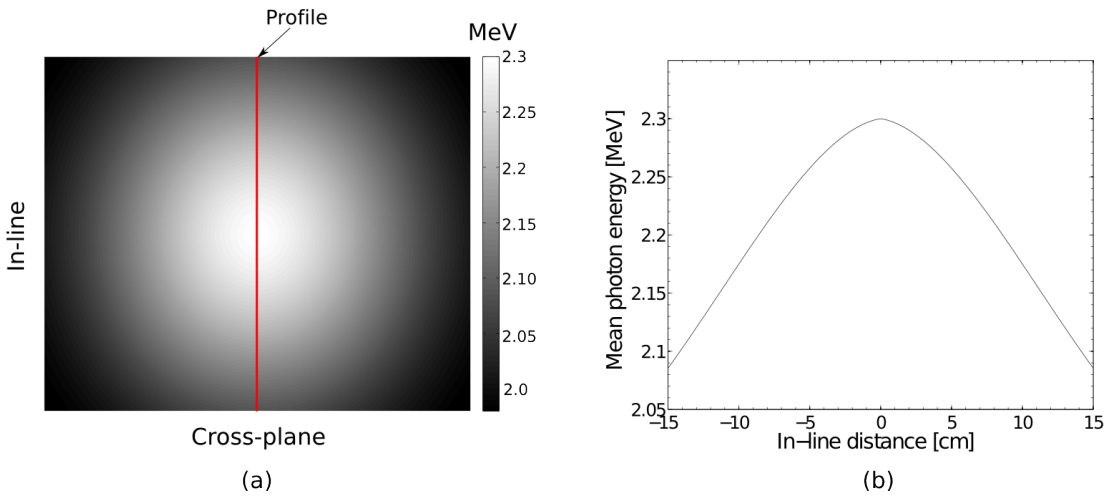


Figure 5-12: Mean photon energy distribution: (a) mean photon energy matrix in MeV, and (b) an in-line profile along central axis of (a) (red).

A summary of the calibration process to arrive at PEF from a raw EPID image, is illustrated in Figure 5–13. The extracted primary fluence ψ had a circular weighting in the center of the square field, and a steep fall-off in the penumbra region.

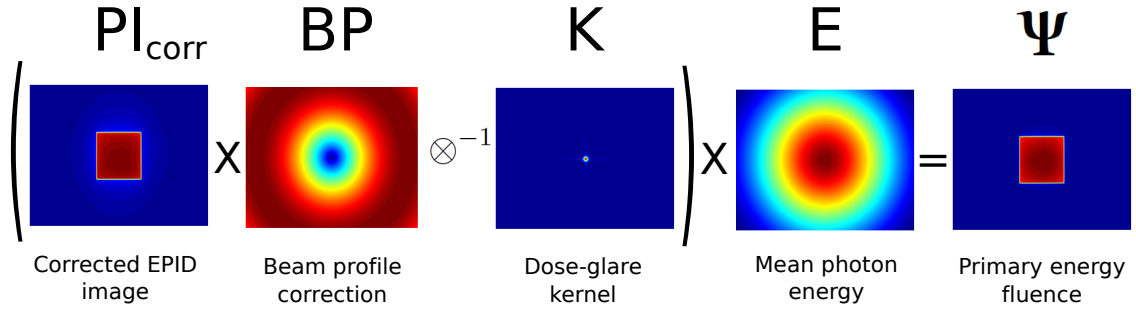


Figure 5–13: A summary of the calibration process to extract the primary energy fluence from a PortalVision aS1000 EPID 6 MV, $10 \times 10 \text{ cm}^2$ image.

5.4 Discussion and Conclusion

The image corrections represented an important initial step for extracting PEF from the EPID. Each calibration image manifested the imperfections present in the EPID. Without the *PD*, *FF*, *DF*, and *NI*, portal dosimetry wouldn't be possible, since they remove defective pixels, adjust pixel sensitivities, and remove electrometer offsets all leading up to over a 40% overall correction.

The beam profile correction was necessary to allow for the incorporation of the flattening filter effect, which creates a flat beam profile plateau at depth. Since, the *FF* removed the beam horns, it became imperative that this dosimetric characteristic be restored for accurate portal dosimetry. Based on the IC-10 beam profile measurement, the horns increased over 6% as compared to the CAX. By multiplying the beam profile matrix by the raw EPID image, the beam horn characteristics were successfully restored.

Due to x-ray scattering in the copper and scintillation screen, as well as optical photon divergence (or glare) between the scintillation screen and the photodiode

5.4. DISCUSSION AND CONCLUSION

array, spatial degradation was present in each EPID image. This degradation was especially apparent in the penumbra and umbra beam profile regions. To measure incident primary photon fluence, spatial degradation needed to be removed. As described previously in Section 5.2.3, a two part scatter kernel (dose and glare) was deconvolved with each EPID image to derive the primary photon fluence. The MC calculated dose kernel represented a minor correction as compared to the iteratively optimized glare kernel. The uniquely shaped glare kernel (i.e. cross patten projections and steep top wide base) may have physical significance or it could resemble non-physical attributes relating to the iteration number for the DECONVLUCY algorithm utilized for optimization and deconvolution. In terms of physical understanding, the glare kernel theoretically should have less spatial extent correction as compared to the dose kernel because the optical photon energies are much lower as compared to the photon and electron energies that make up the dose kernel extent. As for the cross projections, they result mathematically from the process of factorizing the kernel (Fig. 5-2). Before the factorizing method was employed, an attempt to radially map the scatter kernel resulted in severe over deconvolution and was eventually abandoned for the factorization method, which yielded excellent results. Interestingly, without the projections the correction in the umbra region was poor. It is possible these projections are related to the process of reading out the integrated charge along data lines. The steep fall-off 0.5 cm away from the beamlet center represented the optical photon divergence within the amorphous scintillation screen, while the broad decrease from 0.5 cm to 2.0 cm, may have resulted from non-optical photons such as lower energy x-rays and electrons that traversed the scintillation screen. Finally, it should be noted there was elliptical symmetry to the overall scatter kernel because it was observed that the profile along the in-line direction required a slightly broader scatter kernel correction due to the stronger spatial degradation.

5.4. DISCUSSION AND CONCLUSION

Since, the scintillation screen is amorphous (random directional dependance), the elliptical symmetry must be associated with the photodiode array and readout symmetry.

The MC depth dose scored along the CAX of the EPID clearly demonstrated the copper buildup effect. The rather steep dose drop beyond the copper plate and within the scintillation screen, indicated the conversion of electrons and photons into optical photons captured by the photodiode. Moreover, there was a change of slope at the scintillation screen photodiode interface, thus provided more evidence for optical photon creation.

The in-air IC-10 profile provided a reasonable measure of the primary fluence, however since the chamber has a finite volume, the volume averaging effect was apparent in the penumbra regions. To avoid optimizing the primary fluence to a volume averaged fluence, a theoretical profile based on the measured IC-10 profile was used instead. This profile was identical to the IC-10 profile, but without the volume averaging present in the steep regions of the primary fluence. As a result, the derived primary fluence profile represented, the primary incident photon fluence at an SDD of 100 cm. An interesting characteristic of the primary fluence was the abrupt amplitude change at the field edge due to collimator scatter, and leakage through collimator jaws and machine head housing.

The empirically determined mean photon energy distribution revealed that with increased distance from CAX there is a decrease of mean photon energy. This off-axis reduction has been previously studied by Taylor et al. [8] empirically, and was primarily due to selective attenuation by the flattening filter. Since the flattening filter is thicker along the central ray, there is beam hardening (less low energy photons), while photon rays along the thinner regions of the flattening filter encompass a broader spectrum of low energy photons. The CAX mean photon energy of 2.3 MeV on the CAX was expected since, the radiotherapy beam was 6 MV, and

5.4. DISCUSSION AND CONCLUSION

based on the bremsstrahlung photon spectrum the monoenergetic representation commonly is one-third the potential difference (i.e. $6/3=2.0$ MeV). Overall, the mean photon energy distribution presented a more significant correction for photon rays further off-axis. It is also worth noting, the mean photon energy distribution determined empirically was in disagreement with BEAMnrc simulation of the Varian Clinac 23EX. The CAX mean photon energy was found to be 1.8 MeV rather than 2.3 MeV as determined by the empirical method. Moreover, the energy fall-off was much steeper in the BEAMnrc mean photon energy distribution (1.24 MeV at 15 cm) as compared to the empirical mean energy distribution (2.09 MeV at 15 cm). This result may be caused by an incorrect linac model or misuse of the energy distribution data from the BEAMnrc phase-space file. In either case, PDD measurements in Chapter 6 will support the decision to use the empirically determined mean photon energy distribution over the BEAMnrc simulation.

Extraction of PEF required many different steps, however with the proper scatter kernel, the deconvolution based approach requires less measurement than other empirically driven scatter kernel methods [9]. The method for PEF extraction in this research project, could also be easily adapted for other EPID models, and result in an accurate generalized calibration scheme for routine use.

References

- [1] 2000. IAS3 Reference Guide (P/N B401994R01E), Varian Medical Systems Inc.
- [2] M. Fippel, F. Haryanto, O. Dohm, F. Nusslin, and S. Kriesen. A virtual photon energy fluence model for monte carlo dose calculation. *Med. Phys.*, 30:301–311, 2003.
- [3] Gammex. Gammex- <http://www.gammex.com/>.
- [4] C. Rafael C. Gonzalez, Richard E. Woods, and Steven L. Eddins. *Digital Image Processing using MATLAB*. Gatesmark, second edition, 2009.
- [5] L. Ko, J. Kim, and J. Siebers. Investigation of the optimal backscatter for an asi epid. *Phys. Med. Biol.*, 49:1723–1738, 2004.
- [6] NIST. NIST XCOM - <http://www.nist.gov/>.
- [7] J. Siebers, J. Kim, L. Ko, P. Keall, and R. Mohan. Monte carlo computation of dosimetric amorphous silicon electronic portal images. *Med. Phys.*, 31:2135–2146, 2004.
- [8] R. Tailor, V. Tello, C. Schroy, and M. Vossler. A generic off-axis energy correction for linac photon beam dosimetry. *Med. Phys.*, 25:662–667, 1998.
- [9] W. van Elmpt, S. Nijsten, R. Schiffeleers, A. Dekker, B. Mijnheer, P. Lambin, and A. Minken. A monte carlo based three-dimensional dose reconstruction method derived from portal dose images. *Med. Phys.*, 33:2426–2434, 2006.

CHAPTER 6 **THREE-DIMENSIONAL DOSE RECONSTRUCTION USING** **PRIMARY ENERGY FLUENCE AND MONTE CARLO** **SIMULATION**

Contents

6.1	Introduction	94
6.2	Materials and Methods	95
6.2.1	Generation of Phase Space File	95
6.2.2	DOSXYZnrc Simulation and Dose Normalization . . .	97
6.3	Results	98
6.3.1	EPID Reconstructed Beam Profiles	98
6.3.2	EPID Reconstructed Percent Depth Doses	98
6.3.3	2D Dose Distribution Comparison	98
6.4	Discussion and Conclusion	102

6.1 Introduction

Monte Carlo calculation utilizing DOSXYZnrc was implemented in order to convert the 2D primary energy fluence extracted from the EPID to a 3D reconstructed dose. As mentioned in Section 2.4, DOSXYZnrc requires a source input for dose calculation in rectilinear voxel defined phantoms. In this study, the primary energy fluence (PEF) was sampled to create a phase space distribution compatible with DOSXYZnrc as a source input. Several 3D dose volumes were simulated including: 5×5 and 10×10 cm² open-fields, 60° enhanced dynamic wedge (EDW). Results were compared to film and PDIODE photodiode measurements in Solid Water and water, respectively.

6.2 Materials and Methods

6.2.1 Generation of Phase Space File

The binary phase-space file (PSF) contains information related to each particle sampled from the PEF and was written using MATLAB 7.8.0. The PSF begins with a header consisting of the following data [1]:

1. `MODE_RW` - is the file mode: it can be either 'MODE0' or 'MODE2' depending on whether ZLAST is included in the phase-space parameters.
2. `NPPHSP` - is the total number of particles in the file.
3. `NPHOTPHSP` - is the total number of photons in the file.
4. `EKMAXPHSP` - is the maximum kinetic energy of the particles stored in the file.
5. `EKMINPHSP` - is the minimum electron kinetic energy (MeV).
6. `NINCPHSP` - is the number of particles incident from the original (non-phase space) source used to generate the PSF.

In this study, the `MODE_RW` was set to "0" since, there was no ZLAST or z-position of the last interaction of photons. Both the `NPPHSP` and `NPHOTPHSP` were equated because only photons were considered in this research project. According to the mean photon energy distribution, the `EKMASPHSP` and `EKMINPHSP` were set to 2.3 MeV and 0 MeV, respectively. The `NINCPHSP` was arbitrarily defined as 10^8 , due to the fact that the number of particles originating from the source were unknown.

After the header, each particle sampled from the PEF was associated with the following parameter:

1. `LATCH` - 32 bit variable for tracking particle history and represents the particle charge.
2. `E` - is the particle total energy (kinetic and rest mass, single precision).
3. `X` - is the particle X-position (cm).

4. Y - is the particle Y-position (cm).
5. U - is the X-direction cosine.
6. V - is the Y-direction cosine.
7. WT - is the particle's weight; WT also carries the sign of W, the Z-direction cosine.

To avoid any geometry conflict between the PSF and phantom, the PEF was back-projected to a plane 30 cm above isocenter and was assumed that the photons originated from a point source. Every particle was assigned a LATCH of "0" to maintain the existence of only photons. The sampling of each particle was done randomly within the bounds of the field specified by the user. Once a random position was determined, the mean photon energy distribution was called to produce the energy at the same position. Both the U and V were calculated from the random position as follows:

$$U = \frac{X}{\sqrt{X^2 + Y^2 + S2PHSP^2}}, \quad (6.1)$$

$$V = \frac{Y}{\sqrt{X^2 + Y^2 + S2PHSP^2}}, \quad (6.2)$$

where the S2PHSP is the distance between the source and the center of the phase-space plane (70 cm).

For verification dose distribution, the PEFs consisted of 20 million photons bound to the field size plus 2.0 cm. The PSFs were 560 MB and took approximately 5 hours to complete when using a 2.4 GHz Intel Core 2 Duo Processor¹ with 4 GB of RAM.

¹ Intel Corp., Santa Clara, CA, USA. Intel Core 2 Duo Processor is a registered trademark of Intel Corp.

6.2.2 DOSXYZnrc Simulation and Dose Normalization

For Monte Carlo 3D dose calculation, DOSXYZnrc utilized the PSF sampled from the PEF as a source (ISOIRC = 2). The verification phantoms were defined as a non-CT input and assigned water as the material. Phantoms had an X and Y resolution of 0.3125 cm/voxel and a Z resolution of 0.5 cm/voxel. To improve statistical uncertainty, 10^9 particle histories were simulated with ECUT and PCUT set to 0.521 MeV and 0.01 MeV, respectively. The surrounding medium was defined as a vacuum and the phase space particles were allowed to recycle based on DOSXYZnrc automatic calculation. Monte Carlo simulations were conducted on McGill University's computer cluster. Jobs were run in parallel and distributed amongst 18 central processing units (CPUs). The common job time duration was approximately 2.5 hours per field.

The following dose normalization procedure was implemented in order to calibrate the MC calculated 3D dose distributions to absolute dose². The dose normalization was accomplished by simulating a 6 MV radiotherapy beam under the calibration conditions³ for the Varian Clinac 23EX. The resulting voxel at the calibration point D_{cal} , where the linac was calibrated to produce 1 cGy/1 MU, was extracted from the 3D MC simulated dose distribution in water. Each 3D dose simulated was normalized to D_{cal} as expressed in Equation 6.3.

$$D_{x,y,z}^{abs} = U \cdot \frac{D_{x,y,z} [dose/particle]}{D_{cal} [dose/particle]} \cdot \frac{1cGy}{1MU}, \quad (6.3)$$

² In this thesis, the term "absolute dose" as it is commonly understood in a clinical environment, namely for dose determination in units of Gy according to a dosimetry protocol.

³ Calibration conditions: SAD setup, 10×10 cm² field size, 1.5 cm depth in water.

6.3. RESULTS

where U is the number of MU, $D_{x,y,z}^{abs}$ is the absolute dose, $D_{x,y,z}$ is the [dose/particle] from the raw MC 3D dose distribution.

6.3 Results

6.3.1 EPID Reconstructed Beam Profiles

As shown in Figure 6–1, the EPID reconstructed 5×5 , 10×10 , and 20×20 cm² at 5.0, 10.0, and 15.0 cm depth in water were mainly within 2% agreement with PDIODE measurement. MC statistical fluctuation was present in all profiles, especially noticeable in the plateau region. Generally, the statistical fluctuation decreased with depth in water. The EPID reconstructed profile penumbra and umbra regions were in excellent agreement with PDIODE measurement.

6.3.2 EPID Reconstructed Percent Depth Doses

The EPID reconstructed PDDs for each field size (5×5 , 10×10 , 20×20 cm²) were primarily within 2% of PDIODE measurement. Both the 5×5 and 10×10 cm² PDDs indicated better agreement beyond d_{max} ⁴, however the EPID reconstructed PDD discrepancy slowly increased above 10.0 cm depth in water. Overall, the 20×20 cm² PDD had the best agreement with PDIODE measurement along the entire range of depth in water.

6.3.3 2D Dose Distribution Comparison

The EPID reconstructed 10×10 cm² open-field 2D dose distribution measured at 5.0 cm depth in Solid Water exhibited statistical fluctuation and therefore the circular pattern present in the EDR2 film measurement was difficult to observe (Fig. 6–3).

According to Figure 6–4, the absolute dose difference for the EPID reconstructed 6 MV, 10×10 cm² open-field primarily ranged from 1.5% to 2.5%. The

⁴ d_{max} is defined as the depth of dose maximum in water.

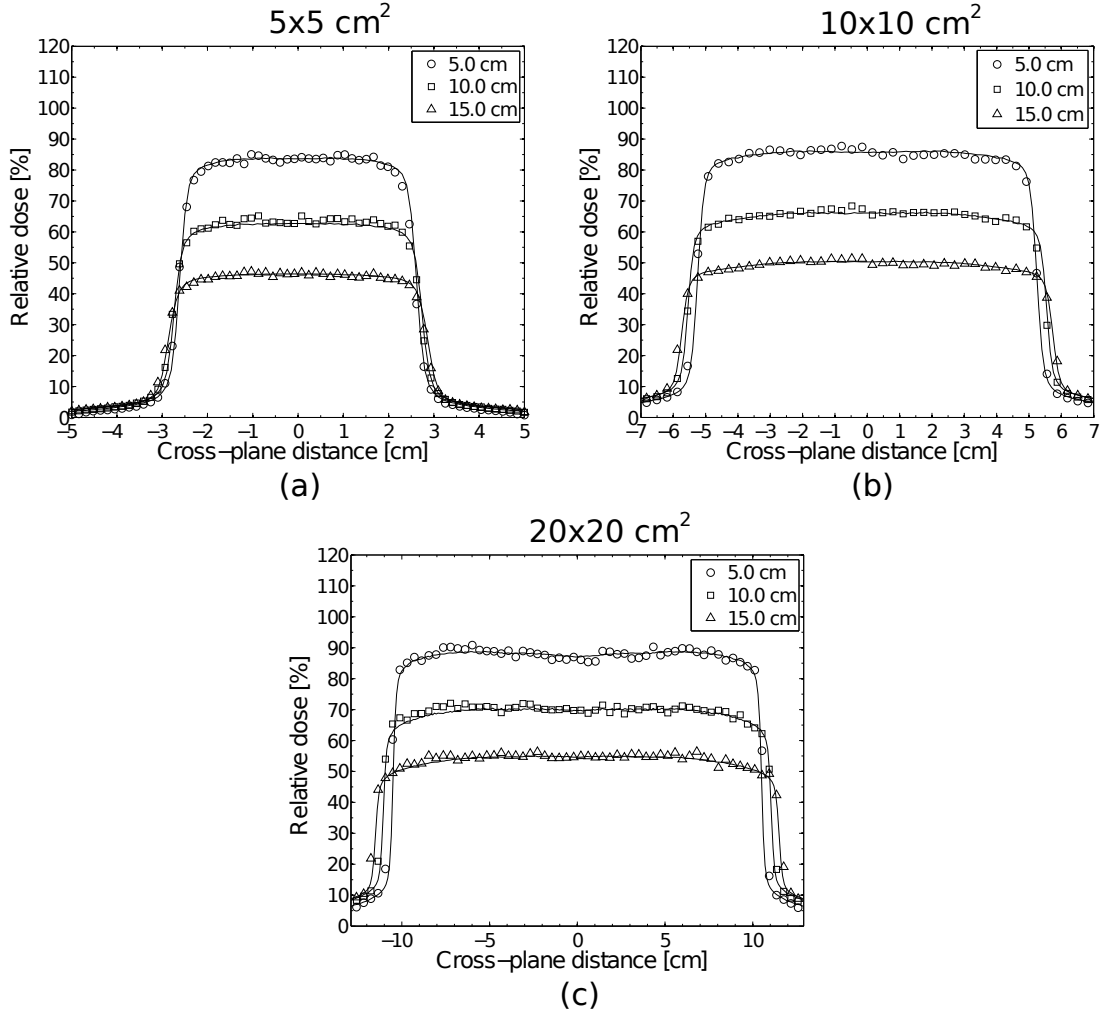


Figure 6-1: EPID reconstructed open-field cross-plane beam profiles at depths of 5.0, 10.0, and 15.0 cm in water as compared to PDIODE measurement: (a) 5×5 cm^2 , (b) 10×10 cm^2 , and (c) 20×20 cm^2 .

greatest discrepancy of approximately 10% was observed in the upper-right corner along the penumbra region.

As indicated by Figure 6-5, the γ indexes inside the field boundary for the DTA criterion of 3.0 mm and dose-difference criterion of 3% were between 0 and 1, while the majority of the failing points lied along the penumbra region in the in-line direction and across the top region of the 2D dose distribution.

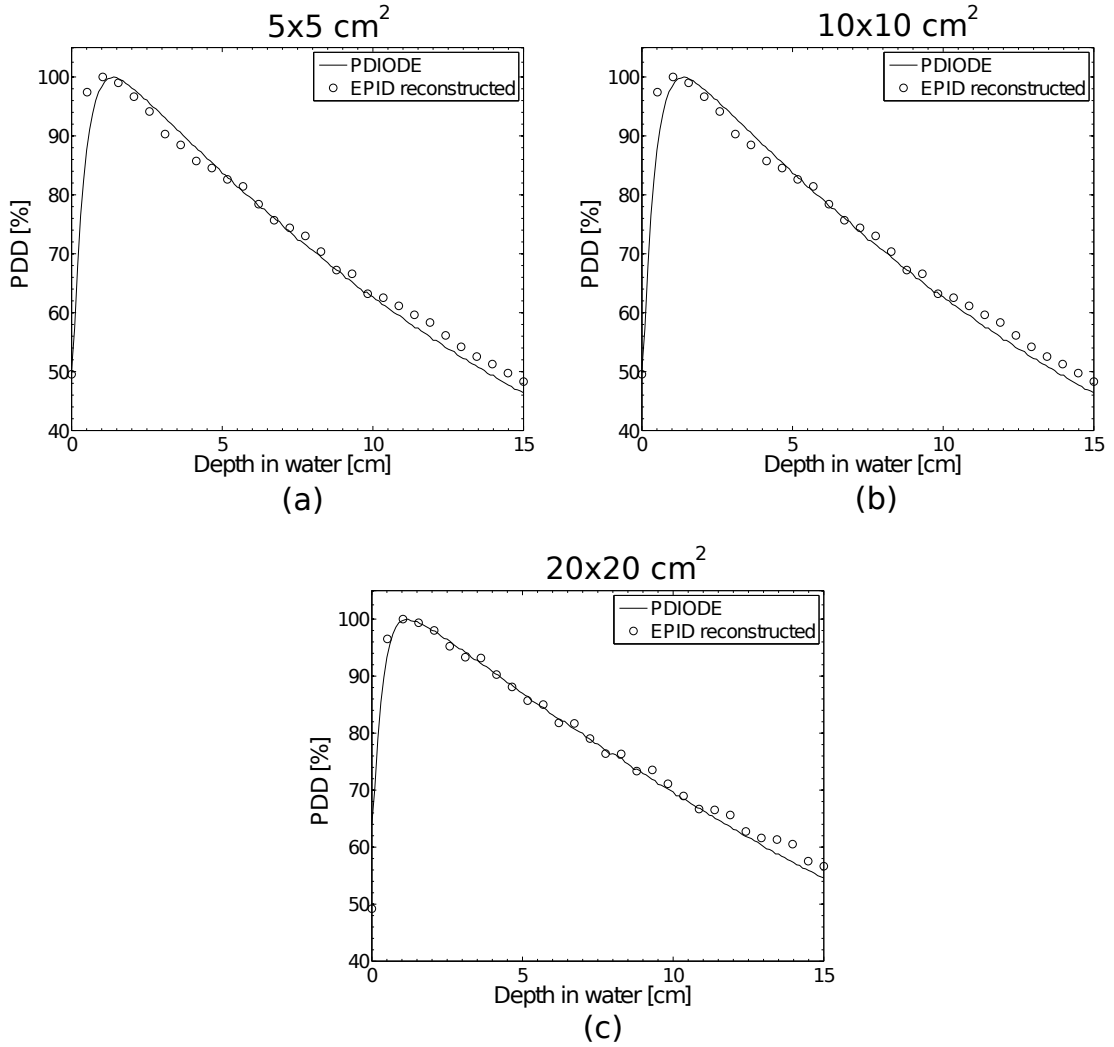


Figure 6-2: EPID reconstructed PDDs as compared to PDIODE measurement in water: (a) $5 \times 5 \text{ cm}^2$, (b) $10 \times 10 \text{ cm}^2$, and (c) $20 \times 20 \text{ cm}^2$.

The EPID reconstructed 60° EDW exhibited a larger high dose region as compared to the EDR2 film (Fig. 6-6). Beyond the high dose region the EPID reconstructed dose gradient showed less discrepancy.

As shown in Figure 6-7, the absolute dose difference was most frequently within 1%. The upper high dose region showed the greatest discrepancy inside the 60° EDW 2D dose distribution of approximately 5%. The best agreement was in the middle and lower dose portion of the dose gradient with absolute dose differences of approximately 1%.

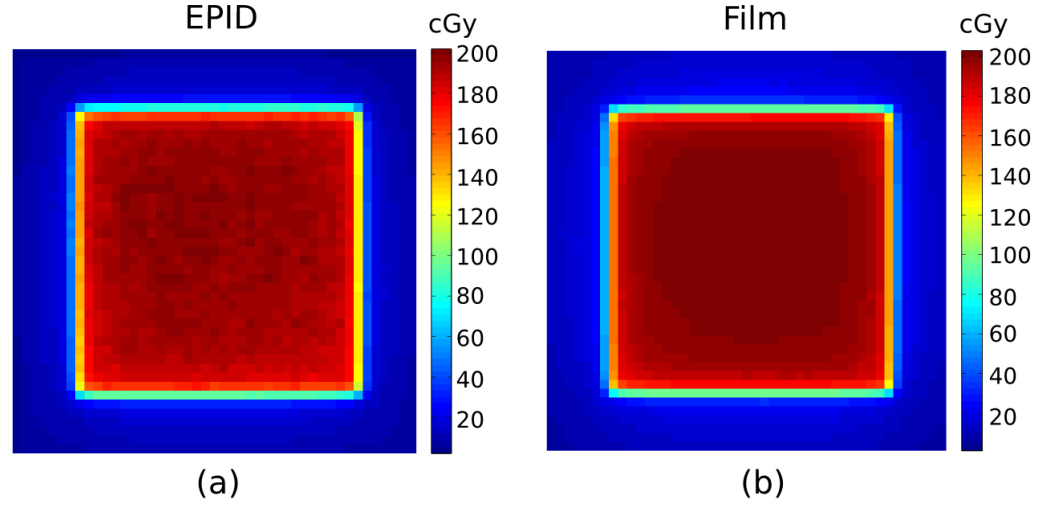


Figure 6-3: A 6 MV, 10×10 cm² open-field 2D dose distributions obtained at 5.0 cm depth in water (Solid Water for film): (a) EPID reconstructed, and (b) EDR2 radiographic film.

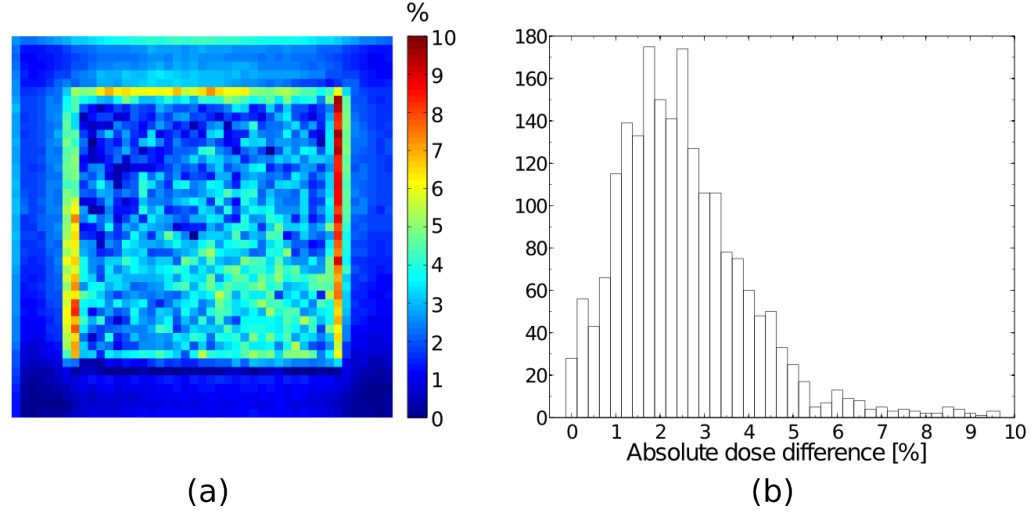


Figure 6-4: Absolute dose difference between EDR2 radiographic film and EPID reconstruction normalized to max film dose for a 6 MV, 10×10 cm² open-field 2D dose distribution obtained at 5.0 cm depth in water (Solid Water for film): (a) absolute dose distribution (cGy), and (b) histogram of (a).

The γ evaluation (3%, 3.0 mm) of the 60° EDW demonstrated strong criterion acceptance within the field with all points passing significantly below 1 (Fig. 6-8). The majority of the fail point locations were in the penumbra region.

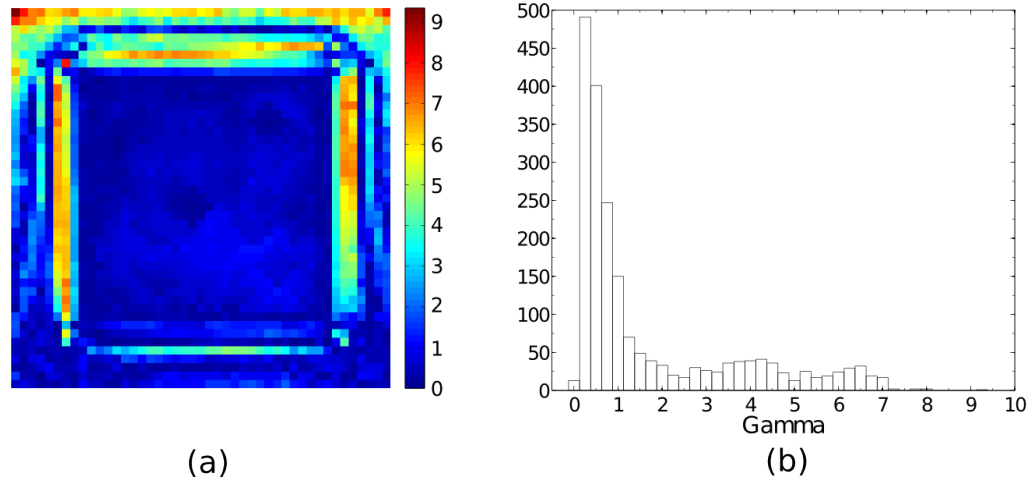


Figure 6-5: γ evaluation between EDR2 radiographic film and EPID reconstruction for a 6 MV, 10×10 cm² open-field 2D dose distribution obtained at 5.0 cm depth in water (Solid Water for film): (a) γ distribution, and (b) histogram of (a).

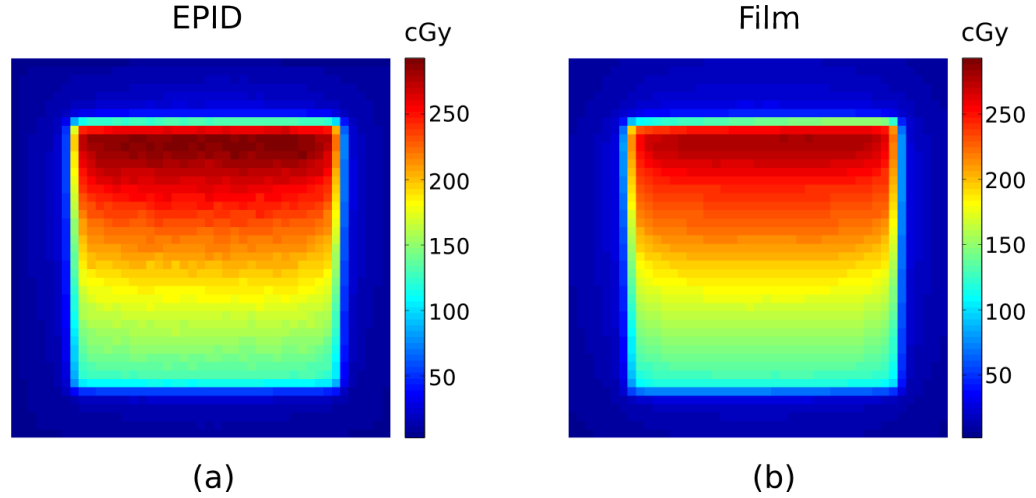


Figure 6-6: A 6 MV, 10×10 cm² 60° enhanced dynamic wedge 2D dose distributions obtained at 5.0 cm depth in water (Solid Water for film): (a) EPID reconstructed, and (b) EDR2 radiographic film.

6.4 Discussion and Conclusion

The EPID reconstructed beam profiles were in excellent agreement with PDIODE measurement. The statistical fluctuations present in the plateau regions could be overcome by sampling more particles from the PEF. This would provide lesser uncertainty for DOSXYZnrc MC calculation and smoother beam profiles.

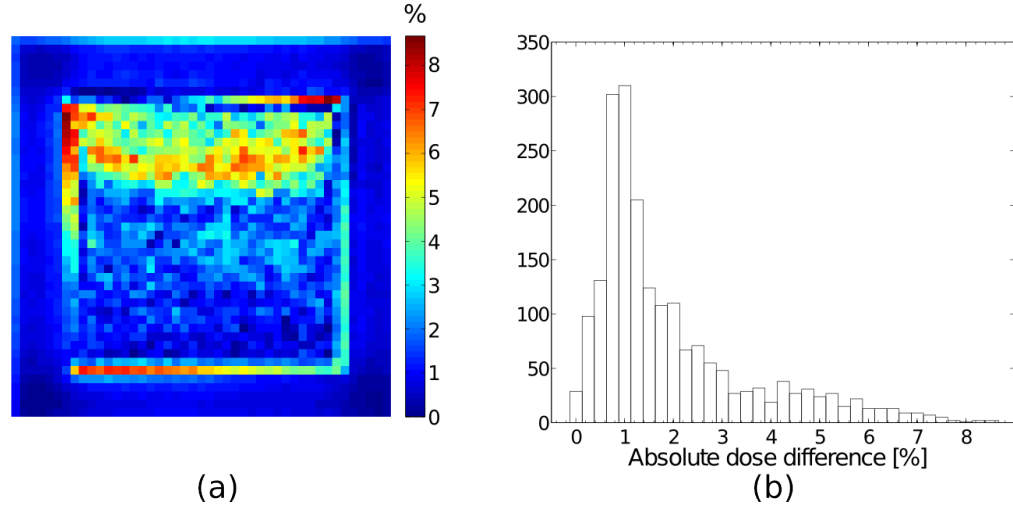


Figure 6-7: Absolute dose difference between EDR2 radiographic film and EPID reconstruction normalized to max film dose for a 6 MV, $10 \times 10 \text{ cm}^2$ 60° enhanced dynamic wedge 2D dose distribution obtained at 5.0 cm depth in water (Solid Water for film): (a) absolute dose distribution (cGy), and (b) histogram of (a).

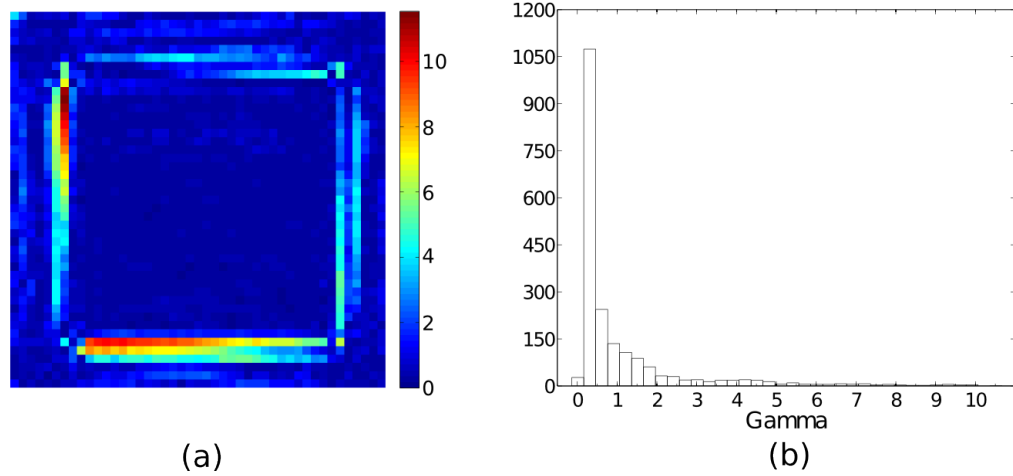


Figure 6-8: γ evaluation between EDR2 radiographic film and EPID reconstruction for a 6 MV, $10 \times 10 \text{ cm}^2$ 60° enhanced dynamic wedge 2D dose distribution obtained at 5.0 cm depth in water (Solid Water for film): (a) γ distribution, and (b) histogram of (a).

As for the reduction in fluctuation at 20.0 cm, this effect was likely due to the fact that more particle histories were simulated as compared to shallower depths that rely more heavily on incident fluence.

The EPID reconstructed PDD buildup regions were expected to disagree with the PDIODE measurements due to volume averaging and the inherent buildup present in the PDIODE. Since, the majority of clinical target volumes are beyond d_{max} the EPID reconstructed PDDs are sufficiently accurate.

Based on the film dosimetry results the adopted calibration protocol produced accurate 2D dose distributions comparable to MC simulated dose distributions. Under optimal conditions the EDR2 film should be within $\pm 2\%$ and based on the 2D dose distributions the majority of dose points inside the two different fields agreed to within 2%. The γ evaluation indicated the majority of points passing inside the field boundaries, suggesting sufficient dose and spatial accuracy required for more complicated distributions like IMRT.

Overall, the verification measurements for the reconstructed EPID dose distributions provided strong evidence for successful dose reconstruction from the PEF extracted from the EPID.

References

- [1] I. Kawrakov and D. Rogers, 2003. EGSnrc / BEAMnrc / DOSXYZnrc. EGS electron gamma source. Pirs, NRCC - Canada Ottawa - National Research Council.

CHAPTER 7 FINAL CONCLUSIONS

Contents

7.1	Dissertation Summary	106
7.2	Future Work	107

7.1 Dissertation Summary

The main objective of this research project was to develop a convolution and Monte Carlo based non-transmission portal dosimetry method used to reconstruct a 3D dose distribution. The method first required an understanding of the Varian PortalVision aS1000 EPID dosimetric performance and suitability for portal dosimetry. A dosimetric evaluation of the PortalVision aS1000 indicated the EPID response was linear with MU and had a 0.2% standard deviation short-term reproducibility. The pixel uniformity was within 3% inside radiotherapy field boundaries and the EPID exhibited a 2% decreased response with increased dose-rate. The displacement was determined to be sub-millimeter for angles ranging from 0 to 360° and also had field size dependence different from dose to water. Furthermore, there was evidence of image lag and the memory effect, however only under extreme clinical conditions. Overall, the PortalVision aS1000 EPID demonstrated excellent dosimetric performance with fast acquisition and high resolution images.

To overcome the x-ray scatter and optical divergence, a scatter kernel was determined for deconvolution of the EPID images for primary energy fluence (PEF) extraction from the PortalVision aS1000. The scatter kernel consisted of two parts: a Monte Carlo (MC) simulated dose kernel scored at the bottom of the scintillation

screen in the EPID model, and a empirically initialized iterative deconvolution optimization optical spreading (“or glare”) kernel. The iterative deconvolution optimization procedure implemented in MATLAB 7.8.0 successfully produced a scatter kernel that had a dominating glare kernel correction as compared to the dose kernel. The deconvolution of a 10×10 cm² field EPID image with the derived scatter kernel, successfully reproduced a similar, but sharper in-air primary fluence as compared to ionization chamber (IC-10) measurement.

To reconstruct a 3D dose from the previously determined PEF, a phase-space file (PSF) generation program, implemented in MATLAB 7.8.0, was written to randomly sample photons from the extracted EPID PEF and acted as an source input for DOSXYZnrc MC simulation in a rectilinear voxel phantom. The resulting 3D dose distributions were verified against measured beam profiles, PDDs, and EDR2 radiographic film 2D dose distributions. The verification measurements indicated strong agreement with EPID reconstructed 3D dose distributions, with most of the measurements within 2% agreement, and passing γ evaluation.

This project successfully reconstructed a 3D dose distribution from the extracted PEF measured by a Varian PortalVision aS1000 EPID. The convolution and MC based method indicated robust performance and was successfully verified by dosimetric measurement.

7.2 Future Work

This study demonstrates the potential for pretreatment IMRT verification from an EPID reconstructed 3D dose distribution in a patients planning CT-scan. Pretreatment for other advanced radiotherapies such as VMAT, IMAT, or RapidArc poses a significant advantage over currently employed procedures, since a 3D dose distribution corresponding to a patient’s actual anatomical features will offer a more clinically relevant, and accurate detailed analysis of calculated vs. actual radiotherapy delivery. In order to pursue RapidArc pretreatment

7.2. FUTURE WORK

verifications, the PortalVision aS1000 continuous imaging mode will need to be explored, since time-resolved dose verification will play an important role in complex dynamic deliveries.

For this method to become routine, other future work will include verification measurements for other radiotherapy photon beam energies (i.e. 10 MV, 18 MV, etc.) and a new source model for DOSXYZnrc in order to exploit the efficiency of dynamic libraries to avoid the inefficiencies of writing a phase-space file. To implement this EPID 3D dose reconstruction method for stereotactic radiotherapy, smaller field sizes as well as better defined geometric accuracy will need to be evaluated in more detail.

ABBREVIATIONS

1D	One-dimension
2D	Two-dimension
3D	Three-dimension
3D-CRT	Three-Dimension Conformal Radiotherapy
AAPM	American Association of Physicists in Medicine
AE	Restrictive stopping power
AP	Collisional restrictive stopping power
ASCII	American Standard Code for Information Interchange
a-Si	Amorphous silicon
CAX	Central axis
CCD	Charge-coupled device
cGy	Centigray
CH	Condensed history
CL	Confidence level
CM	Component module
CPU	Central processing unit
CT	Computed Tomography
CTV	Clinical target volume
DC	Direct current
DF	Dark field
DI	Drift image
dmax	Depth of maximum dose
DMLC-IMRT	Dynamic Intensity Modulated Radiation Therapy

DNA	Deoxyribonucleic acid
DPI	Dots per square inch
DTA	Distance-to-agreement
DU	Digitization unit
EBT	External beam radiotherapy
ECUT	Electron cut-off energy
EDR2	Extended dose range
EDW	Enhanced dynamic wedge
EGS	Electron Gamma Shower
ENIAC	Electronic Numerical Integrator and Computer
EPID	Electronic portal imaging device
ETRAN	Electron transport
FCT	Frame cycle time
FF	Flood field
FLUKA	Fluktuierende Kaskade
FPB	Frame processing board
fps	Frames per second
FWHM	Full-width half-max
GB	Gigabyte
GEANT4	Geometry and Tracking
GHz	Gigahertz
GTV	Gross tumor volume
Gy	Gray
IAS3	Image acquisition system
IC-10	Ionization chamber
ICRU	International Commission on Radiation Units and Measurements

IDU	Image detection unit
IEC	International Electrotechnical Commission
IMAT	Intensity Modulated Arc Therapy
IMRT	Intensity Modulated Radiation Therapy
ISL	Inverse square law
kV	Kilovolt
LINAC	Linear accelerator
MB	Megabyte
MC	Monte Carlo
MCNP	Monte Carlo N-particle-extended
MeV	Megaelectron volt
MHz	Megahertz
MLC	Multileaf collimator
MRI	Magnetic Resonance Imaging
MU	Monitor Unit
MV	Megavolt
NI	Noise image
NRC	Nuclear Research Council of Canada
NTCP	Normal tissue complication probability
PCUT	Photon cut-off energy
PD	Pixel defect map
PDD	Percent depth dose
PDF	Percent density function
PEF	Primary energy fluence
PENELOPE	Penetration and Energy Loss of Position and Electron
PSF	Phase space file

PTV	Planning target volume
RAM	Random access memory
RF	Radio-frequency
RNG	Random number generator
ROI	Region of interest
SAD	Source-to-axis distance
SD	Standard deviation
SDD	Source-to-detector distance
SEER	Surveillance Epidemiology and End Results
SLAC	Stanford Linear Accelerator Center
SLIC	Scanning liquid filled ionization chamber
SMLC-IMRT	Segmental Intensity Modulate Radiation Therapy
SSD	Source-to-surface distance
TCP	Tumor control probability
TFT	Thin film transistor
TPS	Treatment planning system
UCB	Universal control board
UTCP	Uncomplicated tissue control probability
VMAT	Volumetric modulated arc therapy

REFERENCES

- [1] 2000. IAS3 Reference Guide (P/N B401994R01E), Varian Medical Systems Inc.
- [2] D. Bonnett A. Glendinning. Dosimetric properties of the theraview fluoroscopic electronic portal imaging device. *Br. J. Radiol.*, 73:517–30, 2000.
- [3] P. Andreo. Monte carlo techniques in medical radiation physics. *Phys. Med. Biol.*, 36:861–920, 1991.
- [4] L. Antonuk. Electronic portal imaging devices: a review and historical perspective of contemporary technologies and research. *Phys. Med. Bio.*, 47:R31–R65, 2002.
- [5] L. Antonuk, J. Boudry, J. Yorkston, C. F. Wild, M. J. Longo, and R. A. Street. Radiation damage studies of amorphous silicon photodiode sensors for applications in radiotherapy x-ray imaging. *Nucl. Instrum. Methods*, 299:143–6, 1990b.
- [6] Berger and Seltzer, 1968. ETRAN - electron transport. Technical report, National Institute of Standards and Technology.
- [7] J. Berger. Monte carlo calculation of the penetration and diffusion of fast charged particles. *Methods in Computational Physics*, 1:135–215, 1963.
- [8] T. Bogucki, W. Murphy, C. Baker, S. Piazza, and A. Haus. Processor quality control in laser imaging systems. *Med. Phys.*, 24:581–84, 1997.
- [9] J. Boudry and L. Antonuk. Radiation damage of amorphous silicon photodiode sensors. *IEEE Trans. Nucl. Sci.*, 47:703–7, 1994.
- [10] A. Brahme, J. Chavaudra, T. Landberg, E. McCullough, F. Nusslin, A. Rawlinson, G. Svensson, and H. Svensson. Accuracy requirements and quality assurance of external beam therapy with photons and electrons. *Acta. Oncol.*, 27:Suppl. 1, 1998.
- [11] J. F. Briesmeister, 2000. MCNP - a general Monte Carlo N-particle transport code version 4C. Technical Report LA-12625-M, Los Alamos Natl. Lab.
- [12] Karl K. Bush. *Monte Carlo Dose Calculations in Advanced Radiotherapy*. 2009.

- [13] L. L. Carter and E. D. Cashwell. *Particle-Transport Simulation with the Monte Carlo Method, TID-26607*. National Technical Information Service, U. S. Department of Commerce, 1975.
- [14] CERN, 1982. GEANT - GEometry AND TRacking. Technical report, CERN - European Organization for Nuclear Research.
- [15] Sun Nuclear Corp. MapCHECK- <http://www.sunnuclear.com/>.
- [16] M. Dirkx and B. Heijmen. Testing of the stability of intensity modulated beams generated with dynamic multileaf collimation, applied to the mm50 racetrack microtron. *Med. Phys.*, 27:2701–7, 2000.
- [17] M. Dirkx, M. Kroonwijk, J. de Boer, and B. Heijmen. Daily dosimetric quality control of the mm50 racetrack microtron using an electronic portal imaging device. *Radiother. Oncol.*, 37:55–60, 1995.
- [18] A. Djouguela, R. Kollhoff, A. Ruhmann, K. Willborn, D. Harder, and B. Poppe. Physical mechanism of the schwarzschild effect in film dosimetry-theoretical model and comparison with experiments. *Phys. Med. Biol.*, 51:4345–4356, 2006.
- [19] A. Dutreix. When and how can we improve precision in radiotherapy? *Radiother. Oncol.*, 2:275–292, 1984.
- [20] Y. El-Mohri, L. Antonuk, J. Yorkston, K. Jee, M. Maolinbay, K. Lam, and J. Siewerdsen. Dose-response and ghosting effects of an amorphous silicon electronic portal imaging device. *Med. Phys.*, 26:1530–1541, 1999.
- [21] Z. Elbalaa, J. Foulquier, A. Orthuon, H. Elbalaa, and E. Touboul. Role of the frame cycle time in portal dose imaging using an as500-ii epid. *Physica Medica*, 25:148–153, 2009.
- [22] M. Fippel, F. Haryanto, O. Dohm, F. Nusslin, and S. Kriesen. A virtual photon energy fluence model for monte carlo dose calculation. *Med. Phys.*, 30:301–311, 2003.
- [23] Centers for Disease Control and Prevention (CDC), 2006. Fact sheet.
- [24] R. L. Ford and W. R. Nelson, 1978. The EGS Code System: Computer Programs for the Monte Carlo Simulation of Electromagnetic Cascade Showers (Version 3) Rep. SLAC-210.
- [25] E. Franken, J. de Boer, J. Barnhoorn, and B. Heijmen. Characteristics relevant to portal dosimetry of a cooled ccd camera-based epid. *Med. Phys.*, 31:2549–51, 2004.
- [26] Gammex. Gammex- <http://www.gammex.com/>.

- [27] Eric J. Hall & Amato J. Giaccia. *Radiobiology for the Radiologist*. Lippincott Williams & Wilkins, sixth edition, 2006.
- [28] C. Rafael C. Gonzalez, Richard E. Woods, and Steven L. Eddins. *Digital Image Processing using MATLAB*. Gatesmark, second edition, 2009.
- [29] B. Heijmen, K. Pasma, and M. Kroonwijk. Portal dose measurement in radiotherapy using an electronic portal imaging device (epid). *Phys. Med. Biol.*, 40:1943–55, 1995.
- [30] IBA. IBA - <http://www.iba-dosimetry.com/>.
- [31] ICRU. Prescribing, recording, and reporting photon beam therapy. *International Commission on Radiation Units and Measurements*, 50, 1993.
- [32] INFN and CERN, 1982. FLUKA - (FLUktuierende KAskade). Technical report, Italian National Institute for Nuclear Physics (INFN) and by the European Organization for Nuclear Research (CERN).
- [33] A. Kavuma, M. Glegg, G. Currie, and A. Elliott. Assessment of dosimetrical performance in 11 varian a-si500 electronic portal imaging devices. *Phys. Med. Biol.*, 53:6893–6909, 2008.
- [34] I. Kawrakov and D. Rogers, 2003. EGSnrc / BEAMnrc / DOSXYZnrc. The EGSnrc code system : Monte Carlo simulation of electron and photon transport. Pirs-701, NRCC - Canada Ottawa - National Research Council.
- [35] I. Kawrakov and D. Rogers, 2003. EGSnrc / BEAMnrc / DOSXYZnrc. EGS electron gamma source. Pirs, NRCC - Canada Ottawa - National Research Council.
- [36] L. Ko, J. Kim, and J. Siebers. Investigation of the optimal backscatter for an asi epid. *Phys. Med. Biol.*, 49:1723–1738, 2004.
- [37] R. Louwe, L. McDermott, J. Sonke, R. Tielenburg, M. Wendling, M. van Herk, and B. Mijnheer. The long-term stability of amorphous silicon flat panel imaging devices for dosimetry purposes. *Med. Phys.*, 31:2989–2995, 2004.
- [38] D. Low and J. Dempsey. Evaluation of the gamma dose distribution comparison method. *Med. Phys.*, 30:2455–2464, 2003.
- [39] D. Low, W. Harms, S. Mutic, and J. Purdy. A technique for the quantitative evaluation of dose distributions. *Med. Phys.*, 25:656–661, 1998.
- [40] L. McDermott, R. Louwe, J. Sonke, M. van Herk, and B. Mijnheer. Dose-response and ghosting effects of an amorphous silicon electronic portal imaging device. *Med. Phys.*, 31:285–295, 2004.

- [41] L. McDermott, S. Nijsten, J. Sonke, M. Partridge, M. van Herk, and B. Minheer. Comparison of ghosting effects for three commercial a-si epids. *Med. Phys.*, 33:2448–2451, 2006.
- [42] H. Meertens, M. van Herk, J. Bijhold, and H. Bartelink. First clinical experience with a newly developed electronic portal imaging device. *Int. J. Rad. Oncol. Biol. Phys.*, 18:1173–81, 1990.
- [43] H. Meertens, M. van Herk, and J. Weeda. A liquid ionisation detector for digital radiography of therapeutic megavoltage photon beams. *Phys. Med. Bio.*, 30:313–21, 1985.
- [44] P. Muench, A. Meigooni, R. Nath, and W. McLaughlin. Photon energy dependence of the sensitivity of radiochromic film and comparison with silver halide and lif tlds used for brachytherapy dosimetry. *Med. Phys.*, 18:767–775, 1991.
- [45] Metropolis N. The beginning of the monte carlo method. *Los Alamos Science*, Special Issue:125–130, 1987.
- [46] Walter R. Nelson, Hideo Hirayama, and David W. O. Rogers, 1985. The EGS4 Code System, Stanford Linear Accelerator Center.
- [47] NIST. NIST XCOM - <http://www.nist.gov/>.
- [48] International Commission on Radiation Units and Measurements (ICRU). ICRU Report 24. Determination of absorbed dose in a patient irradiated by beams of x or gamma rays in radiotherapy procedures. (*Washington, D.C.: ICRU*), 1976.
- [49] K. Otto. Volumetric modulated arc therapy: Imrt in a single gantry arc. *Med. Phys.*, 35:310–7, 2008.
- [50] M. Overdick, T. Solf, and H. Wischmann. Temporal artefacts in flat dynamic x-ray detectors. *Proc. SPIE*, 4320:47–54, 2001.
- [51] S. Pai, I. Das, J. Dempsey, K. Lam, T. Losasso, A. Olch, J. Palta, L. Reinstein, D. Ritt, and E. Wilcox. Tg-69: Radiographic film for megavoltage beam dosimetry. *Med. Phys.*, 34:2228–2258, 2007.
- [52] Å. Palm, A. Kirov, and T. LoSasso. Predicting energy response of radiographic film in a 6 mv x-ray beam using monte carlo calculated fluence spectra and absorbed dose. *Med. Phys.*, 31:3168–3178, 2004.
- [53] G. Pang, L. Lee, and J. Rowlands. Investigation of a direct conversion flatpanel imager for portal imaging. *Med. Phys.*, 28:2121–2128, 2001.

- [54] M. Partridge, B. Hesse, and L. Müller. A performance comparison of direct- and indirect-detection flat-panel imagers. *Nucl. Instrum. Methods Phys. Res.*, A484:351–363, 2002.
- [55] K. Pasma, M. Kroonwijk, J. de Boer, A. Visser, and B. Heijmen. Accurate portal dose measurement with a fluoroscopic electronic portal imaging device (epid) for open and wedged beams and dynamic multileaf collimation. *Phys. Med. Biol.*, 43:2047–60, 1998.
- [56] Ervin B. Podgorsak. *Radiation Physics for Medical Physicists*. Springer, first edition, 2006.
- [57] A. Sawant, H. Zeman, S. Samant, G. Lovhoiden, B. Weinberg, and F. DiBianca. Theoretical analysis and experimental evaluation of a csi(tl) based electronic portal imaging system. *Med. Phys.*, 29:1042–53, 2002.
- [58] Y. A. Shreider. *The Monte Carlo Method*. Pergamon Press, 1966.
- [59] J. Siebers, J. Kim, L. Ko, P. Keall, and R. Mohan. Monte carlo computation of dosimetric amorphous silicon electronic portal images. *Med. Phys.*, 31:2135–2146, 2004.
- [60] J. Siewerdsen and D. Jaffray. A ghost story: spatio-temporal response characteristics of an indirect-detection flat-panel imager. *Med. Phys.*, 26:1624–1641, 1999.
- [61] E. Spezi, D. Lewis, and C. Smith. A dicom-rt-based toolbox for the evaluation and verification of radiotherapy plans. *Phys. Med. Biol.*, 47:4223–4232, 2002.
- [62] S. Srivastava and I. Das. Dose rate dependence of film dosimetry in radiation treatment: Study of reciprocity law. *Med. Phys.*, 33:2089 (abstract), 2006.
- [63] Varian Medical Systems, 2000. PortalVision aS500 Rel. 6, Reference Manual, Version 6.0.05.
- [64] R. Tailor, V. Tello, C. Schroy, and M. Vossler. A generic off-axis energy correction for linac photon beam dosimetry. *Med. Phys.*, 25:662–667, 1998.
- [65] J. Thebaut and S. Zavgorodni. Coordinate transformations for beam/egsnrc monte carlo dose calculations of non-coplanar fields received from a dicom-compliant treatment planning system. *Phys. Med. Biol.*, 51:N441–9, 2006.
- [66] UB, 1982. PENELOPPE - PENetration and energy LOss of Positron and Electron. Technical report, Universitat de Barcelona.
- [67] W. van Elmpt, L. McDermott, S. Nijsten, M. Wendling, P. Lambina, and B. Mijnheera. A literature review of electronic portal imaging for radiotherapy dosimetry. *Radiother. Onc.*, 88:289–309, 2008.

- [68] W. van Elmpt, S. Nijsten, R. Schiffeleers, A. Dekker, B. Mijnheer, P. Lambin, and A. Minken. A monte carlo based three-dimensional dose reconstruction method derived from portal dose images. *Med. Phys.*, 33:2426–2434, 2006.
- [69] M. van Herk and H. Meertens. A matrix ionisation chamber imaging device for on-line patient setup verification during radiotherapy. *Radiother. Oncol.*, 11:369–78, 1988.
- [70] World Health Organization (WHO). Quality assurance in radiotherapy. (*Geneva: WHO*), 1988.
- [71] World Health Organization (WHO), 2009. Fact sheet.
- [72] C. Yeboah and S. Pistorius. Monte carlo studies of the exit photon spectra and dose to a metal/phosphor portal imaging screen. *Med. Phys.*, 27:330–339, 2000.
- [73] J. Yeo and J. Kim. A Procedural Guide to Film Dosimetry. Medical Physics, Madison, WI, 2004.
- [74] C. X. Yu. Intensity-modulated arc therapy with dynamic multileaf collimation: an alternative to tomotherapy. *Phys. Med. Biol.*, 40:1435–1449, 1995.

